MODELING AND OBSERVER-BASED ROBUST CONTROL DESIGN FOR ENERGY-DENSE MONOPROPELLANT POWERED ACTUATORS

By

Navneet Gulati

Dissertation

Submitted to the Faculty of the

Graduate School of Vanderbilt University

in partial fulfillment of the requirements

for the degree of

DOCTOR OF PHILOSOPHY

in

Mechanical Engineering

December, 2005

Nashville, Tennessee

Approved:

Dr. Eric J. Barth

Dr. Michael Goldfarb

Dr. Nilanjan Sarkar

Dr. Joseph Wehrmeyer

Dr. Bobby Bodenheimer

To my parents

AKNOWLEDGEMENTS

First, I would like to express my gratitude to my advisor Dr. Eric J. Barth for his continuous guidance, advice, efforts, and direction he gave during the course of this work. He always inspired me to think independently and supported me with my ideas. I was greatly benefited by his openness in discussing and evaluating new ideas and his systematic way of approaching and solving a problem. The financial support in the form of research assistantship provided by the National Science Foundation is also gratefully acknowledged.

I am grateful to Dr. Michael Goldfarb for his constant encouragement and providing necessary facilities for the experiments. I am also thankful to Dr. Nilanjan Sarkar, Dr. Joseph Wehrmeyer, and Dr. Bobby Bodenheimer for their time and support as members of my thesis committee.

I would also like to thank my parents for their encouragement and continuous enthusiastic support. Without their support, it would have been impossible to come this far. No words could ever convey the enormous appreciation I feel for them. I would also like to express my gratitude to my brother, Sandeep, and his wife, Kiran, who have always been a source of inspiration in pursuing my endeavors.

Thanks are due to my graduate student colleagues of Center for Intelligent Mechatronics (CIM) Laboratory for all the help they provided and made my stay at Vanderbilt University both memorable and pleasurable. Last, but certainly not the least, I am indebted to all my friends who were always with me during the course of this work. Their lively presence always kept my morale high and motivated me to achieve my goals.

TABLE OF CONTENTS

LIST OF TABLES

LIST OF FIGURES

MECHANICAL ENGINEERING

MODELING AND OBSERVER-BASED ROBUST CONTROL DESIGN FOR ENERGY-DENSE MONOPROPELLANT POWERED ACTUATORS

NAVNEET GULATI

Dissertation under the direction of Professor Eric J. Barth

This dissertation presents the development of a monopropellant-based power supply and actuation system for human scale robots that is energy and power dense with the ability to be controlled accurately at a high bandwidth. This kind of actuation system is known to have an actuation potential an order of magnitude better than conventional battery-DC motor based actuation systems. Though a monopropellant-based actuator has the appeal of being simple in design, it is fairly complex in terms of the physics of its operation. The complex interaction between several energy domains and the nonlinear nature of many of them necessitates a model-based control design to provide adequately accurate, high-bandwidth, efficient, and stable operation as generally required of a mobile robot platform. In order to obtain a model-based controller, a physics-based model of this kind of a system is derived in this work. The control architecture of the centralized configuration is then presented which is shown to provide stable servo tracking of the system. This model-based controller is designed on the basis of Lyapunov stability-based sliding mode control theory to control the inertial mass. A model-based predictive controller is additionally implemented for the control of rate of pressurization and

regulation of the supply pressure in the reservoir. Since the model-based control of the actuators necessitates the use of two high-temperature pressure sensors, these sensors add substantial cost to the monopropellant-based servo system. In order to make the chemofluidic system more cost effective and economically viable, a nonlinear pressure observer is developed in this work. This observer utilizes the available knowledge of other measurable states of the system to reconstruct the pressure states. The elimination of pressure sensors reduces the initial cost of the system by more than fifty percent. Additionally, the use of pressure observers along with the design of a robust controller results in lower weight, more compact and lower maintenance system.

The development of two Lyapunov-based nonlinear pressure observers for pneumatic systems is also presented in this work. The implementation of pressure observers instead of expensive pressure sensors reduces the cost of the system by nearly thirty percent. These savings are achieved without any compromise on the quality of servo tracking of the system. The results presented demonstrate that the tracking performance using pressure observers versus using pressure sensors is in essence indistinguishable.

Approved_____ Date_____

CHAPTER I

INTRODUCTION AND MOTIVATION

Introduction

In recent years, we have witnessed the significant increase of robots in different areas of human life. The use of robots in manufacturing industries has not only resulted in the increase of productivity but it has also increased the quality of products. Today virtually all mass production industries rely heavily on robots to meet their production requirements. Robots are also increasingly employed in areas that are hazardous to humans. Waste removal in nuclear power plants, painting operations in car industries, forging operations are few areas where the environment is unhealthy and machines have successfully replaced humans. Realizing the potential of robots, this state of the art technology was extended to the development of mobile robots. Space exploration and rescue operations were amongst the few identified applications for the use of mobile robots. Last year NASA sent their mobile robots, Spirit and Opportunity, to the planet Mars for exploring the possibility of life there. Similarly, the use of mobile robots in rescue operations, such as to find trapped people from collapsed buildings, has been envisioned by engineers.

Despite all of these developments, there are areas where the use of untethered robots is still considered only for the far term. The use of a robot in combat operations is one such example. Another example is a service robot for people who are in need of assisted living. Among other technical problems in the introduction of robots in these and

other areas, one problem that remains and will remain absolutely prohibitive until its solution is the short operational time of untethered robots. Most of the industrial robots use the combination of DC motor and electricity from the grid for actuation. Mobile robots typically use electrochemical batteries to power motors. However, these types of batteries cannot supply power long enough to meet the requirements of human scale and power comparable robots. A battery/motor power supply and actuation system lacks the fundamental energy and power density required for a useful human-scale service robot. This is perhaps most poignantly illustrated by the P3 humanoid robot (Figure 1-1) developed by Honda. The P3 is arguably the most advanced human-scale humanoid robot in the world and has a mass of about 130 kg, with its nickel-zinc batteries contributing a total mass of about 30 kg. This robotic system is capable of about 15-30 minutes of operation, depending on its workload. This illustrates the major technological barrier for the development of human-scale mobile robots which can operate power-autonomously for extended periods of time.

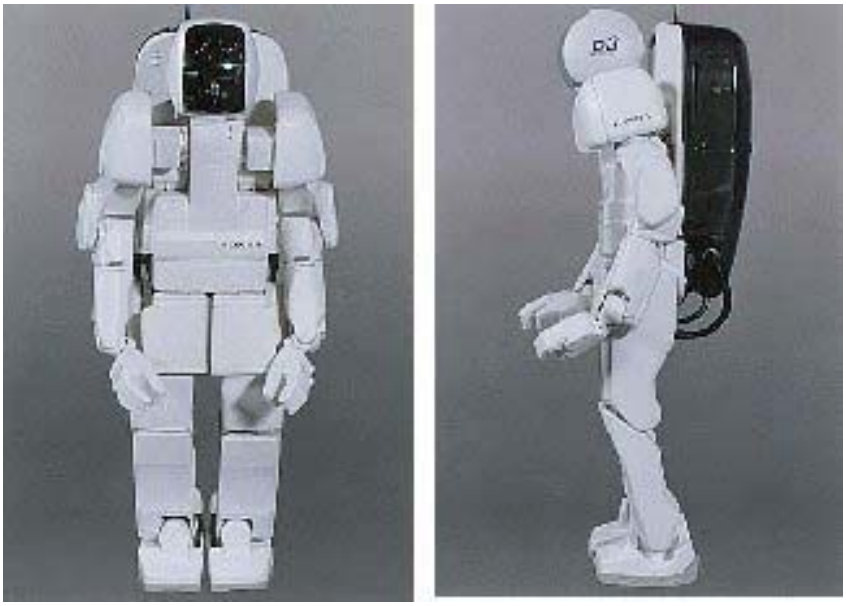

Figure 1-1. Honda P3 Humanoid Robot

Literature Survey

The problem of power limitation necessitates the development of an alternate power supply that can deliver power for an extended period of time. Some researchers have proposed proton exchange membrane fuel cells [1] or solid oxide fuel cells [2] as an alternative to batteries. These alternatives have significant power density limitations relative to the average power requirements of a human-scale robot. Some other authors suggested the use of internal combustion engines to power fluid-powered system, but such an approach is hampered by several issues, including the relative inefficiency of small engines, the loss of power necessitated by controlling power produced outside the control loop, noise problems, noxious exhaust fumes, and start-stop problems for a low duty cycle use. Further, such types of systems would be heavy and they require oxidizers for combustion that make it burdensome for some applications (such as space exploration or other non-oxygen environments).

Another class of fuels is the monopropellants [3] that are energy dense and hence hold the promise of meeting the power requirements of autonomous robots. Monopropellants are a class of propellants that decompose when they come in contact with a catalyst material. Monopropellants were originally developed in Germany during World War II [4]. Since then they have been utilized in several applications involving power and propulsion, most notably to power gas turbine and rocket engines for underwater and aerospace vehicles. In recent years they are also used in the development of micro-propulsion systems in nanosats [5], reaction control thrusters for space vehicles [6], and auxiliary power turbo pumps for aerospace vehicles. For this study, hydrogen peroxide was selected amongst other monopropellants for the development of energy-

dense actuators because it is ecological as the exhaust products are oxygen and steam which are safe for indoor use. Besides, hydrogen peroxide is a stable monopropellant and does not decompose on its own. It is also stable at relatively high temperatures.

The development of chemofluidic actuators was first published by Goldfarb et al. [7] where they presented their preliminary results. Two configurations were shown by the authors to extract mechanical work from hot gaseous products. The first configuration, known as centralized system (Figure 1-2), is essentially based on the principle of standard pneumatic actuation systems. In this type of configuration, liquid hydrogen peroxide is stored in a pressurized blow-down tank. The flow of hydrogen peroxide through the catalyst pack is governed by the discrete valve. When hydrogen peroxide comes in contact with the catalyst, it decomposes into steam and oxygen. These resultant hot gaseous products are collected into a reservoir. The hot reservoir is in turn connected to the cylinder chambers via a pneumatic four-way proportional valve. A controlled amount of fluid is provided to either of the two chambers depending on the force and the load requirements. In the second configuration, called direct injection, the piston output is controlled by injecting the hot gaseous products directly into the chambers from the catalyst pack. Therefore, this configuration necessitates the use of two catalyst packs, one for each chamber of the cylinder. The output in this type of system is controlled with the help of valves that governs the flow of a monopropellant to the catalyst packs, as well as an exhaust valve that depressurizes each chamber by exhausting the gaseous products to the external environment.

The centralized configuration of actuators was shown to have five times better actuation potential than conventional DC motors based actuators [7]. However, for the

control of centralized configuration, the authors used a non-model based position-velocity-acceleration (PVA) controller for the servo control of the inertial load. It has been shown in the literature [8-10] that model-based control design is more robust, stable and provides high bandwidth. Therefore, to obtain a model-based controller for chemofluidic actuators, a model of the system is first derived. This model is based on the first principle constitutive relationships and it also validates the earlier derived empirical/analytical model by Barth et al. [11]. The servo control design based on this model is then formulated and is presented in this work. A pressure observer is also designed and implemented to reduce the initial costs of the system by more than 50 percent. The earlier work on pressure observers by Pandian et al. [12] uses the assumptions of choked flow and known mass flow rate through the valve. Both of these assumptions are restrictive since at low pressure difference, the flow rate is not choked. Also, the mass flow rate is a function of pressure whose value is to be estimated. In this work, the observer uses the knowledge of other measurable states to reconstruct the pressure states.

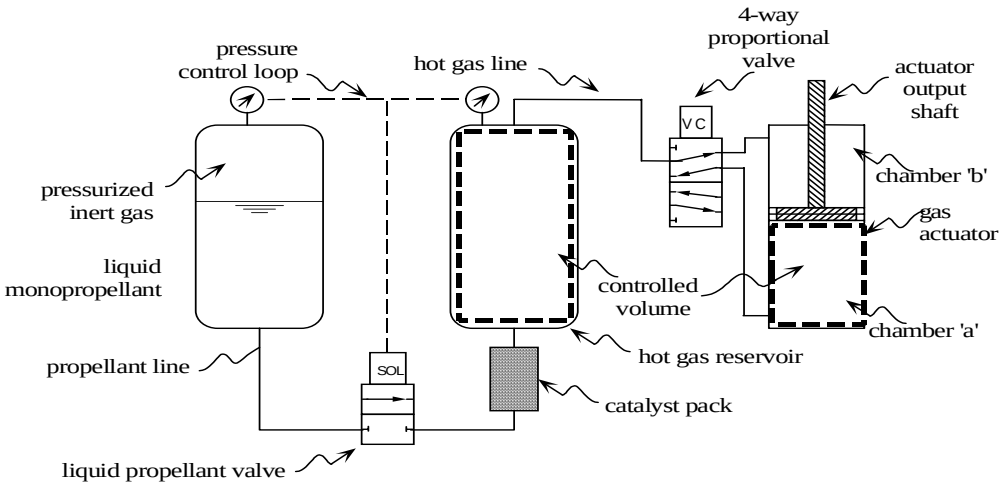

Figure 1-2. Schematic of the Centralized Configuration of Monopropellant Powered Actuators

Motivation and Contribution

The primary motivation of this work is to develop a power source that is capable of providing energy and power appropriate for controlled actuation for extended periods of time. While the chemofluidic actuator has the appeal of being simple in design, it is fairly complex in terms of the physics of its operation. The complex interaction between several energy domains and the nonlinear nature of many of them necessitates a model-based control design to provide adequately accurate, high-bandwidth, efficient, stable operation as generally required of a mobile robot platform. In order to obtain a model-based controller, a model of this kind of a system was first derived in this work. The commonly used states that characterize such a system are the position, velocity, and pressures in both chambers of the cylinder. The sensors used in such a type of system are a potentiometer for measuring the position and two pressure sensors per axis to characterize the energy storage in each chamber. The problem with the pressure measurement is that the high-bandwidth, high-temperature, and high-pressure sensors required for the control of a servo system are expensive and large (relative to the actuator) with a typical cost between $400 and $1200. Since pneumatic actuation requires two pressure sensors per axis, these sensors add $800 to $2400 per axis of monopropellant based servo system. If the requirement of pressure sensors can be eliminated by constructing observers to estimate these states, it will result in an average savings of approximately 50 percent in initial costs. Since the other states (viz. motion output and velocity) are measurable, the possibility exists to reconstruct the cylinder pressures by using the available knowledge of other states of the system.

In order to eliminate the pressure sensors from the control of such systems, the work was commenced for the design of pressure observers. As noted earlier, the dynamics of a chemofluidic system are highly non-linear and fairly complex. In order to test the concept of controlling such a system using pressure observers instead of sensors, the theory was first conceptualized for pneumatic actuators. Pneumatic actuators were selected for the initial development for several reasons. First, the dynamics are similar to chemofluidic actuators and hence it is easy to derive conclusions based on the results of pneumatic actuators. Another reason was that it was desirable to reduce the cost of pneumatic systems since pressure sensors contribute approximately 30 percent in the initial cost of the system. The other less fundamental reason was the easy availability of the pneumatic actuator components because unlike chemofluidic actuators, the pneumatic system does not operate at elevated temperatures.

The development of two Lyapunov-based pressure observers for the pneumatic actuator system is presented in this work. The first method shows that an energy-based stable pressure observer can be developed with the state equations. The other method incorporates the output error to control the convergence of the observed pressures. The stability, robustness, and convergence of both the observers are discussed in this work. The results presented demonstrate that the tracking performance using pressure observers versus pressure sensors is in essence indistinguishable.

The observer design for the pneumatic actuators is then extended to chemofluidic actuators. A model-based controller is further developed, which uses a pressure observer for each chamber of the actuator, to provide adequately accurate, high-bandwidth, and stable servo control of a chemofluidic actuator. The control architecture for the

centralized configuration of the actuators is divided in two parts. The first part of the control problem is the pressurization and regulation of the hot gas reservoir. The functional requirement of the reservoir is to maintain a uniform desired pressure with minimum pressure fluctuations in it. Since transportation delay of 15 ms is present in the system, a predictive control design is selected. The second part of the control problem is the stable servo control of the inertial load. The Lyapunov-based sliding mode control is selected for the motion because of its robustness to deal with the model uncertainties as well as uncertainties due to the pressure observers. The results of the servo tracking are presented which show the effectiveness of the proposed control architecture for the actuators.

Organization of the Document

The dissertation is organized in four chapters. Chapter I presents the introduction and motivation of the complete project. Chapter II, III, and IV of this dissertation comprise different manuscripts that have been submitted for publication as independent journal papers. Chapter II is a journal paper that is submitted to the *ASME Journal of Dynamic Systems, Measurement, and Control* as a full paper. This part presents the detailed mathematical modeling of the monopropellant powered actuators. The modeling of a power and energy dense chemofluidic actuation system discussed herein is aimed at producing a model based on first principles. The model of the system should ideally be simple with the minimum number of states, but at the same time should capture all of the relevant dynamics of the system from a control standpoint. This model is intended to

provide a basis upon which the model-based controllers are to be developed for this actuation concept.

Chapter III is the detailed description of the development of two nonlinear pressure observers and a model-based controller for pneumatic actuators. The pressure states are reconstructed with the available knowledge of the position of the spool valve in both the methods. The merits and demerits of both the developed observers are also discussed. The servo tracking results presented show that pressure observers can successfully eliminate expensive pressure observers. Conference papers based on this work has already been published [13, 14]. The journal version is submitted as a full paper to the *ASME/IEEE Transactions on Mechatronics*.

Chapter IV presents the development of a model-based controller for the centralized configuration of monopropellant powered actuators. This control design is based on the model derived in Chapter II. A pressure observer is also developed to reduce the initial cost of the system. The control design constitutes a model-based predictive controller for pressurization loop and a sliding mode controller for the servo position control of the load. The design of pressure observer is the extension of the work on pressure observers presented in Chapter III. Simulation and experimental results are presented that validate the effectiveness of the proposed observer theory. The observer in this work is used to obtain a high-bandwidth and stable model-based control design. Chapter IV is submitted as a full paper to the *IEEE Transactions on Robotics.*.

References

[1] McCurdy, K., Vasquez, A., and Bradley, K., "Development of PEMFC systems for space power applications," First *International Conference on Fuel Cell Science, Engineering and Technology*, pp. 245-251, Rochester, NY, 2003.

[2] Tappero, F. and Kato, T., "Simulation Model of a Hybrid Power Generation System for Humanoid Robots," *Proceedings of the Fourth IASTED International Conference on Power and Energy Systems*, pp. 550-556, Rhodes, Greece, 2004.

[3] McCormick, J.C., "*Hydrogen Peroxide Rocket Manual*", FMC, 1967.

[4] Wernimont, E.J., Ventura, M., Garboden, G. and Muellens, P., "Past and Present Uses of Rocket Grade Hydrogen Peroxide", *Proceedings of the 2nd International Hydrogen Peroxide Propulsion Conference*, pp. 45-67, November 7-10, 1999.

[5] Hearn, H. C., "Performance Prediction Model for a High-Impulse Monopropellant Propulsion System", *Journal of Spacecraft and Robots*, vol. 11, no. 11, pp. 764-768, 1974.

[6] Hitt, D. L., "MEMS-Based Satellite Micropropulsion via Catalyzed Hydrogen Peroxide Decomposition", *Smart Materials and Structures*, vol. 10, no. 6, pp. 1163-1175, 2001.

[7] Goldfarb, M., Barth, E. J., Gogola, M. A., and Wehrmeyer, J. A., "The Design and Modeling of a Liquid-Propellant-Powered Actuator for Energetically Autonomous Robots," *ASME International Mechanical Engineering Congress and Exposition*, November 2002.

[8] Richer, E., Hurmuzlu, Y., "A High Performance Pneumatic Force Actuator System: Part I – Nonlinear Mathematical Model", *ASME Journal of Dynamic Systems, Measurement, and Control*, Vol. 122, no. 3, pp. 426-434, 2000.

[9] Richer, E., Hurmuzlu, Y., "A High Performance Penumatic Force Actuator System: Part II – Nonlinear controller Design", *ASME Journal of Dynamic Systems, Measurement, and Control*, vol.122, no.3, pp.426-434, 2000.

[10] Bobrow, J., and McDonell, B., "Modeling, Identification, and Control of a Pneumatically Actuated, Force Controllable Robot," *IEEE Transactions on Robotics and Automation*, vol. 14, no. 5, pp. 732-742, 1998.

[11] Barth, E. J., Gogola, M. A., Goldfarb, M., "Modeling and Control of a Monopropellant-Based Pneumatic Actuation System", *IEEE International Conference on Robotics and Automation*, Vol. 1, pp. 628-633, 2003.

[12] Pandian, S. R., Takemura, F., Hayakawa, Y., and Kawamura, S., “Pressure Observer-Controller Design for Pneumatic Cylinder Actuators”, *IEEE/ ASME Transactions on Mechatronics*, Vol 7, no. 4, pp. 490-499.

[13] Gulati, N. and Barth, E., “Non-linear Pressure Observer Design for Pneumatic Actuators”, *IEEE/ ASME International Conference on Intelligent Mechatronics*, Monterey, CA, 2005.

[14] Gulati, N. and Barth, E., “Pressure Observer Based Servo Control of Pneumatic Actuators”, *IEEE/ ASME International Conference on Intelligent Mechatronics*, Monterey, CA, 2005.

CHAPTER II

MANUSCRIPT I

DYNAMIC MODELING OF A MONOPROPELLANT-BASED CHEMOFLUIDIC ACTUATION SYSTEM

Navneet Gulati and Eric J. Barth

Department of Mechanical Engineering

Vanderbilt University

Nashville, TN 37235

Submitted as a Full Paper to the

ASME Journal of Dynamic Systems, Measurement and Control

Abstract

This paper presents a dynamic model of a monopropellant based chemofluidic power supply and actuation system. The proposed power supply and actuation system, as presented in prior works, is motivated by the current lack of a viable system that can provide adequate energetic autonomy to human-scale power-comparable untethered robotic systems. As such, the dynamic modeling presented herein is from an energetic standpoint. Two design configurations of the actuation system are presented and both are modeled. A first-principle based lumped-parameter model characterizing reaction dynamics, hydraulic flow dynamics, and pneumatic flow dynamics is developed for purposes of control design. Experimental results are presented that validate the model.

1. Introduction

The modeling of a power and energy dense chemofluidic actuation system discussed herein is aimed at producing a model based on first principles. The model of the system should ideally be simple with the minimum number of states, but at the same time should capture all of the relevant dynamics of the system from a control standpoint. This model is intended to provide a basis upon which to develop model-based controllers for this actuation concept. While the chemofluidic actuator has the appeal of being simple in design, it is fairly complex in terms of its operation. The complex interaction between several energy domains and the nonlinear nature of many of them necessitates a model-based control design to provide adequately accurate, high-bandwidth, efficient, stable operation as generally required of an untethered mobile robot platform. The modeling work for this kind of a system was started by Barth et al [1] where they presented a

preliminary model of the system that contained both first principle and empirical modeling elements. In this work, a purely first principle based model of the system is derived that utilizes known physical parameters or manufacturer provided parameters, and a minimal number of empirical parameters specific to the particular system components and configuration used. Furthermore, this model formalizes and validates the previously mixed derived/empirical model.

In recent years, the use of robots has gained significant importance in many arenas. Whereas industrial robots are primarily powered by electricity from the grid and require little consideration regarding their supply of power, mobile robots typically use a combination of electrochemical batteries and DC motors for power supply and actuation. Given that a mobile untethered robot must not only carry its supply of power but must also carry its own mass, the operation time of mobile robots is limited by both the energetic capacity of the battery and the overall mass of the combined power supply and actuation system. A battery/motor power supply and actuation system lacks the fundamental energy and power density required for a useful human-scale service robot. This is perhaps most poignantly illustrated by the P3 humanoid robot developed by Honda. The P3 is arguably the most advanced human-scale humanoid robot in the world and has a mass of about 130 kg, with its nickel-zinc batteries contributing a total mass of about 30 kg. This robotic system is capable of about 15-30 minutes of operation, depending on its workload. This illustrates a major technological bottleneck for the development of human-scale mobile robots that can operate power-autonomously (untethered) for extended periods of time.

Short operational times and limited power limits the introduction of mobile robots in applications where they can considerably improve the quality of human life or replace humans performing hazardous operations. As an example, a robot in a combat operation is expected to continue for sufficiently long enough time to complete the mission [2]. Similarly, a robot can be used in an environment that is hazardous by nature to the human health. One such situation is clearing the nuclear waste in a nuclear power plant where the environment is extremely unhealthy [3,4]. Another application that is currently being explored is the introduction of service robots for people who are in need of assisted living, such as the elderly or handicapped [5]. One of the principal purposes of such a robot assistant would be to provide handicapped people with the freedom to live and travel independently. A service robot should thus ideally travel nearly everywhere with its attendee and perform such tasks as reaching items from the upper shelves of a grocery store. Similarly, the use of robots in rescue operations is an active area of research. A mobile robot can be deployed to search the debris of collapsed structures to look for trapped victims [6]. Space exploration is another application where the robots are used, but their functionality is greatly limited [7]. In almost all the cases, the robots are required to have a power source that is capable of providing energy and power appropriate for controlled actuation for extended periods of time. To make use of the full potential of mobile robots, an alternative power source is needed.

One of the alternatives to a battery is the use of liquid fuels for the power supply and actuation of self-powered robots. Liquid chemical fuels have high thermodynamic energy densities. In this case the stored chemical energy of the fuels can be converted to heat whereupon the resulting heat released is converted to mechanical energy by the

expansion of gaseous products. Among several possibilities, monopropellant liquid fuels offer several advantages for this type of system over other candidate fuels or energetic materials [8]. Monopropellants are a class of chemicals that rapidly decompose in the presence of a catalyst. Since no ignition is required to start the chemical reaction, it eliminates the need of an igniting mechanism and thereby results in a low weight energy converter system. Moreover, since the exposure of the monopropellant to the catalytic material can be controlled via an actuated valve, this form of energy transduction lends itself well to controlled compressible fluid power actuation systems. Additionally, this method of transduction and actuation provides a high energy density, a high power density, the ability to refuel, and the distribution of power through small and flexible liquid lines. For the experimental system presented here, hydrogen peroxide is selected from among other monopropellants (e.g., hydrazine or hydroxyl-ammonium-nitrate). The main reasons for this selection are hydrogen peroxide's non-toxicity, relative ease of handing, its stability at high temperatures, and the safe exhaust products (oxygen and water) that allow it to be used indoors.

Monopropellants were originally developed in Germany during World War II. Since then they have been utilized in applications such as power gas turbines and thrusters of Spacecrafts (e.g. [9]). Their potential has also been recognized for the development of micro-propulsion systems in nano-satellites [10]. However, unlike the servo-controlled chemofluidic actuators discussed in this paper, the exothermic reaction dynamics are typically not a part of the control loop in present applications of monopropellant based systems. The chemofluidic system also poses several unique low-level (i.e., position, force, and impedance) control challenges unlike those present in the

control of other more standard actuators like DC motors or fluid-powered (i.e., hydraulic or pneumatic) actuators. The uniqueness of these challenges is due to several factors. First, the system is both hydraulic and pneumatic in nature. As described in the following section, the inlet flow to the direct-injection system is hydraulic, while the exhaust flow is pneumatic, and the control of the mechanical work output requires the cooperative control of both. Second, the exothermic reaction dynamics that provide the actuator work are contained inside the control loop. These dynamics are significant and cannot be neglected, and thus stable high-bandwidth control requires an appropriately constructed lumped-parameter dynamic characterization. In addition to the reaction dynamics, the thermal energy generated by the exothermic reaction is transduced to mechanical work via the thermodynamic constitutive behavior of the reaction products, which must also be dynamically characterized for stable, desirable, closed-loop behavior.

Though the modeling and control of fluid powered actuation has been a topic of study present in the scientific literature (e.g. refer [11-14]) since the 1950's, little modeling has been done for the hydraulic/pneumatic chemofluidic system described in this paper. Recent works by Barth et al. [1] have shown the modeling of the direct injection system. Some preliminary experimental findings on the energetic capability of the chemofluidic actuation system are presented in [15]. In their work, a first order dynamic model was assumed for the heat released. Similarly the heat loss was characterized by a first order dynamic equation. In this paper, the system model is extended to replace the assumptions with first principle constitutive relations.

2. Operating Principle

The operating principle of the monopropellant powered system to extract mechanical work is shown in Figure 2-1. Hydrogen peroxide is fed from a pressurized blow-down storage tank into the catalyst pack via a solenoid-actuated valve. The storage tank is pressurized to 2070 kPa (300 psig) with an inert gas to create the necessary pressure drop across the valve required for fuel delivery. The duration of the valve opening governs the amount of hydrogen peroxide that flows into the catalyst pack. Upon contact with the catalyst, the monopropellant decomposes into steam and oxygen as per the following equation:

$$2H_2O_2(l) \rightarrow 2H_2O(l) + O_2(g) + Heat \quad (1)$$

The decomposition of hydrogen peroxide is highly exothermic. Two possible configurations to extract mechanical work from the hot gaseous products are shown in the figure. Figure 2-1(a) shows a *centralized system* in which the hot gaseous products are collected in a centralized reservoir. This hot reservoir is in turn connected to the actuator's cylinder chambers via a voice-coil-actuated pneumatic four-way proportional valve. A controlled amount of compressible fluid is provided by the valve to either of the two chambers depending on the force and the load requirements to generate the desired mechanical work.

In the second configuration (Figure 2-1.b), termed as *direct injection*, the work of the actuator piston is controlled by directly injecting the hot gaseous products from the catalyst pack into the chambers (i.e., no reservoir for storing hot gases). The output of this type of a system is controlled using liquid valves that govern the flow of monopropellant to the catalyst packs, as well as an exhaust valve that depressurizes each

chamber by exhausting the gaseous products to the external environment. The block diagram of both the configurations is shown in figure 2-2.

3. System Modeling

The modeling task here includes the modeling of a hydraulic inlet valve, a catalyst pack, a compressible fluid power actuator, and a pneumatic exhaust valve. An energy balance based approach is taken to model these components and their interaction. In the case of the catalyst pack and actuator chamber, a control-volume approach is taken. With the knowledge of the mass, energy, and heat crossing the boundary of the control-volume, the system dynamic equation can be derived using the law of conservation of energy.

3.1 Hydraulic Inlet Valve

The hydraulic valve is one of the control elements of the actuation system. Precise control of the system requires the precision metering of monopropellant via the valve. The mass flow rate through the valve is a function of upstream and downstream pressures and the density of the fluid flowing through the valve, and is given as follows:

$$\dot{m}_{in} = \rho \dot{Q}_{in} \tag{2}$$

where, $\dot{m}_{in}$ is the mass flow rate; ρ is the density of the fluid; $\dot{Q}_{in}$ is the volumetric flow rate. The volumetric flow rate can be derived using Euler's and Continuity equations and is defined by:

$$\dot{Q}_{in} = C_d A_o \sqrt{\frac{2}{\rho}(P_1 - P_2)} \tag{3}$$

where, C_d is the discharge coefficient (a manufacturer provided, or easily measured, parameter); A_0 is the orifice area of the valve; P_1 and P_2 are the upstream and downstream pressures respectively. Substituting equation (3) into equation (2) yields:

$$\dot{m}_{in} = C_d A_o \sqrt{2\rho(P_1 - P_2)} \tag{4}$$

Equation (4) is a well accepted model in the literature for the liquid flow through a control valve. This model cannot be derived rigorously but instead is obtained by considering the control valve as analogous to a flat plate orifice (Figure 2-3).

Since the density of the fluid passing through the control valve is constant for the system presented in this paper, equation (3) can be re-written in a simplified form as:

$$\dot{m}_{in} = C_1 A_0 \sqrt{(P_1 - P_2)}, \qquad \text{where } C_1 = C_d \sqrt{2\rho} \tag{5}$$

3.2 Catalyst Pack

The catalyst pack is the component where the energy conversion from stored chemical energy to heat takes place. The monopropellant enters into the catalyst pack from one end and the chemical reaction is triggered as it moves over the catalyst bed. As a result, hydrogen peroxide decomposes into steam and oxygen and heat energy is liberated. The catalyst bed offers resistance to the flow of both the reactant and the resultant gaseous products. The flow resistance can be modeled as the fluid passing through an orifice (Figure 2-4) and the governing equations can be obtained. The modeling of the catalyst pack is divided into two subsections. In the first subsection, the flow resistance offered by catalyst bed is modeled. The next subsection captures the

reaction dynamics and the energy released by the decomposition of the monopropellant hydrogen peroxide.

3.2.1 Catalyst Pack Flow Resistance

Since the inlet to the catalyst pack is a liquid and the output is gaseous products, the flow over the catalyst bed can be modeled as two extremes. In the first case, it is considered that the monopropellant decomposes at the end of the catalyst pack and hence the flow through the catalyst pack is a liquid throughout the length. In the second case, it is considered that the monopropellant decomposes at the start of the catalyst pack and hence the gaseous products flow across the length. With the first consideration, the derivation of mass flow rate through the catalyst pack is similar to the model of the hydraulic inlet valve and is given as:

$$\dot{m}_{in} = C_2 A_{cat} \sqrt{(P_2 - P_3)} \tag{6}$$

where P_2 and P_3 are the upstream and downstream pressures of the catalyst pack respectively, C_2 is the function of discharge coefficient (C_d) of the catalyst pack and the density of the fluid (ρ) passing through it ($C_2 = C_d \sqrt{2\rho}$), and A_{cat} is the effective area of the catalyst pack.

With the second assumption (decomposition at the beginning of the catalyst pack), the mass flow rate can be obtained as discussed in Section 3.4 of this paper. Both cases considered here are ideal and in reality, the phase transformation takes place somewhere along the length of the catalyst pack. In this paper, the first assumption (decomposition at the end of the catalyst pack) is used to calculate the mass flow rate

through the hydraulic inlet valve and the catalyst pack. Eliminating P_2 from equations (5) and equation (6) yields:

$$\dot{m}_{in} = C^* \sqrt{(P_1 - P_3)} \qquad \text{where, } C^* = \frac{(C_1 A_0)(C_2 A_{cat})}{\sqrt{(C_1 A_0)^2 + (C_2 A_{cat})^2}} \tag{7}$$

This above equation characterizes the input-output relationship of the inlet hydraulic valve as shown in the block diagram (figure 2-2). The input to the block is the area of the valve and the output is the mass flow rate of the propellant.

3.2.2 Catalyst Pack Thermal Modeling

A control volume (CV) approach is taken to model the catalyst pack. As such, mass, heat, and work can cross boundaries of the control volume. A power balance equates the energy storage rate to the energy flow rate crossing the boundary. The rate form of the first law of thermodynamics is given as follows:

$$\dot{U}_{cat} = \dot{H}_{cat} + \dot{Q}_{cat} - \dot{W}_{cat} \tag{8}$$

where $\dot{U}_{cat}$ is the rate of change of the internal energy of the catalyst pack, $\dot{H}_{cat}$ is the net rate of change of enthalpy entering the catalyst pack, $\dot{Q}_{cat}$ is the net rate of change of heat energy entering into the catalyst pack, and $\dot{W}_{cat}$ is the power or rate of work done by the system on the external environment. The potential and kinetic energy associated with the fluid/ gases entering and leaving the catalyst pack is assumed negligible in equation (8). This is because of the fact that these energies are negligible as compared to the heat energy of the gases that are leaving the controlled volume. In addition, uniform properties of the mass entering and leaving the CV are assumed.

The dynamic characteristics of the catalyst pack are obtained by solving equation (8). In the following part of this section, all the terms of equation (8) are evaluated and the resulting expressions are then substituted in the rate form of first law of thermodynamics (i.e., equation (8)) to obtain the input-output relationship of the catalyst pack block of figure 2-2.

(a) Determining Rate of Change of Work Done

Considering the fixed volume of the catalyst pack, the work done by the catalyst pack on a CV drawn around it is zero and hence,

$$\dot{W}_{cat} = 0 \tag{9}$$

(b) Determining Rate of Change of Enthalpy:

The net rate of change of enthalpy is given by:

$$\dot{H}_{cat} = (\dot{H}_{cat})_{in} - (\dot{H}_{cat})_{out} \tag{10}$$

where $(\dot{H}_{cat})_{in}$ and $(\dot{H}_{cat})_{out}$ are the rate of change of enthalpy entering and leaving the CV respectively. $(\dot{H}_{cat})_{in}$ in equation (10) is calculated by the expression:

$$(H_{cat})_{in} = m_{in} C_p T_{in} \tag{11}$$

where m_{in} is the mass of the fluid entering into the CV, C_p is the average specific heat of the liquid monopropellant at a constant pressure, and T_{in} is the temperature of the liquid entering into the CV.

Differentiating equation (11) yields:

$$(\dot{H}_{cat})_{in} = \dot{m}_{in} C_p T_{in} + m_{in} C_p \dot{T}_{in} \tag{12}$$

Since there is almost no variation in the temperature of monopropellant entering into the catalyst pack, T_{in} can be assumed as constant and the equation (12) reduces to the following:

$$(\dot{H}_{cat})_{in} = \dot{m}_{in} C_p T_{in} \tag{13}$$

Substituting $(\dot{H}_{cat})_{in}$ from equation (13) into equation (10) yields:

$$\dot{H}_{cat} = \dot{m}_{in} C_p T_{in} - (\dot{H}_{cat})_{out} \tag{14}$$

(c) *Determining Heat Energy Rate Entering the Controlled Volume:*

The rate of heat energy supplied to CV can be calculated as follows:

$$\dot{Q}_{cat} = \dot{Q}_D - \dot{Q}_E \tag{15}$$

where $\dot{Q}_D$ is the rate of heat released by decomposition of hydrogen peroxide and $\dot{Q}_E$ is the rate of heat lost to the environment.

The decomposition of a monopropellant in the catalyst pack results in the release of heat. The chemical equation of hydrogen peroxide decomposition is given by the equation (1). The heat released by the reaction can easily be calculated using enthalpy of formation h_f and molecular weights of the reactants and the products:

$$h_{f(H_2O_2)}(l) = -187.61\ kJ/mol;\ h_{f(H_2O)}(l) = -285.83\ kJ/mol;\ h_{f(O_2)} = 0; \tag{16}$$

The molecular weights of H_2O_2, H_2O, and O_2 are 34.016 *g/mol*, 18.016 *g/mol*, and 32 *g/mol* respectively.

Using heats of formation and molecular weights, equation (1) can be used to derive the heat produced in the reaction:

$$1\ kg\ (H_2O_2) = x_{O_2}\ kg\ (H_2O) + x_{H_2O_2}\ kg\ (O_2) + \Delta H_r \tag{17}$$

where ΔH_r is the heat released per kilogram of hydrogen peroxide.

$$x_{O_2} = 0.53, \quad x_{H_2O_2} = 0.47, \quad \Delta H_r = 2887.465\ kJ \text{ for } 100\%\ H_2O_2 \tag{18}$$

$$x_{O_2} = 0.67, \quad x_{H_2O_2} = 0.33, \quad \Delta H_r = 2020.615\ kJ \text{ for } 70\%\ H_2O_2 \text{ (by volume)}$$

With known ΔH_r, $\dot{Q}_D$ can be calculated using the following equation:

$$\dot{Q}_D = -\Delta H_r \dot{m}_D \tag{19}$$

where $\dot{m}_D$ is the decomposition rate of hydrogen peroxide in the CV. The decomposition of hydrogen peroxide obeys a first order chemical kinetics law. The rate of decomposition is strongly dependent on the temperature, purity of the monopropellant, and the type of catalyst used. The rate of change of the concentration of hydrogen peroxide is given by the Arrhenius law (refer Khoumeri et al. [16]):

$$\frac{d[H_2O_2]_D}{dt} = -K_o e^{-E_a/RT}[H_2O_2] \tag{20}$$

where $\frac{d[H_2O_2]_D}{dt}$ is the rate of change of concentration of hydrogen peroxide in the CV, E_a (J/mol) is the activation energy of hydrogen peroxide, T is the temperature inside the catalyst pack , K_o is the pre-exponential factor, and $e^{-E_a/RT}$ is the Boltzmann factor.

Multiplying equation (20) by molecular weight and the volume of hydrogen peroxide results in:

$$\dot{m}_D = -K_o e^{-E_a/RT} m \tag{21}$$

where *m* is the total mass of the monopropellant in the catalyst pack. The above equation shows that the rate of decomposition of hydrogen peroxide increases exponentially with an increase in temperature. The non-linear dynamic model presented by Khoumeri et al. for the change of hydrogen peroxide decomposition showed a good agreement with experimental results. The authors showed the results with a fixed initial amount of hydrogen peroxide. The same model is used in this paper and the mass of the monopropellant inside the catalyst pack as calculated as follows:

$$m = \int_0^t (\dot{m}_{in} - \dot{m}_D) dt \tag{22}$$

In the Laplace domain, equations (19), (21), and (22) can be more compactly represented by the following (with a slight abuse of notation due to the non-constant coefficient):

$$\frac{\dot{Q}_D}{\dot{m}_{in}} = \frac{\Delta H_r}{\tau s + 1} \quad \text{where, } \tau = \frac{1}{K_o e^{-E_a/RT}} \tag{23}$$

Equations (23) can be solved either analytically or numerically to calculate the rate of decomposition of hydrogen peroxide and for the resulting amount of heat released.

(d) Determining Rate of Heat Loss:

The energy released by the chemical reaction, Q_D, increases the temperature of the fluid flowing through the catalyst pack. This results in the phase transformation of the reactants and the products from liquid to the gaseous state. A portion of the energy released is also lost to the catalyst pack walls. If linear heat conduction is considered, a unit analysis reveals that it can be cast in terms of energy flow rates. The linear heat conduction equation can be derived using Fourier's law of heat conduction and is given in the following form,

$$\dot{Q}_E = \frac{kA}{l}(T_{high} - T_{atm}) \tag{24}$$

where k is the thermal conductivity of the material, $\frac{A}{l}$ represents the characteristic length, T_{high} represents the temperature inside the catalyst pack, and T_{atm} is the temperature of the surroundings. Though this equation gives a direct relationship for heat loss to the environment, it also necessitates the measurement of the temperature inside the catalyst pack. To avoid adding state variables relating to the temperature of the decomposed substance inside the catalyst pack, the temperature of the catalyst pack walls and the external environment, the temperature inside the catalyst pack T_{high} is assumed to be constant. The alternate approach that relates the heat loss to previously established state variables regarding energy flow rate is as follows.

The rise in temperature inside the catalyst pack is the direct result of the rate of heat released by the decomposition of hydrogen peroxide. As a consequence, the following approximation can be made:

$$T_{high} = T_{atm} + k_{cp}\dot{Q}_D \tag{25}$$

where, k_{cp} is a proportionality constant. The above equation shows that a higher decomposition rate implies higher temperature inside the catalyst pack and hence higher heat losses. As per this assumption, there is no heat transfer to the environment when the decomposition rate of the monopropellant is zero. However, it should be noted that in the actual case, there is some heat transfer but it is negligible as compared to the losses from the actuator due to the larger surface area of the actuator as compared with the catalyst pack.

Substituting equation (25) equation into equation (24) yields:

$$\dot{Q}_E = \frac{kAk_{cp}\dot{Q}_D}{l} \tag{26}$$

Since $\frac{kAk_{cp}}{l}$ is a constant for a particular configuration of the catalyst pack, the above equation can be rewritten as:

$$\dot{Q}_E = k_{cat}\dot{Q}_D \tag{27}$$

Either of the two equations, equation (24) (with T_{high} as constant) or equation (27), can be used to calculate the rate of heat transfer from the catalyst pack. The resulting inaccuracy due to the assumptions made here can be taken into account with the design of a model-based robust controller.

(e) *Determining Rate of Change of Internal Energy:*

The internal energy of the catalyst pack is the energy stored by the fluid in the CV, where the walls are excluded from the CV. The amount of energy stored by the fluid is negligible as compared to the energy stored in the catalyst pack walls (modeled as heat loss). This can be seen by considering the steady state temperature condition of the catalyst pack. During the steady state condition, the fluid inside the catalyst pack and its walls are at the same temperature:

$$\Delta T_{cat} = \Delta T_w \tag{28}$$

where ΔT_{cat} and ΔT_w represent the change of temperatures of fluid in the catalyst pack and the walls respectively from an arbitrary reference temperature. Using the relationship, $\Delta U = mC\Delta T$,

$$\frac{\Delta U_{cat}}{m\ C_{cat}} = \frac{\Delta U_w}{m_w C_w} \tag{29}$$

therefore,

$$\Delta U_{cat} = \frac{m}{m_w}\frac{C_{cat}}{C_w}\Delta U_w \tag{30}$$

where m_w is the mass of the catalyst pack casing, C_{cat} and C_w are the specific heats at constant volume of the fluid in the catalyst pack and casing respectively. Dividing both sides of the equation (30) by Δt and taking the limit:

$$\dot{U}_{cat} = \frac{m}{m_w}\frac{C_{cat}}{C_w}\dot{U}_w \tag{31}$$

The ratio $\frac{m}{m_w} << 1$ (approx. 10^{-4}) and also $\frac{C_{cat}}{C_w} < 1$. Therefore,

$$\dot{U}_{cat} \approx 0 \tag{32}$$

Substituting $\dot{W}_{cat}$, $\dot{H}_{cat}$, $\dot{Q}_{cat}$, and $\dot{U}_{cat}$ from equations (9, 14, 15, 32) in equation (8):

$$(\dot{H}_{cat})_{out} = \dot{m}_{in} C_p T_{in} + \dot{Q}_D - \dot{Q}_E \tag{33}$$

With these substitutions, equation (33) can be reduced to the following compact representation (again with a slight abuse of notation):

$$\frac{(\dot{H}_{cat})_{out}}{\dot{m}_{in}} = \left[C_p T_{in} + \frac{\Delta H_r}{\tau s + 1} - k_{cat}\frac{\Delta H_r}{\tau s + 1} \right] \tag{34}$$

The input-output relationship of the catalyst pack block in figure 2-2 is governed by equation (34). The control input to the block is the mass flow rate of the monopropellant and the output is the enthalpy rate flowing out of the catalyst pack.

3.3 Actuator

The schematic in Figure 2-1 shows the control volume with moving boundaries for the chamber. In this case, the control volume boundaries change with the position of

the piston. The energy balance equation is again applied, as per the first law of thermodynamics, to obtain:

$$\dot{U}_{ch} = \dot{H}_{ch} + \dot{Q}_{ch} - \dot{W}_{ch} \tag{35}$$

In the above equation, subscript "*ch*" shows that properties here stand for the chamber. The dynamic characteristics of the actuator are obtained by the use of the above equation. All of the terms of this equation are evaluated in the following subsections.

(a) Rate of Change of Internal Energy

By taking the average specific heat, C_v, in the temperature range of 300*K* to 450*K*, internal energy of the chamber is given by the expression:

$$U_{ch} = (m_{ch} C_v T_{ch}) \tag{36}$$

where m_{ch} is the mass of the gaseous products in the CV of the cylinder and T_{ch} is the temperature in the cylinder. Therefore,

$$\dot{U}_{ch} = \frac{d}{dt}(m_{ch} C_v T_{ch}) \tag{37}$$

Using the relationship, $C_v = \frac{R}{\gamma - 1}$ and substituting in the above equation results in:

$$\dot{U}_{ch} = \frac{d}{dt}(\frac{m_{ch} RT}{\gamma - 1}) \tag{38}$$

where γ is the ratio of the specific heat at constant pressure to the specific heat at constant volume, $\gamma = \frac{C_p}{C_v}$, and *R* is the gas constant. Using the ideal gas relationship *PV* = mRT_{ch}, equation (38) yields:

$$\dot{U}_{ch} = \frac{d}{dt}(\frac{PV}{\gamma - 1}) \tag{39}$$

The above equation can be rewritten as follows:

$$\dot{U}_{ch} = \frac{(P\dot{V} + \dot{P}V)}{\gamma - 1} \tag{40}$$

where P is the pressure in the CV; V is the volume of the CV.

(b) Determining Rate of change of Enthalpy

The rate of change of enthalpy is defined by the following relationship:

$$\dot{H}_{ch} = (\dot{H}_{ch})_{in} - (\dot{H}_{ch})_{out} \tag{41}$$

If the heat losses are neglected between the catalyst pack and the cylinder:

$$(\dot{H}_{ch})_{in} = (\dot{H}_{cat})_{out} \tag{42}$$

$(\dot{H}_{ch})_{out}$ in equation (41) can be calculated as follows:

$$(\dot{H}_{ch})_{out} = \dot{m}_e[x_{O_2}(C_p)_{O_2}T_{ex} + x_{H_2O_2}(h_f + xh_{fg})] \tag{43}$$

where $\dot{m}_e$ is the mass flow rate from the exhaust valve and can be calculated using equation (52) discussed in the next section, $(C_p)_{O_2}$ is the average specific heat of oxygen at a constant pressure, h_f is the specific enthalpy of saturated liquid, h_{fg} is the specific enthalpy of vaporization, x is the dryness fraction of steam, x_{O_2} and $x_{H_2O_2}$ are the fraction of oxygen and hydrogen peroxide per kilogram of the exhaust products (equation (18)), and T_{ex} is the temperature of the exhaust products.

(c) Determining Rate of Heat Loss

The equation of heat loss to the environment is similar to equation (24) defined for the catalyst pack and is given as follows:

$$\dot{Q} = \frac{k_{ch} A}{l}(T_{high} - T_{atm}) \tag{44}$$

For this case also, T_{high} is assumed as a constant for the purposes of calculating heat losses to the environment.

(d) Determining Rate of Change of Work Done

The rate of work done by the cylinder, $\dot{W}_{ch}$, can be calculated using the following relationship:

$$\dot{W}_{ch} = P\dot{V} \tag{45}$$

Substituting the expressions for $\dot{U}_{ch}$, $\dot{H}_{ch}$, and $\dot{W}_{ch}$ into equation (36) results in:

$$\frac{1}{\gamma - 1}(\dot{P}V + P\dot{V}) = (\dot{H}_{ch})_{in} - (\dot{H}_{ch})_{out} + \dot{Q} - P\dot{V} \tag{46}$$

Rearranging equation (46) yields:

$$\dot{P} = \frac{(\gamma - 1)[(\dot{H}_{ch})_{in} - (\dot{H}_{ch})_{out} + \dot{Q}] - \gamma(P\dot{V})}{V} \tag{47}$$

The rate of change of pressure inside each chamber can therefore be expressed as:

$$\dot{P}_{(a,b)} = \frac{(\gamma - 1)[(\dot{H}_{ch})_{in} - (\dot{H}_{ch})_{out} + \dot{Q}]_{(a,b)} - \gamma(P_{(a,b)}\dot{V}_{(a,b)})}{V_{(a,b)}} \tag{48}$$

where $P_{(a,b)}$ is the pressure of the chambers "a" and "b" of the cylinder respectively, and $V_{(a,b)}$ is the volume of each cylinder chamber. The volume in each chamber is related to the rod position *y* by:

$$V_a = A_a y \tag{49}$$

$$V_b = A_b(L - y) \tag{50}$$

where, A_a and A_b are the piston effective areas, and L is the stroke length of the piston. The position, y, of the piston is in turn obtained from the equation of motion which can be expressed as:

$$M\ddot{y} + B\dot{y} + F_f = P_a A_a - P_b A_b - P_{atm} A_r \tag{51}$$

where M is the mass of the piston-load assembly, B is the viscous friction coefficient, F_f is the Coulomb friction force, A_a and A_b are the piston effective areas, and A_r is the area of the rod.

The gas constant used in the above equations is the weighted average of gas constants of the steam and oxygen. This following relationship can be derived using Dalton's law of partial pressures (see [17]):

$$R_m = \frac{m_{steam} R_{steam} + m_{O_2} R_{O_2}}{m} \tag{52}$$

Similarly γ is also the weighted average of the specific heat ratios of steam and oxygen.

The equation (48) characterizes the input-output dynamic relationship of the actuator in figure 2-2. The same equation also characterizes the hot gas reservoir in the centralized configuration (Figure 2-2a). The output, $\dot{P}$, of this block is a function of two inputs. The first input, $(\dot{H}_{ch})_{out}$, is the enthalpy flow rate out of the chamber and the other input is the enthalpy flow rate, $(\dot{H}_{ch})_{in}$, entering the chamber.

3.4 Pneumatic Exhaust Valve

The mass flow rate through the pneumatic valve depends on the upstream and downstream pressures. The mass flow rate increases with the increase in the ratio of upstream to downstream pressure. The chocked condition occurs when the velocity of

flow through the valve orifice reaches the speed of sound, in which case the mass flow rate depends linearly on the upstream pressure. Below this velocity, the flow is unchoked and the mass flow rate is a non-linear function of upstream and downstream pressure. The flow rate under subsonic and sonic conditions are given as follows (refer [14,18])

$$\dot{m}_e = \frac{C_e A_e P_u}{\sqrt{T_e}} \sqrt{\frac{(2\gamma)}{(\gamma-1)R}\left((\frac{P_d}{P_u})^{2/\gamma} - (\frac{P_d}{P_u})^{(\gamma+1)/\gamma} \right)}, \quad \text{if } \frac{P_d}{P_u} > \left(\frac{2}{\gamma+1} \right)^{\gamma/(\gamma-1)} \tag{52}$$

$$\dot{m}_e = \frac{C_e A_e P_u}{\sqrt{T_e}} \sqrt{\frac{2\gamma}{\gamma+1}\left(\frac{2}{\gamma+1} \right)^{2/\gamma-1}} \quad \text{, otherwise}$$

where C_e is the discharge coefficient of the valve (a manufacturer provided parameter), A_e is the exhaust area of the valve, T_e is the exhaust temperature of the gaseous products, and P_u and P_d are the upstream and downstream pressures of the valve respectively, with P_d being atmospheric pressure in this case. Equation (52) characterizes the dynamics of the exhaust valve (refer to Figure 2-2), where the input to the block is the exhaust valve area and the output is the mass flow rate through the valve.

4. Experimental Setup and System Identification

Experiments were conducted to check the accuracy of the first-principles derived dynamic model. A schematic for the system setup is illustrated in Figure 2-1. The objective of the experiments was to measure the change of pressure in the cylinder for any given input to the binary on/off input valve or proportional exhaust valve as a function of time. These measured results were in turn compared to the corresponding output obtained by the derived dynamic model. The closeness of the response obtained

experimentally to the model based response will indicate the accuracy and correctness of the model.

For the experiment, two significantly different volume cylinders of different geometries were selected to show the model invariance to design changes. In the first setup (dash-dotted line of Figure 2-1a), a 300 cubic centimeter fixed volume cylinder was used as a reservoir. The propellant was stored in a stainless-steel blow-down propellant tank which was equipped with a pressure transducer (Omega PX200-200 GV). Liquid hydrogen peroxide with 70% concentration pressurized to 690 *kPa* (100 *psig*) with inert nitrogen gas was used in the experiment. A single solenoid-operated binary on/ off valve (Parker General Valve model 009-581-050-2) was used for controlling the flow of propellant from the blow-down tank. The catalyst pack that immediately follows the binary on/off valve was constructed in house and consists essentially of a 5-cm-long stainless-steel tube packed with the Shell 405 catalyst material. A thermocouple (Omega K-type) was attached to the catalyst pack to measure the rise in temperature. The catalyst pack was in turn connected to the hot gas pressure reservoir. The pressure in the reservoir was measured using a pressure transducer (Omega PX202-200 GV) attached to the reservoir.

In the experiment, hydrogen peroxide passes through the solenoid operated on/off inlet valve and the catalyst pack as commanded, and pressurizes the fixed volume cylinder. The inlet valve was opened for different time durations (from 1 second to 5 seconds) to measure the rise of pressure in the fixed volume cylinder. The valve was commanded using a Pentium 4 PC with an A/D card (National Instruments PCI-6031E).

The change in the pressure inside the fixed volume cylinder was recorded and compared with the model response to the same input.

In the second setup, the fixed volume cylinder was replaced with a variable volume (maximum volume of 58 cubic centimeters) pneumatic cylinder (Figure 2-1b) with a corresponding maximum stroke length of 4 inches. In addition, a 4-way solenoid valve (MicroAir Numatics) was modified to offer proportional operation and was utilized for discharging steam and oxygen from the cylinder to the atmosphere. Pressure sensors (EPXT Entran) were used to measure the pressures in the cylinder. For this experiment, a series of pulses of 50 milliseconds were given to the solenoid operated input valve. The corresponding rise of pressure in the chamber (chamber "a" of Figure 2-1b) was recorded and compared with the simulation results. Similarly, the exhaust valve was commanded to open for 120 milliseconds and the resulting drop in the pressure was recorded and compared to the simulation results. In this setup, relatively high supply pressure of 2.07 *MPa* (300 *psig*) was used. In another set of readings, the piston was set at different positions (therefore different volumes) and the pressure data was collected for the same input signal. The experiment was also repeated by continuously changing the position of the piston.

For evaluating the model response, the valve discharge coefficient of the hydraulic valve (C_d) was determined by measuring the mass of water flowing through the valve in a certain amount of time. The blow-down tank was filled with water and pressurized to 138 *kPa* (20 *psig*). The inlet valve was then commanded to open for 5 seconds and the water flowing out was measured for mass flow rate calculations. With this value of flow rate, the valve discharge coefficient was determined using equation (4).

The experiment was repeated for different supply pressures and for different opening times of the valve. The average discharge coefficient of 0.78 was then calculated based on the readings. The solid line in Figure 2-5 shows the plot of mass flow rates that were observed experimentally and the dashed line shows the calculated mass flow rate with the average discharge coefficient. Similarly, the valve discharge coefficient of the exhaust valve was determined experimentally using a Hastings Mass Flow-meter. Compressed air was used as the medium for the measurement of mass flow rate at different valve openings of the valve (not shown). The average discharge coefficient (C_d = 0.39) was then calculated using equation (52).

5. Results and Discussion

Figure 2-6 shows experimental and simulation results for the fixed volume cylinder. The dotted line in the figure shows the simulation pressure while the solid line shows the actual pressure rise in the fixed volume cylinder. As seen in the figure, there is a good agreement between the simulation and experimental results in terms of the pressure and the rate of pressure. Figure 2-6a shows the change in pressure when the inlet hydraulic valve was commanded to open for 1 second. As can be seen, the pressure increases rapidly up to 1 second and then starts to decrease slowly. The increase in the pressure is the result of heat produced due to the decomposition of hydrogen peroxide that passes over the catalyst when the valve is opened. The decrease in pressure is primarily because of the heat losses to the walls of the cylinder and to the environment. The actual drop in the pressure is observed to be little different than the simulation results. This is mainly due to the assumption made for calculating heat losses. Other

contributing factors for the deviation may include the presence of minor leakages in the cylinder through fittings. Figures 2-6b through 2-6e show the rise in pressure with the solenoid operated on/off inlet valve commanded to open for 2, 3, 4 and 5 seconds, respectively. Figure 2-6f shows the change in the pressure when the valve was commanded to open for one second and close for one second in a cycle.

The results for the variable volume cylinder are shown in Figures 2-7 and 2-8. Figure 2-7a shows the rise in the pressure when the position of the piston was set and held at 1 inch (volume: 14.5 cubic centimeters). The figure shows the rise in the pressure when a series of four 50 milliseconds pulses were given to the inlet hydraulic valve. The four series of data have been placed on the same figure for compactness, but each was a separate run where the initial pressure in the simulation was set to match the actual initial pressure. Figure 2-7b shows the drop in the cylinder pressure when the exhaust valve was opened for 120 milliseconds. Two separate cycles of the exhaust valve opening are shown in the figure. It was observed in the experiment that the recorded temperature of the exhaust products was close to the saturation temperature. This indicates that the quality of steam is between the saturated liquid and saturated steam. The enthalpy of steam flowing out of the cylinder was calculated using a steam look-up table. The best results were obtained when the dryness fraction of the steam was set to a value of 0.35.

Similarly, figure 2-8 shows the simulation and experimental results when the length of the piston was set and held at 4 inches (volume: 58 cubic centimeters). Figure 2-9 shows the change in pressure when the volume of the cylinder was changed continuously over a period of time by imposing a variable load on the output piston

during operation. A close agreement is observed between the simulation and experimental results.

In the simulation, most of the parameters of the model were set as per the values found in the literature. Some of the parameters (e.g., valve discharge coefficient, k_{cat}) were either identified experimentally or tuned for better results. For example, the value of the pre-exponential factor (K_o) ranges from 10^{14} to 10^{19} s^{-1} in literature. But the best results were obtained using the value of K_o as 10.10^{17} s^{-1}. One major intent of this work was to formulate a model that had a minimum number of empirical parameters. Of the empirical parameters left in the model presented, all are intuitive quantities with intuitive and fairly well decoupled influences. It is in this manner that the model is useful: all parameters can either be found in the literature or are well understood parameters with intuitive effects that can be measured or estimated. As was *not* the case with prior modeling work on this system, the model presented is derived using first principles and therefore contains only physically meaningful parameters. The values of all the parameters used for this experiment are presented in Table 2-1. Finally, it should be noted that it was observed that the effective area of the catalyst pack changes slowly over a period of time. This results in a change in the mass flow rate behavior and consequently the pressurization rate behavior of the cylinder. This slowly varying plant behavior can be addressed either by implementing a robust controller or by adapting this parameter in the control design.

6. Conclusion

The dynamic model of inlet hydraulic valve, catalyst pack, actuator, and the pneumatic exhaust valve was presented that is associated with a proposed monopropellant-based actuation system. This modeling effort was pursued using fundamental energetic principles in an effort to obtain a model with physically meaningful and well understood parameters. The motivation for obtaining the model was to describe the dynamics associated with either the centralized or direct injection configuration useful for purposes of control, and in part to aide in the development of such monopropellant-based actuation systems. An experimental verification of the model revealed good agreement with both dynamic and steady-state characteristics of the system.

References

[1] Barth, E. J., Gogola, M. A., Goldfarb, M., "Modeling and Control of a Monopropellant-Based Pneumatic Actuation System", IEEE International Conference on Robotics and Automation, Vol. 1, pp. 628-633, 2003.

[2] Morillon, J. G., "Development of High Level Robotic Functions for Mobile Combat Systems", *Unmanned Ground Vehicle Technology, Proceedings of SPIE – The International Society for Optical Engineering*, Vol. 5083, pp. 452-461, 2003.

[3] Glass, S. W., Ranson, C. C., Reinholtz, C. F., Calkins, J. M., "Modular Robotic Applications in Nuclear Power Plant Maintenance", *Proceedings of the 58th American Power Conference*, Vol. 58-1, pp. 421-426, 1996.

[4] Roman, H. T., "Robots Cut Risks and Costs in Nuclear Power Plants", *IEEE Computer Applications in Power*, Vol. 4, Issue 3, pp. 11-15, 1991.

[5] Pellerin, C., "Service Robots in the 1990s", *Industrial Robot*, Vol. 20, no. 3, pp. 34-35, 1993.

[6] Mae, Y., Arai, T., Inoue, K., Yoshida, A., Miyawaki, K., Adachi, H., "Locomotive Working Robots in Rescue Operations", *International Journal of Robotics and Automation*, Vol. 18, no. 4, pp. 153-159, 2003.

[7] Katz, D. S., Some, R. R., "NASA Advances Robotic Space Exploration", *Computer*, Vol. 36, pp. 52-61, 2003.

[8] Barth, E. J., Gogola, M., Wehrmeyer, J. A., Goldfarb, M., "The Design and Modeling of a Liquid-Propellant-Powered Actuator for Energetically Autonomous Robots", *ASME International Mechanical Engineering Conference and Exposition (IMECE)*, 2002.

[9] Hearn, H. C., "Performance Prediction Model for a High-Impulse Monopropellant Propulsion System", *Journal of Spacecraft and Robots*, vol. 11, no. 11, pp. 764-768, 1974.

[10] Hitt, D. L., "MEMS-Based Satellite Micropropulsion via Catalyzed Hydrogen Peroxide Decomposition", *Smart Materials and Structures*, vol. 10, no. 6, pp. 1163-1175, 2001.

[11] Shearer, J. L., "Study of Pneumatic Processes in the Continuous Control of Motion with Compressed Air – I", *Transactions of the ASME*, vol. 78, pp. 233-242, 1956.

[12] Shearer J. L., ""Study of Pneumatic Processes in the Continuous Control of Motion with Compressed Air – II", *Transactions of the ASME*, vol. 78, pp. 243-249, 1956.

[13] Bobrow, J., and McDonell, B., "Modeling, Identification, and Control of a Pneumatically Actuated, Force Controllable Robot," *IEEE Transactions on Robotics and Automation*, vol. 14, no. 5, pp. 732-742, 1998.

[14] Richer, E., Hurmuzlu, Y., "A High Performance Pneumatic Force Actuator System: Part I – Nonlinear Mathematical Model", *ASME Journal of Dynamic Systems, Measurement, and Control*, Vol. 122, no. 3, pp. 426-434, 2000.

[15] Goldfarb, M., Barth, E. J., Gogola, M. A., Wehrmeyer, J. A., "Design and Energetic Characterization of a Liquid-Propellant-Powered Actuator for Self Powered Robots", *IEEE/ASME Transactions on Mechatronics*, Vol. 8, no. 2, pp. 254-262, 2003.

[16] Khoumeri, B., Balbi, N., Leoni, E., Chiaramonti, N., Balbi, J.H., "The Decomposition of Hydrogen Peroxide – A non-linear dynamic model", *Journal of Thermal Analysis and Calorimetry*, Vol. 59 (2000), 901-911.

[17] Avallone, E., "*Mark's Standard Handbook for Mechanical Engineers*", McGraw-Hill, Inc., New York, 1987.

[18] Ogata, K., "*System Dynamics*", Prentice-Hall, Inc., Eaglewood Cliff, New Jersey, 1978.

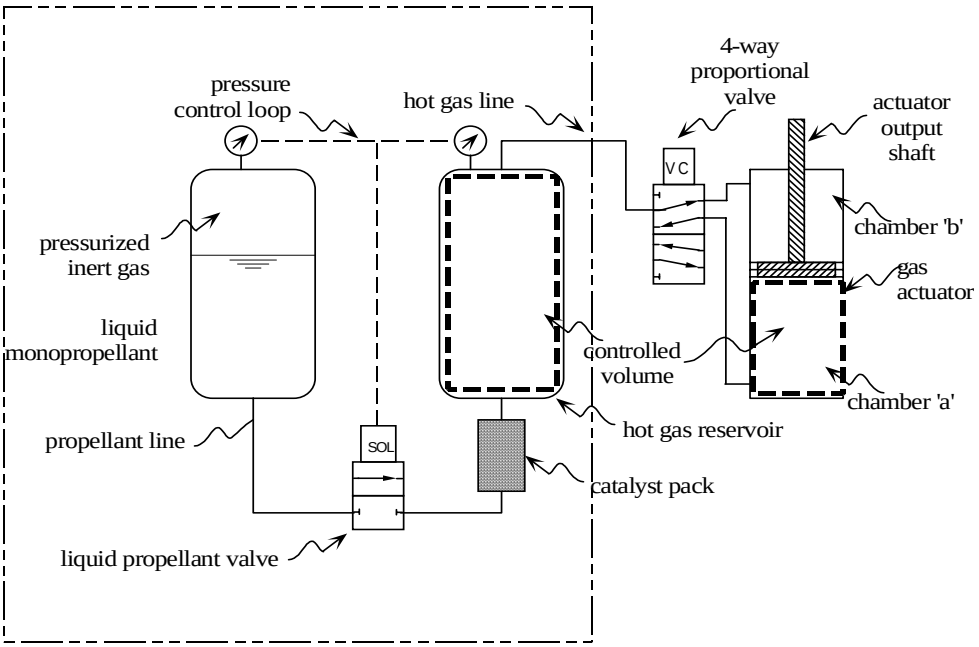

Fig 2-1a. Schematic of the centralized monopropellant actuation system.

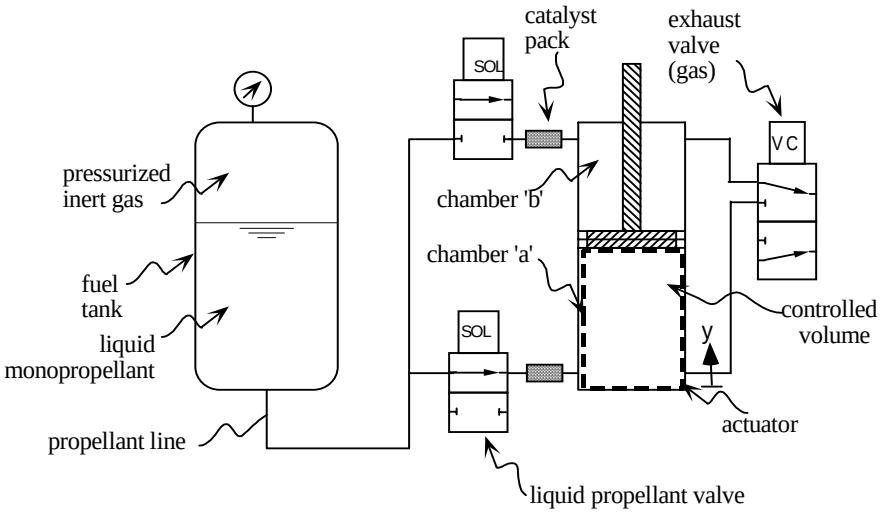

Fig 2-1b. Schematic of the direct injection monopropellant actuation system.

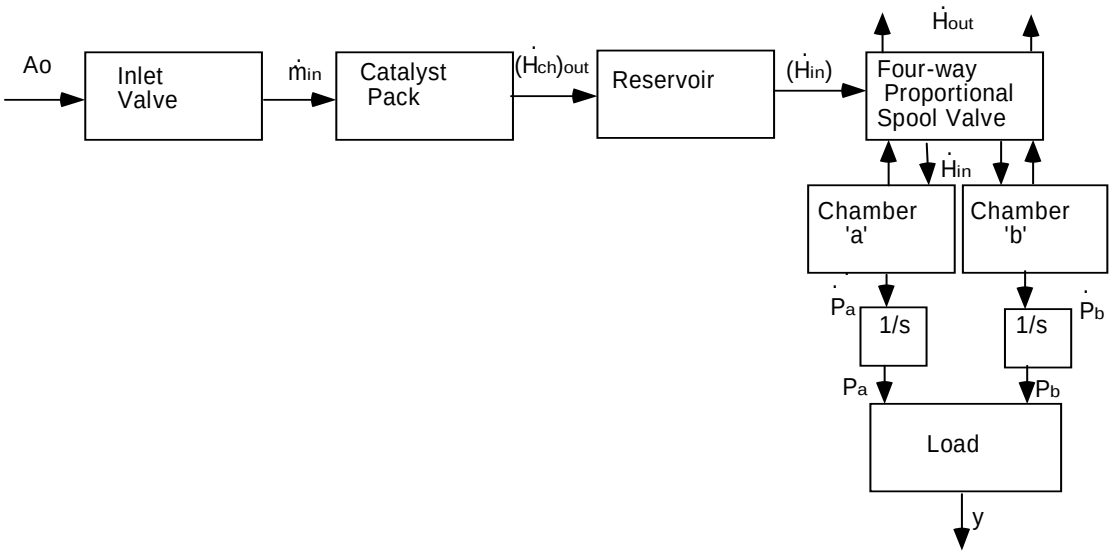

Fig 2-2a. Block diagram of the centralized configuration of the chemofluidic actuation system.

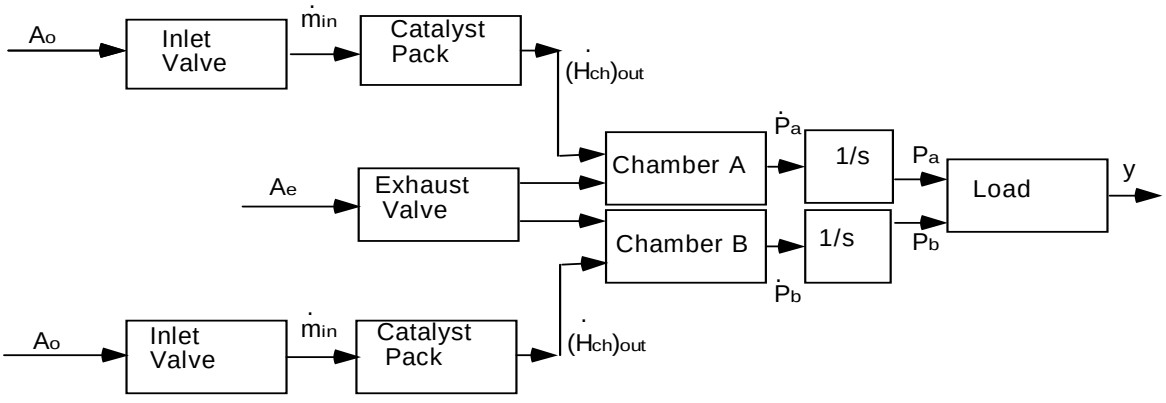

Fig 2-2b. Block diagram of the direct injection configuration of the chemofluidic actuation system

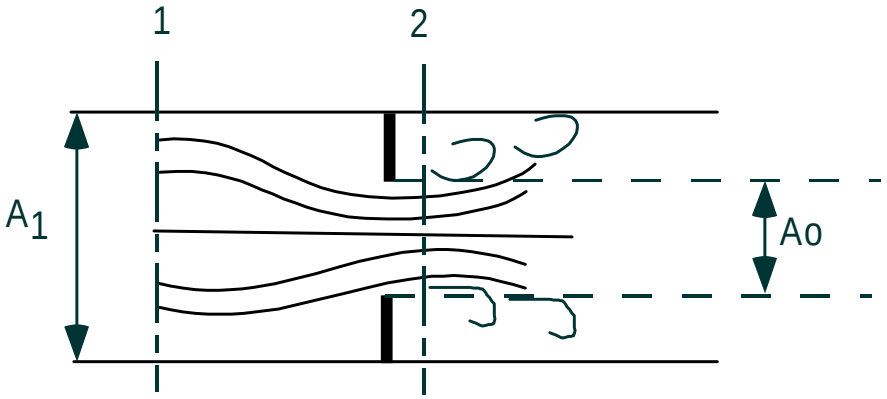

Fig 2-3. Steady flow of a liquid through an orifice.

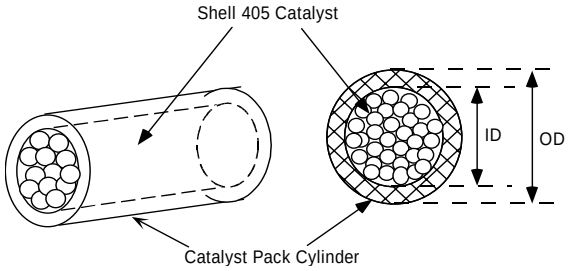

Fig 2-4a. Catalyst Pack - Actual

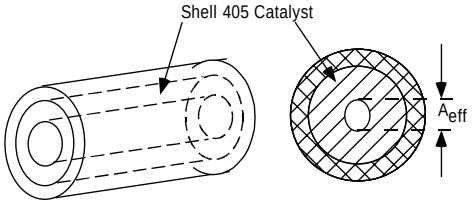

Fig 2-4b. Catalyst Pack as Modeled

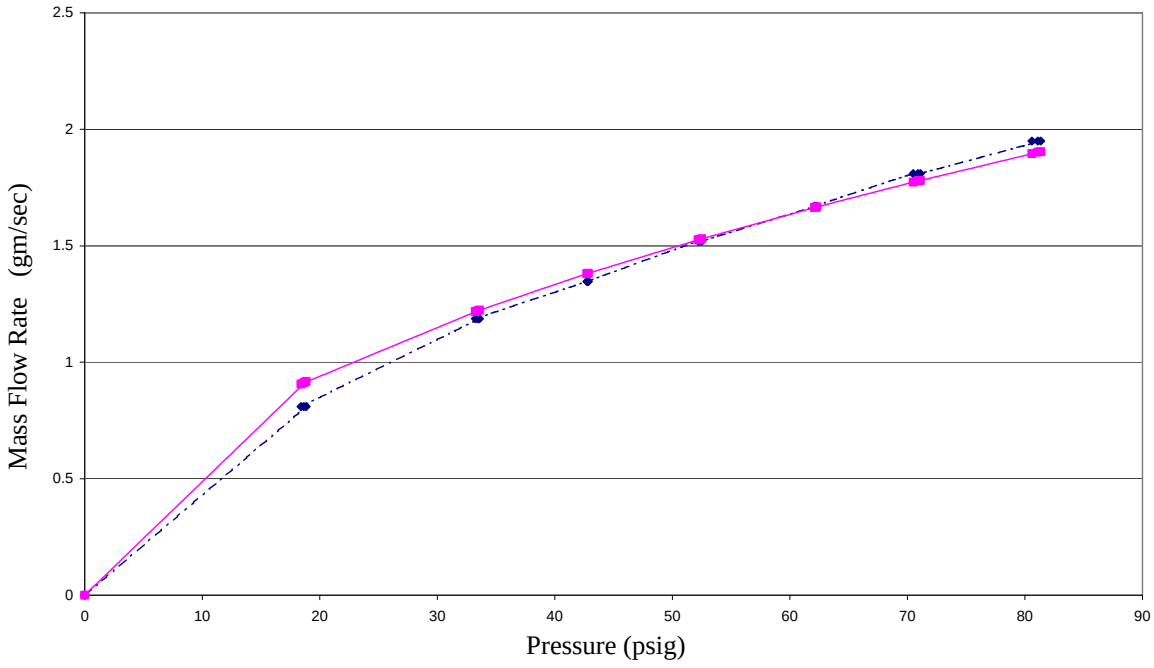

Fig 2-5. Plot showing the mass flow rate of the inlet hydraulic valve as a function of the pressure drop across the valve. The points on the solid line are the measured mass flow rates, and the points on the dashed line are the modeled mass flow rates using the average discharge coefficient.

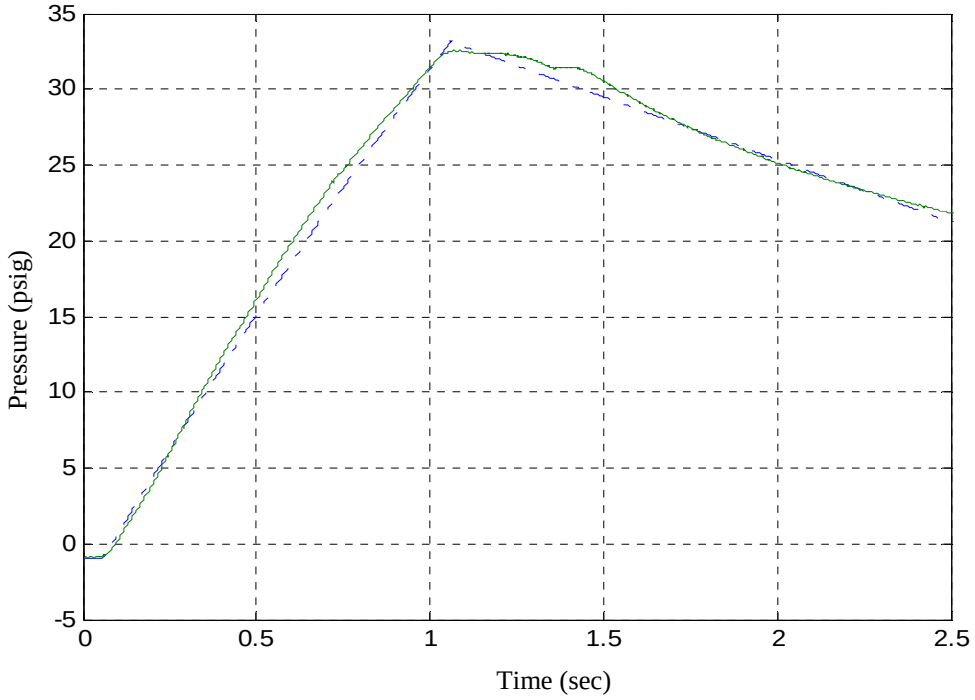

Fig 2-6a. Change in pressure inside the fixed volume cylinder with an inlet hydraulic valve opening time of 1 second. The solid line is the actual pressure and the dashed line is the modeled pressure.

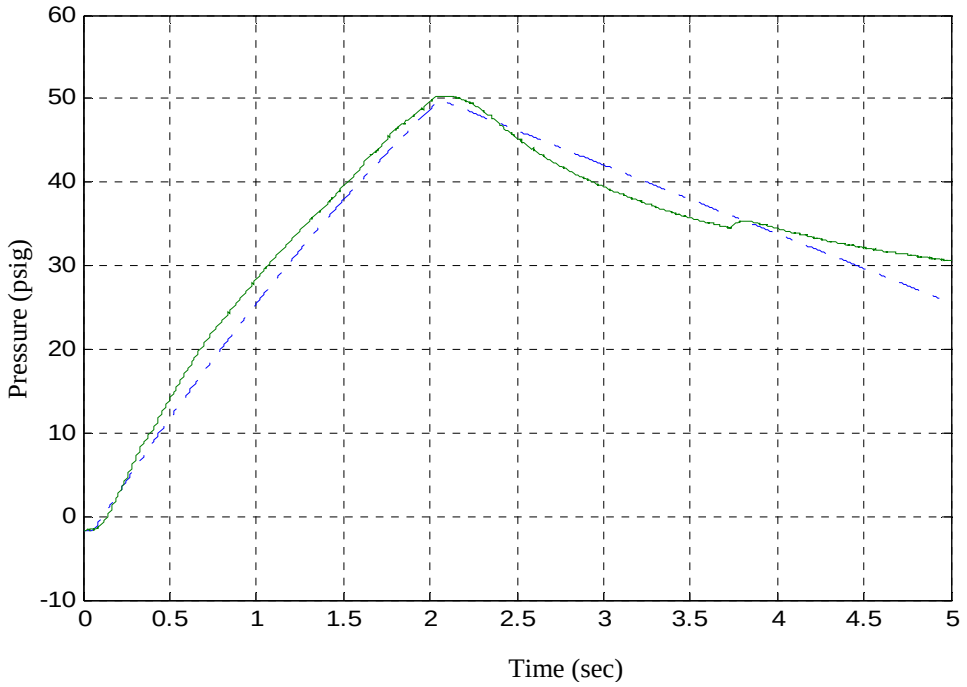

Fig 2-6b. Change in pressure inside the fixed volume cylinder with an inlet hydraulic valve opening time of 2 seconds. The solid line is the actual pressure and the dashed line is the modeled pressure.

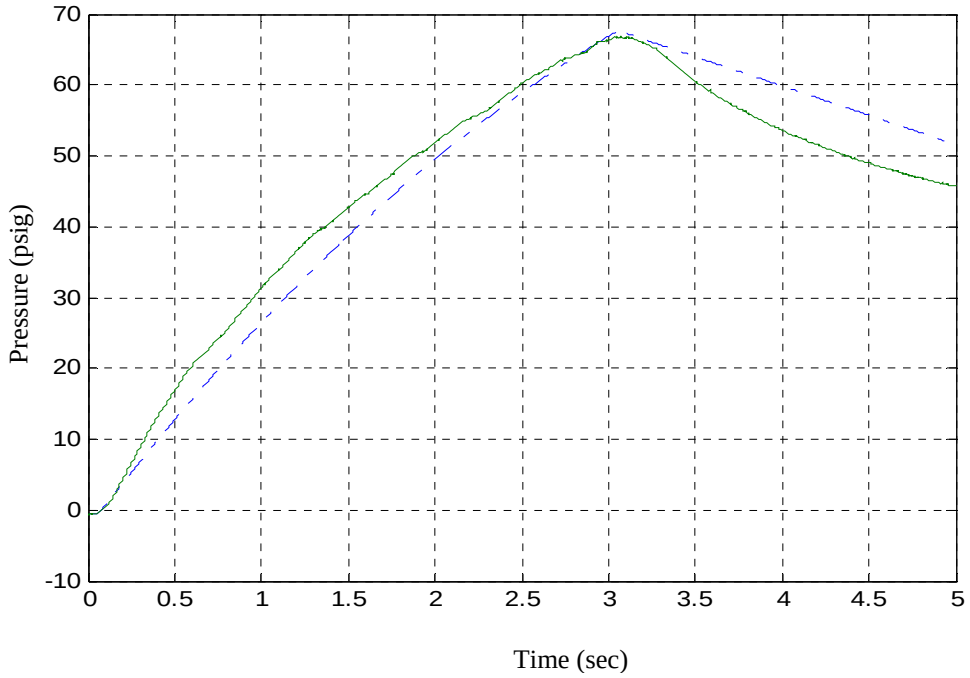

Fig 2-6c. Change in pressure inside the fixed volume cylinder with an inlet hydraulic valve opening time of 3 seconds. The solid line is the actual pressure and the dashed line is the modeled pressure.

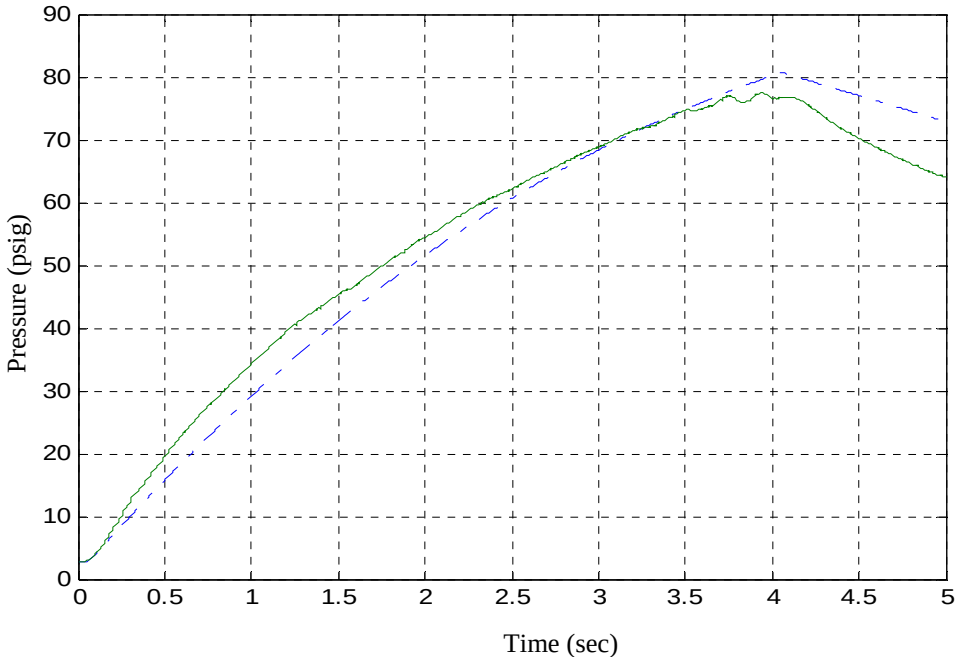

Fig 2-6d. Change in pressure inside the fixed volume cylinder with an inlet hydraulic valve opening time of 4 seconds. The solid line is the actual pressure and the dashed line is the modeled pressure.

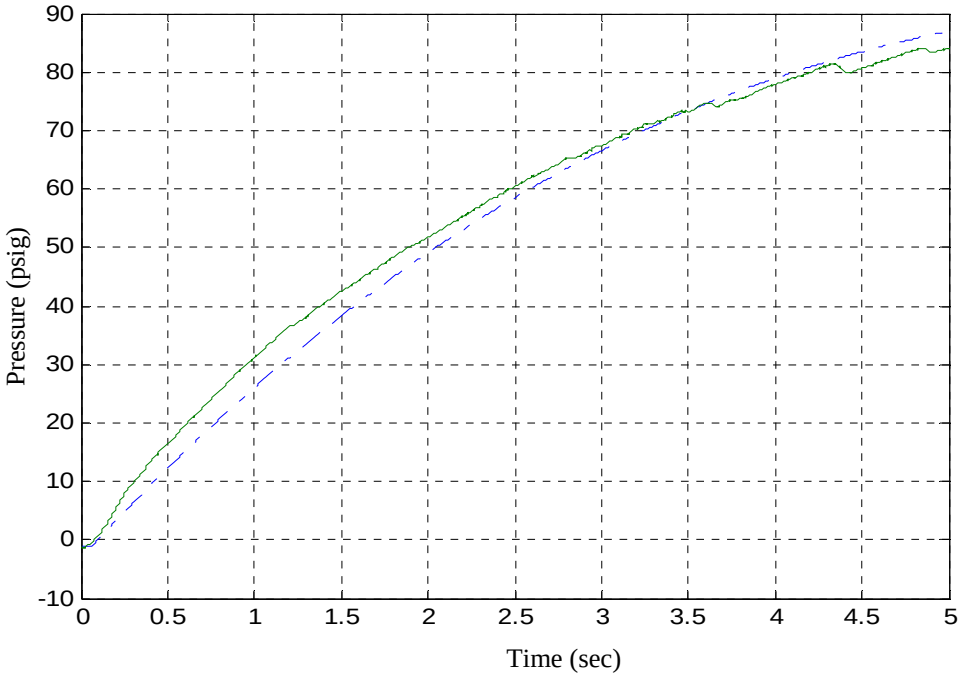

Fig 2-6e. Change in pressure inside the fixed volume cylinder with an inlet hydraulic valve opening time of 5 seconds. The solid line is the actual pressure and the dashed line is the modeled pressure.

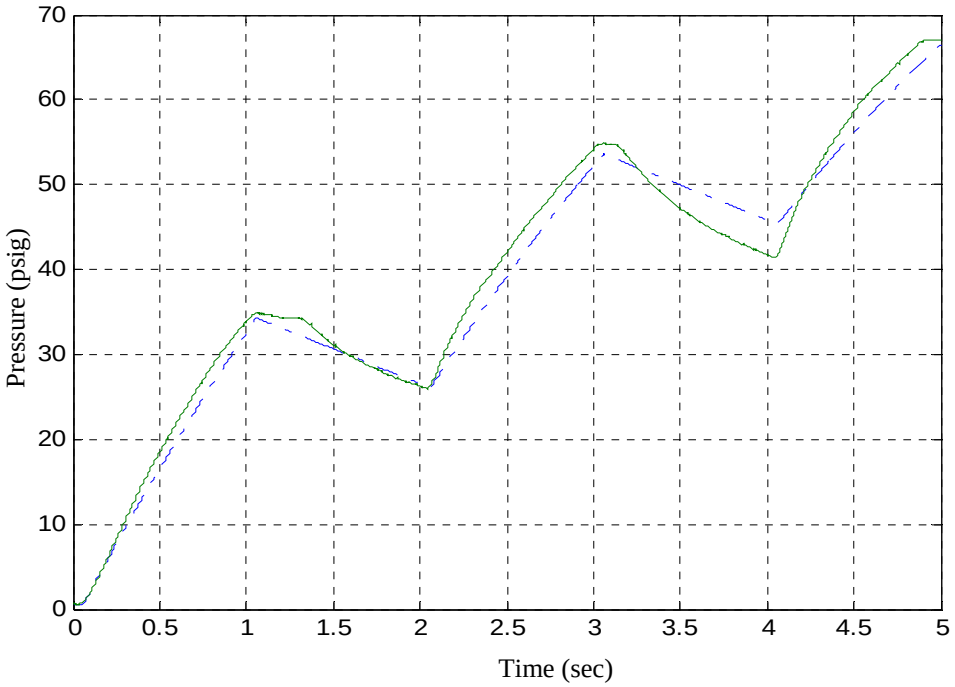

Fig 2-6f. Change in pressure inside the fixed volume cylinder with a cyclic opening and closing of the inlet valve for 1 second. Solid = actual pressure, dashed = modeled pressure.

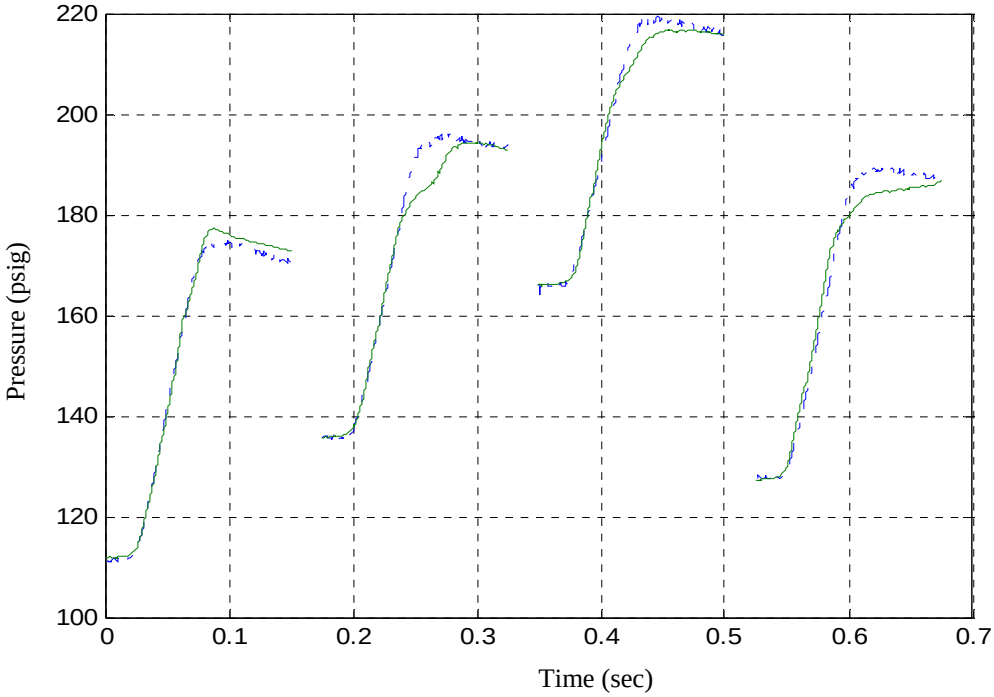

Fig 2-7a. Change in pressure inside the variable volume cylinder held at a 1 inch stroke length with a commanded inlet hydraulic valve opening time of 50 ms for four separate runs. Solid = actual pressure, dashed = modeled pressure.

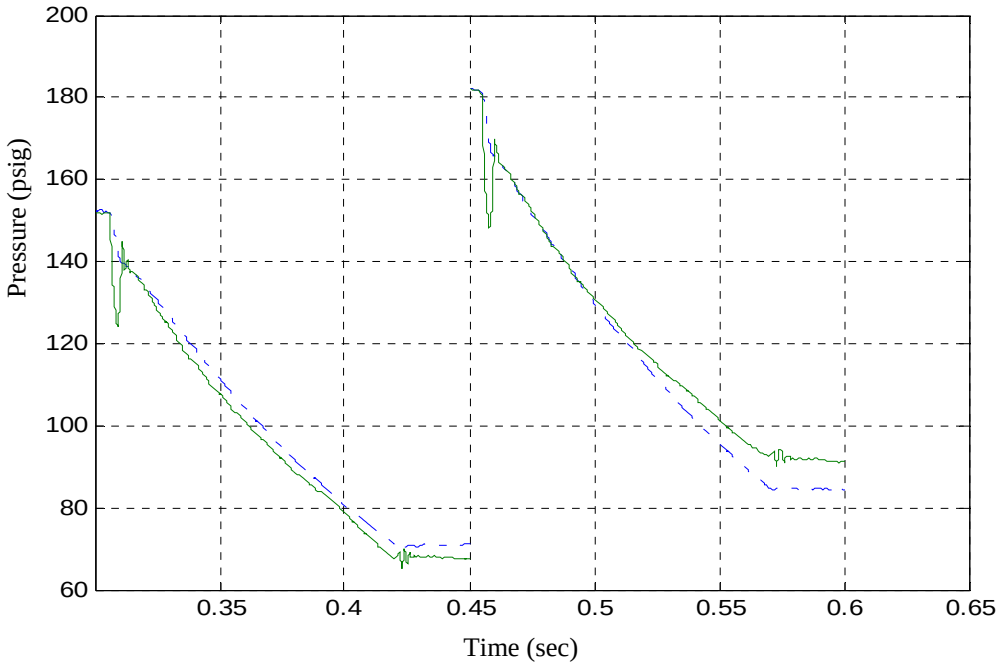

Fig 2-7b. Change in pressure inside the variable volume cylinder held at a 1 inch stroke length with a commanded exhaust valve opening time of 120 ms for two separate runs. Solid = actual pressure, dashed = modeled pressure.

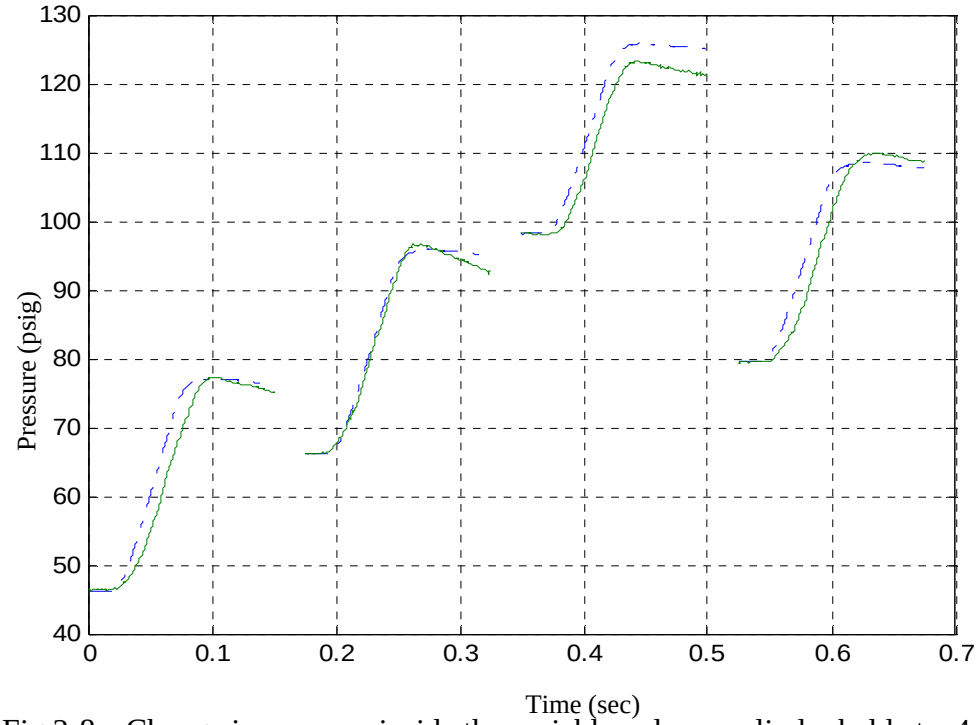

Fig 2-8a. Change in pressure inside the variable volume cylinder held at a 4 inch stroke length with a commanded inlet hydraulic valve opening time of 50 ms for four separate runs. Solid = actual pressure, dashed = modeled pressure.

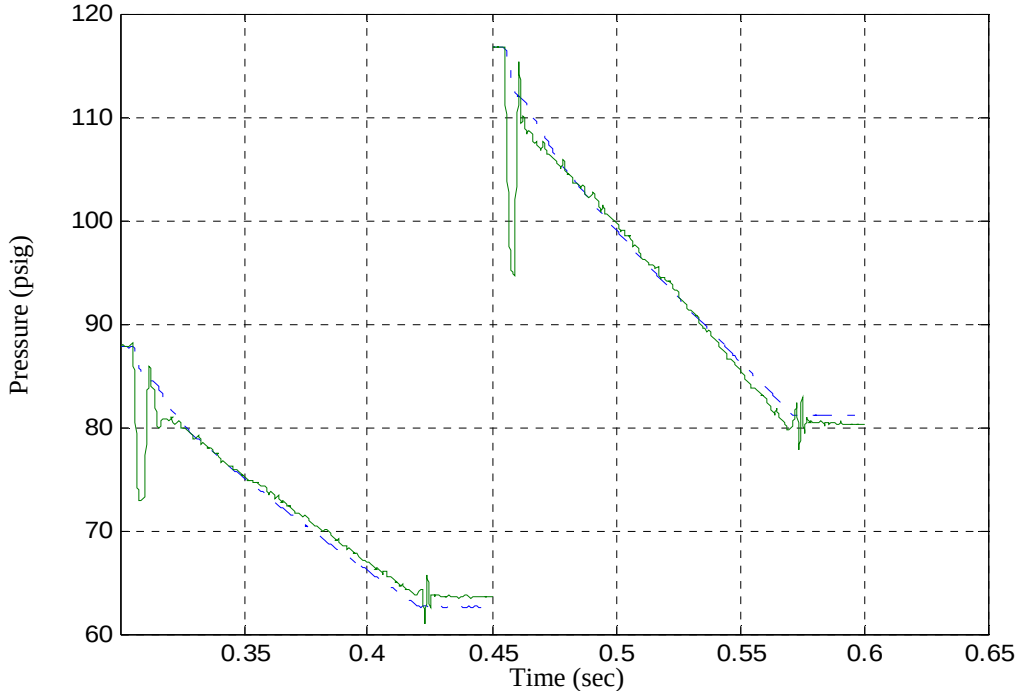

Fig 2-8b. Change in pressure inside the variable volume cylinder held at a 4 inch stroke length with a commanded exhaust valve opening time of 120 ms for two separate runs. Solid = actual pressure, dashed = modeled pressure.

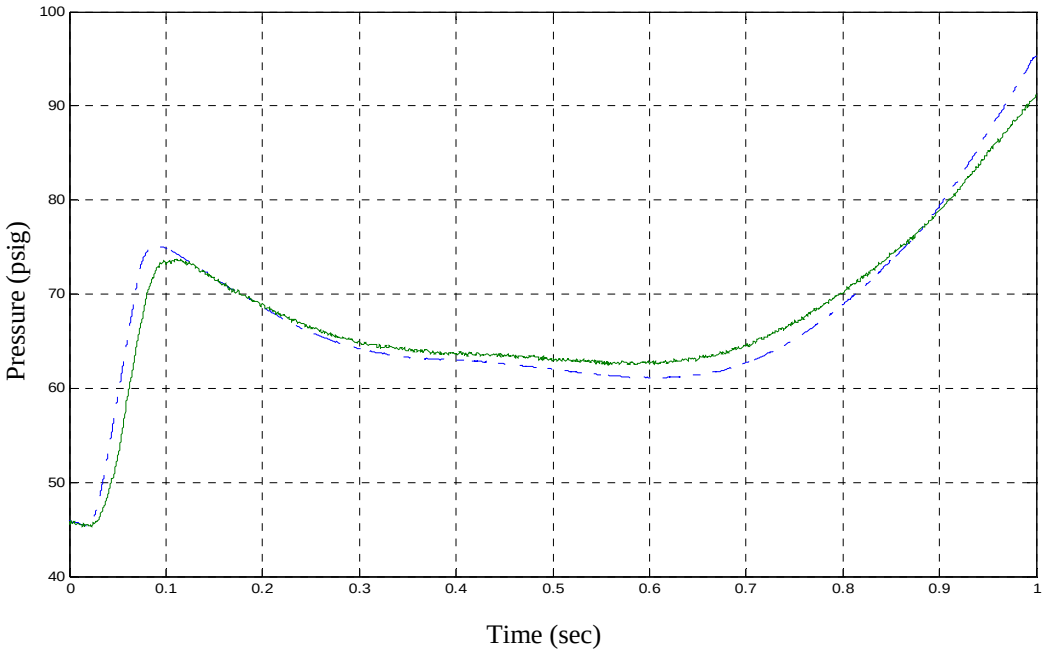

Fig 2-9. Change in pressure inside the variable volume cylinder with an inlet hydraulic valve opening time of 50 ms and a variable stroke length imposed by a variable load on the piston.

Table 2-1: Values of Parameters used in the Experiment

Symbol	Value
C_d	0.78
A_0	7.3e-9 m^2
A_{cat}	7e-9 m^2
ρ	1035 Kg/ m^3
C_p	725.1 cal/ Kg-^{0}C
K_o	10e17 s^{-1}
E_a	106.9 kJ/mol
R	8.3145 kJ/ kmol-K
K_{cat}	0.08
γ	1.327
K_{ch}	0.1
R_m	394.96 J/ Kg-K
C_e	0.4
P_{cr}	0.541

CHAPTER III

MANUSCRIPT II

LYAPUNOV-BASED PRESSURE OBSERVER DESIGN AND SERVO CONTROL OF PNEUMATIC ACTUATORS

Navneet Gulati and Eric J. Barth

Department of Mechanical Engineering

Vanderbilt University

Nashville, TN 37235

Submitted as a Full Paper to the

ASME/ IEEE Transactions on Mechatronics

Abstract

Pneumatic actuators are highly non-linear by their nature. Thus, the robust precision dynamic control output of pneumatic systems requires model-based control techniques such as sliding mode and adaptive control. These controllers require full state knowledge of the system, viz. pressure, position, and velocity. For measuring two of the states, pneumatic servo systems require two expensive pressure sensors per axis, and hence it makes the system economically non-competitive with most electromagnetic types of actuation. This paper presents the development of two Lyapunov-based pressure observers for the pneumatic actuator system. The first method shows that an energy-based stable pressure observer can be developed with the state equations. The other method incorporates the output error to control the convergence of the observed pressures. A robust observer-based controller is further developed to obtain a low cost precision pneumatic servo system. Simulation and experimental results are presented that demonstrate and validate the effectiveness of the proposed observers.

1. Introduction

A schematic of a pneumatic servo system is depicted in Figure 3-1. A typical setup consists mainly of a pneumatic cylinder, valves, and sensors. In this system, the output position is controlled by a force that arises from the pressure differential across the piston in the cylinder. The time derivative of the pressure differential is a non-linear function of the mass flow rate in the cylinder chamber via a spool valve, as well as the volumes and rates of change of the volumes of the two sides of the cylinder. The mass flow rate, in turn, is a nonlinear function of the valve position, which is also the control

input to the system, as well as the cylinder pressures, supply pressure and atmospheric pressure. As a result, the dynamics of such a system that relates control input to the position output is highly non-linear. An additional cause of non-linearity is the seal friction between the piston and the cylinder, and any friction that may be associated with the motion of the load. The prime cause of non-linearity is the compressibility of air, which results specifically in two non-linear components of the system dynamics. The first is the non-linear relationship that describes the compliance of an ideal gas in each side of the cylinder. The second hard non-linearity is due to the saturation of the mass flow rate through the valve at sonic flow conditions. The mass flow rate through the valve initially depends both on the upstream and downstream pressures and increases with the pressure difference. Once the velocity of air at the venturi of the valve orifice reaches the speed of sound, i.e. sonic, the mass flow rate is only a linear function of the upstream pressure. This is because pressure disturbances travel at the speed of sound and hence at a sonic flow condition, the changes in the downstream pressure cannot travel upstream quickly enough to affect the upstream flow. The transition of flow rate between choked and unchoked condition is inevitable for any reasonable operating regime of desired motion control. The only potential way of avoiding this transition is to reduce the supply pressure to a very low level (~200 kPa). However, this low supply pressure renders the system almost useless as such a system would suffer from an extremely low output impedance and severe power limitations. As such, pressure sensors are commonly employed in non-linear model-based controllers of pneumatic servo systems in order to detect and compensate for the shift in dynamic behavior that occurs in the transition between chocked and unchoked flow through the valve.

Pressures in the cylinder are commonly used as states in precision pneumatic servo actuation systems. The other commonly used states to characterize this system are velocity of the piston, and the position. The measurement of pressures characterizes the energy storage in the cylinder mainly due to the compressibility of air. Similarly, measurement of velocity characterizes the energy stored in the load inertia. A typical pneumatic system employs two pressure sensors, and a linear potentiometer to measure the states of the system. In general, the velocity signals are obtained by numerical or analog differentiation of the position signals with a first or second order filter. The requirement for pressure sensing in a pneumatic servo system is particularly burdensome because high-bandwidth, high-pressure sensors required for the control of pneumatic servo systems are expensive and large (relative to the actuator), with a typical cost between $250 and $500. Since pneumatic systems require use of two pressure sensors per axis, these sensors add $500 to $1000 per axis of a pneumatic servo system. Coupled with valve and cylinder costs, pneumatic systems are not cost-competitive with power comparable electromagnetic types of actuation. If the requirement of pressure sensors can be eliminated by constructing observers to estimate these states, it will result in an average savings of approximately 30 percent in initial costs. Since the other states (viz. motion output and velocity) are measurable, the possibility exists to reconstruct the cylinder pressures by using the available knowledge of the inputs and the other states of the system. It should be noted that the requirement of pressure measurement can be avoided by the use of non-model based controllers, such as the position-velocity-acceleration (PVA) controller structure [1]. Although such controllers have met with a certain amount of success, non-model based controllers cannot address the often

significant nonlinearities associated with pneumatic systems. It has been pointed out by Pandian et. al. [2] that for the precise and robust control performance, the use of pressure states is essential.

Despite a number of prior publications on control methodologies that require full state measurement [3-9], few works explicitly consider the initial/operating cost associated with pneumatic systems. Pandian et. al. [4] presented a sliding mode controller for position control that showed good results at lower frequencies. Richer and Hurmuzlu [7] in their work presented the design of a sliding-mode force controller and showed a good response up to 20 Hz sinusoidal frequency. All these developed controllers concentrated on the position and/or force tracking accuracy and ignored the energetic efficiency and/or initial costs associated with the control system. Many authors focused on the development of more energy efficient controllers to reduce the operating cost of the system. Sanville [10] suggested a use of a secondary reservoir in an open-loop system to collect exhaust air. This air was in turn utilized as an auxiliary low-pressure supply. Al-Dakkan [11] et al. presented a control methodology that provides significant energy savings. They used two three-way spool valves, instead of a conventional four-way proportional spool valve, and introduced a dynamic constraint equation that minimizes cylinder pressures resulting in lower energy consumption. In other efforts to reduce initial costs, Ye et al. [12], Kunt and Singh [13], Lai et al. [14], Royston and Singh [15], Paul et al. [16], and Shih and Hwang [17] demonstrated the viability of servo-control of pneumatic actuators via solenoid on/off valves in place of proportional valves.

Though all these efforts were made to reduce initial and operating costs, the components of the pneumatic system still remained expensive. In the continuing efforts

to achieve higher cost savings, Pandian et al. [2] in their work presented two methods for observing pressure in an effort to eliminate costly pressure sensors. In the first method, a continuous gain observer design, the pressure is measured in one chamber and the pressure in another chamber is observed – thereby eliminating one of the two pressure sensors. In this case, a choked flow condition is assumed by the authors. In addition, mass flow rate is assumed to be known while deriving the error equation. Both of these assumptions are restrictive since at a low pressure difference across the control valve, the flow rate is not choked. Also, the mass flow rate is a function of pressure whose value is to be estimated. In the second method, a sliding-mode pressure observer design, the same assumptions of the first method were used. In this method, the difference between the estimated and actual pressure in one chamber is treated as a disturbance and the pressure in another chamber is observed using a sliding-mode observer design. However the convergence of the error to zero is not clear, as the disturbance, which is the non-homogenous part or driving term of the desired error dynamic differential equation, can lead to large steady state error. In another development, Bigras and Khayati [18] presented a design of a pressure observer for a pneumatic cylinder system for which the connection ports provide a considerable restriction to the air supply. The observer was based on the measurement of actual pressure outside the cylinder and hence pressure sensors cannot be eliminated from the system. Wu et al. [19], based on a rank condition test concluded that pressure states are not observable from the measurement of motion output alone because of the existence of singular points when the system is at rest.

In this paper, two Lyapunov based pressure observer designs are presented. It is shown that the error between the observed and actual observed states converges to zero

by including knowledge of valve spool position as well as the motion states of the system. At singular points, it can be shown that the error will not diverge away from the actual values. At all other points, both observer designs are shown to have analytical convergence of the error between the actual pressure and the observed pressure. However, and inevitably, the observer experimentally shows some amount of inaccuracy in the observed values of the pressures. Therefore, a robust controller based on sliding mode control theory is developed in this paper to take into account observer error along with the uncertainties present in the system model, like friction, to obtain a low cost pneumatic servo system. The organization of this paper is as follows. In the next section, a model of the pneumatic system is presented. In section 3, the design and analytical properties of two observers, an energy-based Lyapunov observer and a force-error based observer is derived. Section 4 presents the design of a sliding mode controller for the servo control of pneumatic system shown in Figure 3-2. In section 5 and 6, the experimental setup, implementation, and results are discussed.

2. Model of a Pneumatic Servo Actuator

A model of the standard pneumatic servo actuator is reasonably standard and is derived in many texts and papers [20-23]. A complete model of the system was presented by Richer and Hurmuzlu [24], where they considered valve dynamics as well as the time delay and attenuation associated with pneumatic lines. The salient features of the standard dynamic model are summarized in this paper. The dynamic equation for the piston-rod-load assembly shown in Figure 3-1 is derived using a force balance equation (Newton's second law) and can be expressed as:

$$M\ddot{x} + B\dot{x} + F_c = P_a A_a - P_b A_b - P_{atm} A_r \tag{1}$$

where, M (kg) is the mass of the load; B is the viscous friction coefficient; F_c (N) is the Coulomb friction; P_a and P_b (N/m^2 or Pa) are the absolute pressure in each chamber of the cylinder, P_{atm}(N/m^2 or Pa) is the absolute environmental pressure; A_r (m^2) is the cross-sectional area of the rod, and A_a and A_b (m^2) are the effective piston areas in chambers 'A' and 'B', respectively.

The dynamics of the chamber pressures P_a and P_b can be derived by utilizing the first law of thermodynamics and assuming no heat loss occurs in the cylinder. The resulting first order differential equation is as follows:

$$\dot{P}_{(a,b)} = \frac{\gamma RT}{V_{(a,b)}} \dot{m}_{(a,b)} - \frac{\gamma \dot{V}_{(a,b)}}{V_{(a,b)}} P_{(a,b)} \tag{2}$$

where γ is the ratio of the specific heat at constant pressure (C_p) to the specific heat at constant volume (C_v), $\gamma = {C_P}/{C_v}$; R ($J/kg\text{-}K$) is the gas constant; V (m^3) is the volume of the chamber; subscripts 'a' and 'b' represents properties of chambers 'A' and 'B' respectively. As per the sign convention used in this paper, $\dot{m}$ is positive while charging the cylinder and negative during discharge to the atmosphere.

The pressure dynamics are governed in part by the mass flow rate term, which in turn is directly influenced by the commanded flow orifice area of each valve. The relationship between the valve area and the mass flow rate of air is derived by assuming that the flow through the valve is an ideal gas undergoing an isentropic process, which leads to the commonly accepted mass flow rate expressions for a converging nozzle:

$$\dot{m} = \frac{C_e A_v p_u}{\sqrt{T}} \sqrt{\frac{(2\gamma)}{(\gamma-1)R}\left((\frac{p_d}{p_u})^{2/\gamma} - (\frac{p_d}{p_u})^{(\gamma+1)/\gamma} \right)}, \quad \text{if } \frac{p_d}{p_u} > \left(\frac{2}{\gamma+1}\right)^{\gamma/(\gamma-1)} \tag{3}$$

$$\dot{m} = \frac{C_e A_v p_u}{\sqrt{T}} \sqrt{\frac{2\gamma}{\gamma+1}\left(\frac{2}{\gamma+1}\right)^{2/\gamma-1}}, \quad \text{if } \frac{p_d}{p_u} \leq \left(\frac{2}{\gamma+1}\right)^{\gamma/(\gamma-1)}$$

where C_e is the discharge coefficient of the valve – typically well characterized by the valve manufacturer; A_v (m^2) is the flow orifice area of the valve; T *(K)* is the inlet temperature of the gas; p_u and p_d (N/m^2 or Pa) is the upstream and downstream pressure respectively. It should be noted that during the charging process p_u is the supply pressure and p_d is the chamber pressure of the cylinder. While in the case of the discharging, p_u is the chamber pressure and p_d is the atmospheric pressure. As previously described, the chocked condition occurs when the velocity of flow through the valve reaches the speed of sound (the conditional statement of equation (3)), in which case the mass flow rate depends linearly on the upstream pressure. Below this velocity, the flow is unchoked and the mass flow rate is a non-linear function of upstream and downstream pressure.

The complete system dynamics of the pneumatic servo actuator are therefore characterized by the state vector $\mathbf{x}^T = [x\ \dot{x}\ P_a\ P_b]$ and the input $\mathbf{u} = [A_{v_a}\ A_{v_b}]$ and described by the combination of equations (1-3), where a positive valve area indicates a connection to the supply pressure (charge), and a negative valve area indicates a connection to the atmosphere (discharge). The volume and rate of change of volume are algebraically related to the displacement and velocity of the piston, and therefore do not give rise to independent states.

3. Observers

3.1 Energy-Based Lyapunov Observer Design

In this method, a Lyapunov function is chosen based on the pneumatic energy stored in the system. The pressure is estimated based on the following observer equations:

$$\dot{\hat{P}}_a = \frac{RT}{V_a}\dot{\hat{m}}_a - \frac{\dot{V}_a}{V_a}\hat{P}_a \tag{4}$$

$$\dot{\hat{P}}_b = \frac{RT}{V_b}\dot{\hat{m}}_b - \frac{\dot{V}_b}{V_b}\hat{P}_b$$

where, $\hat{P}$ in the above equations represents the estimated pressure and $\dot{\hat{m}}$ represents the estimated mass flow rate according to equation (3) based on the estimated pressure and the known valve orifice area $A_{V_{(a,b)}}$. Although equations (4) appear to be simply an open-loop estimation based on an isothermal assumption of the pressure dynamics of equations (2), they are actually closed-loop observers due to the relationship between $\hat{P}$ and $\dot{\hat{m}}$. In order to show the convergence between the actual pressures and the estimated pressures obtained from the above equations, the following positive definite candidate Lyapunov function is chosen for this method:

$$V = \frac{1}{2}(\tilde{P}_a V_a)^2 + \frac{1}{2}(\tilde{P}_b V_b)^2 \tag{5}$$

where, $\tilde{P}_a$ and $\tilde{P}_b$ represents the error between the actual pressure and the estimated pressure in chambers 'A' and 'B' respectively ($\tilde{P}_{(a,b)} = P_{(a,b)} - \hat{P}_{(a,b)}$). It should be noted that the Lyapunov function chosen is based on the energy stored in the cylinder of a

pneumatic system and represents the difference between the actual and observed stored energies.

Equation (5) can be rewritten as:

$$V = \frac{1}{2}(P_a V_a - \hat{P}_a V_a)^2 + \frac{1}{2}(P_b V_b - \hat{P}_b V_b)^2 \tag{6}$$

Differentiating equation (6) results in:

$$\begin{aligned} \dot{V} = (P_a V_a - \hat{P}_a V_a)(\dot{P}_a V_a + P_a \dot{V}_a - \dot{\hat{P}}_a V_a - \hat{P}_a \dot{V}_a) + \\ (P_b V_b - \hat{P}_b V_b)(\dot{P}_b V_b + P_b \dot{V}_b - \dot{\hat{P}}_b V_b - \hat{P}_b \dot{V}_b) \end{aligned} \tag{7}$$

If the process of charging and discharging of air in the cylinder is considered as isothermal (i.e., $\gamma = 1$), then using equation (2) the following substitutions can be made in equation (7):

$$\dot{P}_{(a,b)} V_{(a,b)} + P_{(a,b)} \dot{V}_{(a,b)} = RT\dot{m}_{(a,b)} \quad \text{and} \quad \dot{\hat{P}}_{(a,b)} V_{(a,b)} + \hat{P}_{(a,b)} \dot{V}_{(a,b)} = RT\dot{\hat{m}}_{(a,b)} \tag{8}$$

The thermodynamic process of charging and discharging a pneumatic actuator is an active area of research. There are number of publications that discuss extensively over the process of gas expansion and compression in the cylinder. It has been shown by some researchers that the charging process is dominantly isothermal (refer [25]) and many have concluded the discharging process also to be well approximated as isothermal (refer [25, 26]). Therefore, an isothermal process is a reasonable assumption to make.

Substitution of equation (8) in equation (7) yields:

$$\dot{V} = RTV_a(P_a - \hat{P}_a)(\dot{m}_a - \dot{\hat{m}}_a) + RTV_b(P_b - \hat{P}_b)(\dot{m}_b - \dot{\hat{m}}_b) \tag{9}$$

In the above equation, $\dot{V}$ is negative semi-definite. The term $(P_{(a,b)} - \hat{P}_{(a,b)})(\dot{m}_{(a,b)} - \dot{\hat{m}}_{(a,b)})$ is always non-positive for both the charging and discharging

process. During the charging process for a given known valve orifice area, if the actual pressure in the cylinder is higher than the estimated pressure, then the actual flow rate will be less than the estimated flow rate. This is because a higher downstream pressure always results in a lower mass flow rate in case of the unchoked flow. For the case of choked flow, $\dot{m}$ and $\dot{\hat{m}}$ will be equal as the flow rate is only a function of known supply pressure. In contrast, for the discharging process with a known valve orifice area, a higher actual pressure in the cylinder will result in a higher mass flow rate than the estimated mass flow rate. However, as noted earlier, both $\dot{m}$ and $\dot{\hat{m}}$ will be negative because of the sign convention of discharge, again resulting in a non-positive $(P_{(a,b)} - \hat{P}_{(a,b)})(\dot{m}_{(a,b)} - \dot{\hat{m}}_{(a,b)})$ term. This term always being non-positive acts as a natural feedback correction between the actual and observed pressures. This of course hinges on a well characterized valve with an accurate, high bandwidth command of the flow orifice area – something typically well provided by the valve manufacturer – and the accuracy of equation (3) – which has been shown in the literature to be quite accurate.

At singular points, i.e. when the velocity and control inputs are zero, the value of the scalar function $\dot{V}$ is zero. Consequently, it can be inferred that the error will not diverge away from the real values. Since $\dot{V}$ is negative semi-definite, the equilibrium point of zero is stable.

3.2 Force-Error based Observer Design

In this method, the Lyapunov function is chosen based on the error between actual and estimated pressures of the cylinder as determined through an estimate of the force

(which is estimated from the motion of the load). The pressure is estimated based on a state equation with the corrective term as follows:

$$\dot{\hat{P}}_a = \frac{\gamma RT}{V_a}\dot{\hat{m}}_a - \frac{\gamma \dot{V}_a}{V_a}\hat{P}_a + k_1 \Delta\widetilde{F} \tag{10}$$

$$\dot{\hat{P}}_b = \frac{\gamma RT}{V_b}\dot{\hat{m}}_b - \frac{\gamma \dot{V}_b}{V_b}\hat{P}_b + k_2 \Delta\widetilde{F}$$

where, $$\Delta\widetilde{F} = (P_a A_a - P_b A_b) - (\hat{P}_a A_a - \hat{P}_b A_b) \tag{11}$$

This term, $\Delta\widetilde{F}$, can be calculated using a manipulation of equation (1) ($P_a A_a - P_b A_b = M\ddot{x} + B\dot{x} + F_c - P_{atm} A_r$), and using estimates of pressures in chambers 'A' and 'B'. The above equation can be rearranged as:

$$\Delta\widetilde{F} = (P_a - \hat{P}_a)A_a - (P_b - \hat{P}_b)A_b \tag{12}$$

The convergence of the pressure estimation error can be shown by using the following candidate positive definite Lyapunov function:

$$V = \frac{1}{2}\widetilde{P}_a^2 + \frac{1}{2}\widetilde{P}_b^2 \tag{13}$$

Differentiating equation (13) results in:

$$\dot{V} = \widetilde{P}_a \dot{\widetilde{P}}_a + \widetilde{P}_b \dot{\widetilde{P}}_b \tag{14}$$

Substituting equation (10) in the equation (14) yields:

$$\dot{V} = (P_a - \hat{P}_a)[\frac{\gamma RT}{V_a}(\dot{m}_a - \dot{\hat{m}}_a) - \frac{\gamma \dot{V}_a}{V_a}(P_a - \hat{P}_a) - k_1\{(P_a - \hat{P}_a)A_a - (P_b - \hat{P}_b)A_b\}] \quad +$$

$$(P_b - \hat{P}_b)[\frac{\gamma RT}{V_b}(\dot{m}_b - \dot{\hat{m}}_b) - \frac{\gamma \dot{V}_b}{V_b}(P_b - \hat{P}_b) - k_2\{(P_a - \hat{P}_a)A_a - (P_b - \hat{P}_b)A_b\}] \tag{15}$$

Rearranging equation (15):

$$\dot{V} = \frac{\gamma RT}{V_a}(\dot{m}_a - \dot{\hat{m}}_a)(P_a - \hat{P}_a) - (\frac{\gamma \dot{V}_a}{V_a} + k_1 A_a)(P_a - \hat{P}_a)^2 + \frac{\gamma RT}{V_b}(\dot{m}_b - \dot{\hat{m}}_b)(P_b - \hat{P}_b)$$

$$- \quad (\frac{\gamma \dot{V}_b}{V_b} - k_2 A_b)(P_b - \hat{P}_b)^2 + (k_1 A_b - k_2 A_a)(P_a - \hat{P}_a)(P_b - \hat{P}_b) \quad (16)$$

selecting $(k_1 A_b - k_2 A_a) = -2(\frac{\gamma \dot{V}_a}{V_a} + k_1 A_a)^{1/2}(\frac{\gamma \dot{V}_b}{V_b} - k_2 A_b)^{1/2}$ and substituting in equation(16):

$$\dot{V} = \frac{\gamma RT}{V_a}(\dot{m}_a - \dot{\hat{m}}_a)(P_a - \hat{P}_a) + \frac{\gamma RT}{V_b}(\dot{m}_b - \dot{\hat{m}}_b)(P_b - \hat{P}_b) -$$

$$[(\frac{\gamma \dot{V}_a}{V_a} + k_1 A_a)^{1/2}(P_a - \hat{P}_a) + (\frac{\gamma \dot{V}_b}{V_b} - k_2 A_b)^{1/2}(P_b - \hat{P}_b)]^2 \quad (17)$$

It has already been shown in the previous section that first two terms in the above equation are negative semi-definite. Therefore, in order to make $\dot{V}$ negative definite, terms $(\frac{\gamma \dot{V}_a}{V_a} + k_1 A_a)$ and $(\frac{\gamma \dot{V}_b}{V_b} - k_2 A_b)$ should be positive along with the constraint:

$$(k_1 A_b - k_2 A_a)^2 = 4(\frac{\gamma \dot{V}_a}{V_a} + k_1 A_a)(\frac{\gamma \dot{V}_b}{V_b} - k_2 A_b) \quad (18)$$

The above equation is a quadratic equation and can be solved to get bounds on the value of k_1 and k_2 which will give real values of these two parameters.

For analyzing the scalar function $\dot{V}$, consider three cases:

Case I: Velocity ($\dot{x}$) positive ($\dot{V}_a$ positive and $\dot{V}_b$ negative)

It can be shown by solving the quadratic equation (equation (18)) that selection of gains as $k_1 = \frac{\gamma \dot{V}_b A_a}{V_b A_b^2}$ and $k_2 = \frac{\gamma \dot{V}_b}{V_b A_b}$ will result in negative definite $\dot{V}$ for $V_a \le V_b\left(\frac{A_b}{A_a}\right)$

When $V_a > V_b\left(\frac{A_b}{A_a}\right)$, it can be shown that selection of gains as $k_1 = \frac{-\gamma \dot{V}_a}{V_a A_a}$ and $k_2 = -\frac{\gamma \dot{V}_a A_b}{V_a A_a^2}$ will result in a negative definite $\dot{V}$ for sufficiently high velocities.

Case II: Velocity ($\dot{x}$) negative ($\dot{V}_a$ negative and $\dot{V}_b$ positive)

The solution of the quadratic equation shows that selection of gains as $k_1 = \frac{-\gamma \dot{V}_a}{V_a A_a}$ and $k_2 = -\frac{\gamma \dot{V}_a A_b}{V_a A_a^2}$ will result in a negative definite $\dot{V}$ for $V_a > V_b\left(\frac{A_b}{A_a}\right)$. When $V_a \le V_b\left(\frac{A_b}{A_a}\right)$, it can be shown that selection of gains as $k_1 = \frac{\gamma \dot{V}_b A_a}{V_b A_b^2}$ and $k_2 = \frac{\gamma \dot{V}_b}{V_b A_b}$ will result in a negative definite $\dot{V}$ for sufficiently high velocities.

Case III: Velocity ($\dot{x}$) and control inputs zero (Singular points)

Setting gains k_1 and k_2 equal to zero will result in $\dot{V}$ equal to zero (negative semi-definite). This case is similar to the singularity condition of the energy-based Lyapunov observer.

From a consideration of all three cases, at worst $\dot{V}$ is negative semi-definite, and the equilibrium point of zero is stable.

4. Sliding Mode Controller

The proposed motion controller in this paper is based on sliding mode control theory. Sliding mode controllers are generally well suited for pneumatic servo actuators

due to the highly non-linear behavior and uncertainties present in the model. The equivalent control input is calculated such that the rate of change of a positive-definite ($V = \frac{1}{2}s(t)^2$) Lyapunov scalar function is zero ($\dot{V} = 0$), where the manifold *s = 0* is defined as the desired stable motion tracking error dynamics. A corrective term is then added to the equivalent control input to make $\dot{V}$ negative in the face of uncertainty, which implies robustness of the controller and provides uniform asymptotic stability. With this condition satisfied, all trajectories will move towards the surface *s(t) = 0,* and once they reach the surface, remain on it for all future time.

For the system shown in Figure 3-2, the desired output is the position of the end-effector. The control input to the system is the area of the valve. In order to derive the control law, define a time-varying sliding surface as:

$$s = \left(\frac{d}{dt} + \lambda \right)^{n-1} e \tag{19}$$

where, λ is a strictly positive number, *n* is the number of times the output must be differentiated to get the input, and *e* is the error between the actual and desired position.

The above equation can be rewritten as:

$$s = (\ddot{x} - \ddot{x}_d) + 2\lambda\dot{e} + \lambda^2 e \tag{20}$$

Substituting the expression of $\ddot{x}$ from equation (1) in the equation (20), and neglecting friction:

$$s = \frac{1}{M}(P_a A_a - P_b A_b - P_{atm} A_r - B\dot{x}) - \ddot{x}_d + 2\lambda\dot{e} + \lambda^2 e \tag{21}$$

Differentiating equation (21) results in:

$$\dot{s} = \frac{1}{M}(\dot{P}_a A_a - \dot{P}_b A_b - B\ddot{x}) - x_d^{(3)} + 2\lambda\ddot{e} + \lambda^2\dot{e} \tag{22}$$

In the control of the pneumatic system shown in Figure 3-2, two four-way proportional spool valves were used. However, they were constrained to act as a one four-way proportional spool valve. Accordingly, the following constraint equation was imposed on the control input, which is the effective or signed valve area in this case:

$$A_v = A_{v_a} = -A_{v_b} \tag{23}$$

A positive valve area corresponds to the charging of chamber 'A' and discharging of the chamber 'B', while a negative area corresponds to charging of the chamber 'B' and discharging of the chamber 'A'.

Using constraint equation (23), substituting the value of $\dot{P}_a$ and $\dot{P}_b$ in equation (22) and equating $\dot{s}$ to zero yields the equivalent control law:

$$A_{v_{eq}} = \frac{\gamma\dot{x}\left(\frac{P_a A_a^2}{V_a} + \frac{P_b A_b^2}{V_b}\right) + B\ddot{x} + M(x_d^{(3)} - 2\lambda\ddot{e} - \lambda^2\dot{e})}{RT\gamma\left(\frac{C_f}{\sqrt{T}}\right)\left(\frac{P_{u_a}\psi(P_{u_a}, P_{d_a})A_a}{V_a} + \frac{P_{u_b}\psi(P_{u_b}, P_{d_b})A_b}{V_b}\right)} \tag{24}$$

where, $\psi = \begin{cases} P_u\sqrt{\frac{\gamma}{R}\left(\frac{2}{\gamma+1}\right)^{\frac{(\gamma+1)}{(\gamma-1)}}} & \textit{for choked flow} \\ P_u\left(\frac{P_d}{P_u}\right)^{\frac{1}{\gamma}}\left(\sqrt{1-\left(\frac{P_d}{P_u}\right)^{\frac{(\gamma-1)}{\gamma}}}\right)\left(\sqrt{\frac{2\gamma}{R(\gamma-1)}}\right) & \textit{for unchoked flow} \end{cases}$

The function ψ captures the shift in dynamic behavior that occurs in the transition between choked and unchoked flow through the valve. The switching condition in equation (24) ensures that the controller uses the right equivalent control law. This equivalent control input provides marginal stability in the sense of Lyapunov and uses

model and error information. As noted earlier, a robustness term is added to this control input to ensure uniform asymptotic stability. Thus the final control input is given by:

$$A_v = A_{veq} - k * sat\left(\frac{s}{\phi}\right) \tag{25}$$

where k is a strictly positive gain and captures bounded uncertainties of the model and the pressure observer; Φ is the boundary layer thickness and selected such as to avoid excessive chattering across the sliding surface while maintaining the desired performance of the system.

The saturation function in equation (25) is defined by the following:

$$sat(\frac{s}{\phi}) = \begin{cases} \text{sgn}\left(\frac{s}{\phi}\right) & if \left|\frac{s}{\phi}\right| \geq 1 \\ \frac{s}{\phi} & otherwise \end{cases} \tag{26}$$

5. Experimental Setup

The sliding mode controller, along with the developed observers, was implemented for the servo control of a commercial two-degree of freedom pneumatic robot (manufactured by Festo Corporation). A schematic of the system setup is illustrated in Figure 3-1 and the actual setup is shown in Figure 3-2. For the results, only one degree of freedom is used, which is a double acting pneumatic cylinder (Festo SLT-20-150-A-CC-B). Two four-way proportional spool valves (Festo MPYE-5-M5-010-B) constrained to operate together are used for controlling charging and discharging process of both chambers of the cylinder. A linear potentiometer (Midori LP-150F) with a travel length of 150 mm is used to measure the position of the load. The velocity signals are obtained by an analog differentiator with a first order roll-off at 50 Hertz. Similarly, acceleration

signals are obtained by an analog differentiation of the velocity signals with a first order roll-off at 50 Hertz. Two pressure transducers (Festo SDE-16-10V/20mA) are also used in the setup for the measurement of actual pressures. The control and the observer algorithms are implemented using Real Time Workshop (RTW) from Mathworks on a 2.4GHz, 512MB RAM, Pentium IV processor based PC. The communication between the computer and the experimental setup is established through the digital input and analog output channels of an A/D card (National Instruments PCI-6031E).

The maximum pressure supply used for this experiment is 620kPa (90 psig). Some of the parameters (example, area of piston, area of rod, stroke length, pay-load mass) for this experiment are known accurately. The discharge coefficient (C_e), which primarily represents frictional flow losses, is a function of the valve area among other parameters such as the size and shape of the valve opening, surface finish and similar parameters. For this experiment, the average discharge coefficient was calculated based on the volumetric flow chart provided by the valve manufacturer. Other parameters, like the viscous friction coefficient, are difficult to measure. Therefore, these parameters are estimated.

The experiment was conducted in two stages. In the first stage of the experiment, pressure sensors signals were used in the control law to control the end-effector with a mass of 3.6 kilograms. For this, the robotic arm was controlled to execute a sinusoidal motion at different frequencies. The same experiment was then repeated for step inputs. In another set of readings, disturbances were introduced in the system by applying external forces (using our hand) to the robotic arm to ensure the robustness of the observer in presence of disturbances and uncertainties (such as friction) in the system. In

all the cases, the actual pressures in both the chambers were recorded and compared with the corresponding observed pressures.

In the second stage of the experiment, to prove the effectiveness of the observers, the pressure sensors were disconnected from the system. The robotic arm was then controlled using the estimated pressures from the pressure observers. The end-effector was commanded for the same sinusoidal and step input as used for the first stage of the experiment. Subsequently, the tracking performance of the robotic arm was compared to the tracking obtained using pressure sensors.

6. Results and Discussion

Figure 3-3 shows a comparison of observed and actual pressures at a 0.5 Hz sinusoidal motion of amplitude 30 mm. In figure 3-3a, the solid line shows the actual pressure as measured with a pressure sensor in chamber 'A'. The dotted line shows the observed pressure with the energy-based Lyapunov observer. Similarly, figure 3-3b shows the observed and actual pressures from the force-error based observer in chamber 'A'. Figure 3-3c and 3-3d shows the measured and observed pressures in chamber 'B'.

Figure 3-4 and Figure 3-5 shows the convergence of the observed pressure at 2 Hz and 3 Hz frequencies respectively. The initial conditions of the observed pressures in this case were set different from the actual initial values to check the convergence rate. As can be seen in Figure 3-4a, the initial pressure of the observer for chamber 'A' was set to atmosphere pressure (101 *kPa*) when the actual pressure in the chamber was 475 *kPa*. The observed value converges in nearly 0.3 seconds. For chamber 'B', the observed

pressure converges in 0.2 seconds (figure 3-4b). Similarly, figure 3-6 shows the observer results for a step motion.

As shown in the figures, the observed pressures quickly converge toward the actual pressures. A maximum multiplicative error of +0.4 and -0.9 atmospheric pressure was observed for energy-based observers when the velocity of the piston is zero. Similarly, a maximum multiplicative error of ± 0.6 atmospheric pressure exists for force-error based observers. More significantly for purposes of control, the phase delay of either observer method was similar or smaller than the actual pressure sensor signal. The prime cause of the error between the observed and measured pressure signal is the difference between the actual and calculated mass flow rates. The error between the flow rates is higher at small area openings of the valve. As noted earlier, the mass flow rate calculations are based on the average discharge coefficient which is a function of valve opening area among other parameters. At small valve openings, frictional flow losses are more dominant and hence the value of the discharge coefficient is much lower than the average value used in the experiment. This effect is dominant at lower frequencies when the valve openings are small. Another contributing factor in the error is the frictional flow losses in the pipes between the valve and the cylinder, which is neglected in the design of the observers. The length of the air tubes used in the experiment were kept fairly short to minimize this unmodeled effect.

The results of the case when external disturbances are added to the system are shown in Figure 3-7. The disturbances were introduced in the system by applying external forces (by hand) to the robotic arm. The force was added between 1.2 to 2.8 seconds and between 5.2 to 6.5 seconds. In this case also, the observed response closely

follows the actual response of the system. This shows the robustness of the observer in presence of disturbances and uncertainties (such as friction) in the system.

Convergence using force-error based observer shows a dependence on the correct estimate of friction. In this experiment, a constant value of viscous friction coefficient and Coulomb forces is used which gives satisfactory results. However, an adaptive algorithm could be implemented to adapt these parameters to improve on the results. The friction of the proportional valve is not modeled in the observer design. Instead, a dither signal of 100 Hz frequency of small amplitude is used in the experiment to nullify the effect of static friction. A part of the error is also contributed by velocity and acceleration signals since these are obtained by differentiating the position and velocity signals respectively. As a consequence, these are noisy and hence add to the deviation of the observed pressures from the actual values.

The design of the energy-based observer is independent of the frictional forces between the payload and the surface – or indeed independent of any model of the load dynamics. Furthermore, the convergence rate is unaffected if the payload varies, as might be the case with an industrial robotic manipulator. The only disadvantage associated with this observer is that the convergence rate cannot be influenced. It is however observed experimentally that convergence is faster at higher tracking frequencies.

The motion tracking results of the controller with a mass of 3.6 kg at the end-effector are demonstrated in Figures 3-8 and 3-9. In all the figures shown, the solid line shows the desired trajectory and the dashed line shows the actual trajectory followed by the end-effector. Figure 3-8a shows the tracking of the end-effector at a 0.25 Hz sinusoidal frequency when the controller uses pressure sensors present in the system.

Figure 3-8b shows the result of sinusoidal tracking when the controller uses the energy-based pressure observers developed in this paper. It can be seen that the results obtained using pressure sensors versus pressure observers demonstrates essentially the same tracking performance. A small deviation in the tracking is observed in both cases when the velocity of the end-effector is zero. This is presumably because of the neglected Coulomb friction in the controller design. Figure 3-9 demonstrates the results at a 2.5 Hz sinusoidal frequency. At this frequency a phase lag and attenuation in the amplitude is observed in the response. The results of the step response are shown in Figure 3-10. The results are similar to the sinusoidal tracking where the response of the system is almost identical using pressure sensors (figure 3-10a) or using pressure observers (figure 3-10b).

The observer/controller results presented here are obtained using the energy-based pressure observer. Results of the force-error based pressure observer are very similar and are not presented in this paper. The energy-based pressure observer is preferred here due to its structural simplicity, its independence on the change of load parameters (like payload mass), and its independence of acceleration. As commented earlier, the convergence rate of the observer error cannot be explicitly influenced in the energy-based pressure observer design. However, from the experimental tracking results, it appears that the convergence rate is adequate enough to provide motion control that appears indistinguishable from the motion control that utilizes pressure sensors.

Figure 3-11 shows the measured closed-loop frequency response of the controlled system using the energy-based pressure observers. The bandwidth is observed to be about 5 Hz. It should be noted that the 5 Hz bandwidth is not a limitation of the controller. At this frequency, saturation in the valve output was observed which limited the bandwidth.

The bandwidth can be increased with the use of valves with higher mass flow rates (larger maximum orifice sizes) or by reducing the mass at the end-effector. An increase in bandwidth can also be obtained by increasing the supply pressure.

7. Conclusion

In this paper, the designs of two Lyapunov based pressure observers for a pneumatic servo system were presented. The effectiveness of the proposed pressure observers was demonstrated using experimental results. It is shown in the paper that the proposed observers, along with a robust controller, can be implemented in lieu of expensive pressure sensors. The results presented demonstrate that the tracking performance using pressure observers versus using pressure sensors is in essence indistinguishable. This shows that the system can be accurately controlled using pressure observers resulting in a lower cost system, with no performance tradeoffs. Additionally, the use of pressure observers along with the controller developed results in a lower weight, more compact, and lower maintenance system.

References

[1] Ning, S. and Bone, G. M., "High Steady-State Accuracy Pneumatic Servo Positioning System with PVA/ PV Control and Friction Compensation," *Proceeding of the 2002 IEEE International Conference on Robotics & Automation*, pp. 2824-2829, 2002.

[2] Pandian, S. R., Takemura, F., Hayakawa, Y., and Kawamura, S., "Pressure Observer-Controller Design for Pneumatic Cylinder Actuators", *IEEE/ ASME Transactions on Mechatronics*, Vol 7, no. 4, pp. 490-499.

[3] Acarman, T., Hatipoglu, C., and Ozguner, U., "A Robust Nonlinear Controller Design for a Pneumatic Actuator", *Proceedings of the American Control Conference*, vol. 6, pp. 4490-4495, 2001.

[4] McDonell, B. W., and Bobrow, J. E., "Adaptive Tracking Control of an Air Powered Robot Actuator", ASME Journal of Dynamic Systems, Measurement, and Control, vol.115, pp. 427-433, 1993.

[5] Liu, S., and Bobrow, J. E., "An Analysis of a Pneumatic Servo System and its Application to a Computer-Controlled Robot", ASME Journal of Dynamic Systems, Measurement, and Control, vol.110, no.3, pp. 228-235, 1988.

[6] Pandian, S. R., Hayakawa, Y., Kanazawa, Y., Kamoyama, Y., and Kawamura, S., "Practical Design of a Sliding Mode Controller for Pneumatic Actuators", ASME Journal of Dynamic Systems, Measurement, and Control, vol. 119, no. 4, pp. 664-674, 1997.

[7] Arun, P. K., Mishra, J. K., and Radke, M. G., "Reduced Order Sliding Mode Control for Pneumatic Actuator", *IEEE Transactions on Control Systems Technology*, v 2, n 3, p 271-276, 1994.

[8] Tang, J., and Walker, G., "Variable Structure Control of a Pneumatic Actuator", *Journal of Dynamic Systems, Measurement and Control, Transactions of the ASME*, v 117, n 1, pp. 88-92, 1995.

[9] Richer, E., Hurmuzlu, Y., "A High Performance Pneumatic Force Actuator System: Part II – Nonlinear controller Design", *ASME Journal of Dynamic Systems, Measurement, and Control*, vol.122, no.3, pp.426-434, 2000.

[10] Sanville, F. E., "Two-level Compressed Air Systems for Energy Saving", *The 7th International Fluid Control Symposium*, pp. 375-383, 1986.

[11] Al-Dakkan, K. A., "Energy Saving Control for Pneumatic Servo Systems", Ph.D. Thesis, Vanderbilt University, Nashville, TN, 2003.

[12] Ye, N., Scavarda, S., Betemps, M., and Jutard, A., "Models of a Pneumatic PWM Solenoid Valve for Engineering Applications", *ASME Journal of Dynamic Systems, Measurement, and Control*, vol.114, no.4, pp. 680-688, 1992.

[13] Kunt, C., and Singh, R., "A Linear Time Varying Model for On-Off Valve Controlled Pneumatic Actuators", *ASME Journal of Dynamic Systems, Measurement, and Control*, vol.112, no.4, pp. 740-747, 1990.

[14] Lai, J. Y., Singh, R., and Menq, C. H., "Development of PWM Mode Position Control for a Pneumatic Servo System", *Journal of the Chinese Society of Mechanical Engineers*, vol.13, no.1, pp. 86-95, 1992.

[15] Royston, T., and Singh, R., "Development of a Pulse-Width Modulated Pneumatic Rotary Valve for Actuator Position Control", *ASME Journal of Dynamic Systems, Measurement, and Control*, vol.115, no.3, pp. 495-505, 1993.

[16] Paul, A. K., Mishra, J. K., and Radke, M. G., "Reduced Order Sliding Mode Control for Pneumatic Actuator", *IEEE Transactions on Control Systems Technology*, vol.2, no.3, pp. 271-276, 1994.

[17] Shih, M., and Hwang, C., "Fuzzy PWM Control of the Positions of a Pneumatic Robot Cylinder Using High Speed Solenoid Valve", *JSME International Journal*, vol.40, no.3, pp.469-476, 1997.

[18] Bigras, P. and Khayati, K., "Nonlinear Observer for Pneumatic System with Non Negligible Connection Port Restriction", *Proceedings of the American Control Conference*, Anchorage, AK, pp. 3191-3195, 2002.

[19] Wu, J., Goldfarb, M., and Barth, E., "On the Observability of Pressure in a Pneumatic Servo Actuator", *ASME Journal of Dynamic Systems, Measurement, and Control*, in press.

[20] Ogata, K., "*System Dynamics*", Prentice-Hall, Inc., Eaglewood Cliff, New Jersey, 1978.

[21] Shearer, J. L., "Study of Pneumatic Processes in the Continuous Control of Motion with Compressed Air – I", *Transactions of the ASME*, vol. 78, pp. 233-242, 1956.

[22] Shearer J. L., ""Study of Pneumatic Processes in the Continuous Control of Motion with Compressed Air – II", *Transactions of the ASME*, vol. 78, pp. 243-249, 1956.

[23] Bobrow, J., and McDonell, B., "Modeling, Identification, and Control of a Pneumatically Actuated, Force Controllable Robot," *IEEE Transactions on Robotics and Automation*, vol. 14, no. 5, pp. 732-742, 1998.

[24] Richer, E., Hurmuzlu, Y., "A High Performance Pneumatic Force Actuator System: Part I – Nonlinear Mathematical Model", *ASME Journal of Dynamic Systems, Measurement, and Control*, Vol. 122, no. 3, pp. 426-434, 2000.

[25] Skinner, C. K., and Wagner, F. D., "A Study of the Process of Charging and Discharging Constant Volume Tanks with Air", S. B. Thesis, M.I.T, Department of Mech. Engr, Cambridge, MA, 1954.

[26] Al-Ibrahim, A. M., and Otis, D. R., "Transient Air Temperature and Pressure Measurements During the Charging and Discharging Processes of an Actuating Pneumatic Cylinder", *Proceedings of the 45th National Conference on Fluid Power*, 1992.

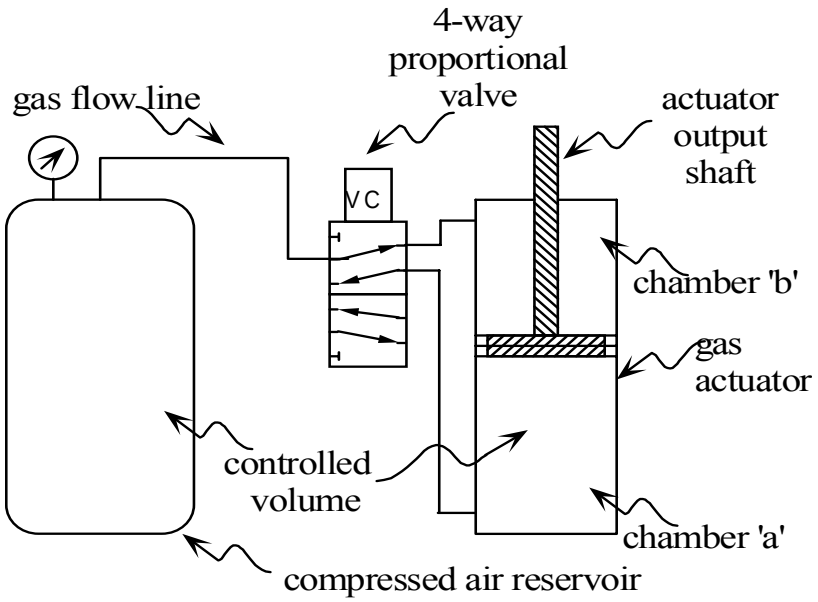

Fig 3-1. Schematic of a pneumatic servo actuation system

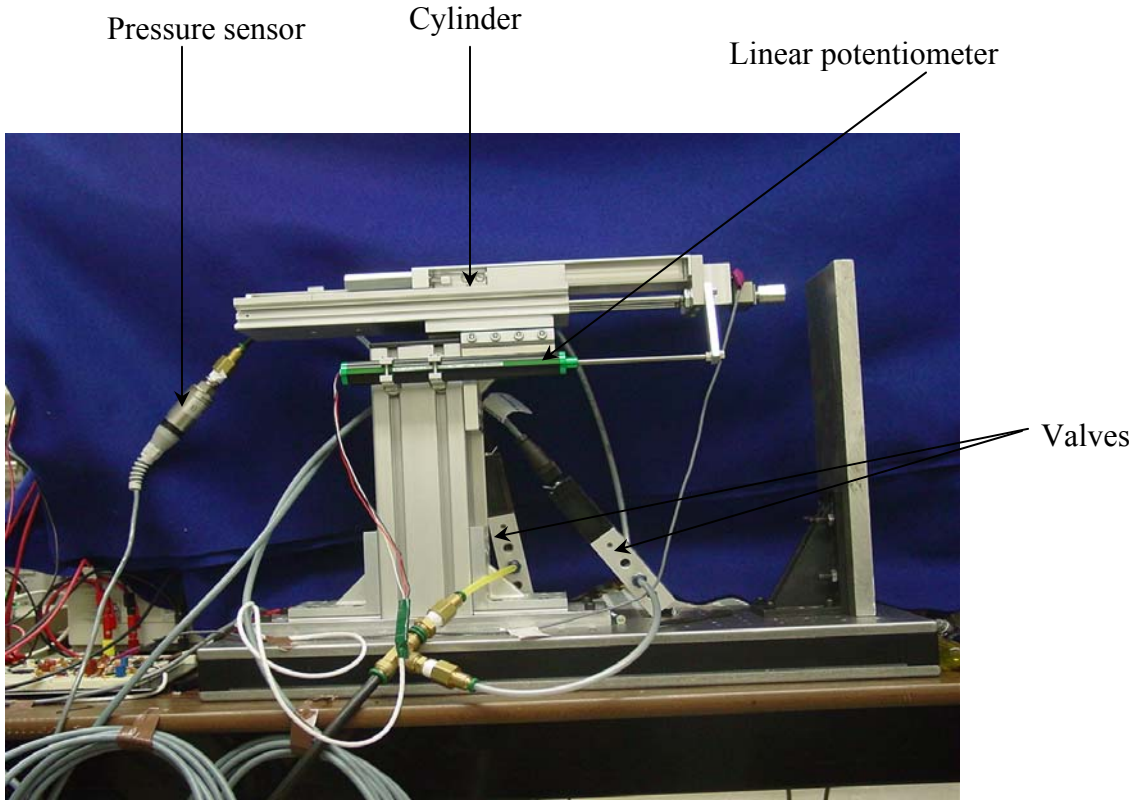

Fig 3-2. Experimental setup of a pneumatic actuator servo system

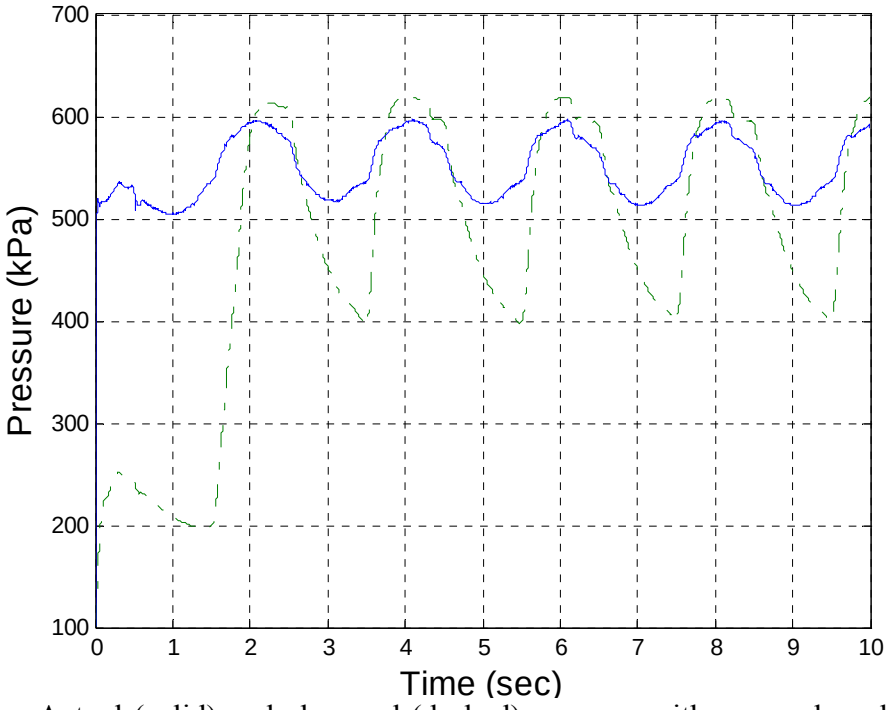

Fig. 3-3a. Actual (solid) and observed (dashed) pressure with energy-based observer at 0.5 Hz sinusoidal tracking– chamber 'A'

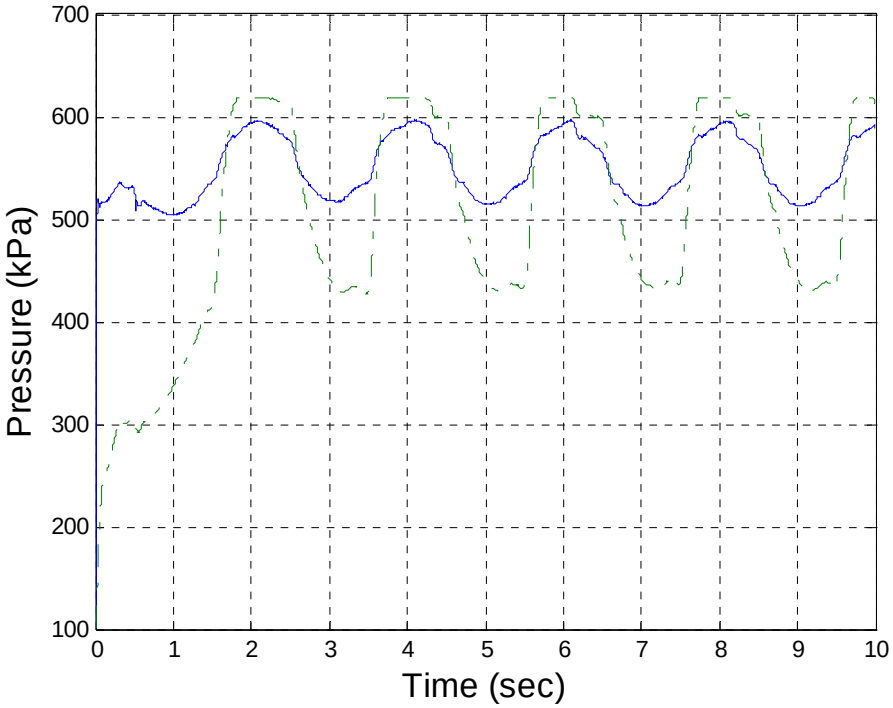

Fig. 3-3b. Actual (solid) and observed (dashed) pressure with force-error based observer at 0.5 Hz sinusoidal tracking – chamber 'A'

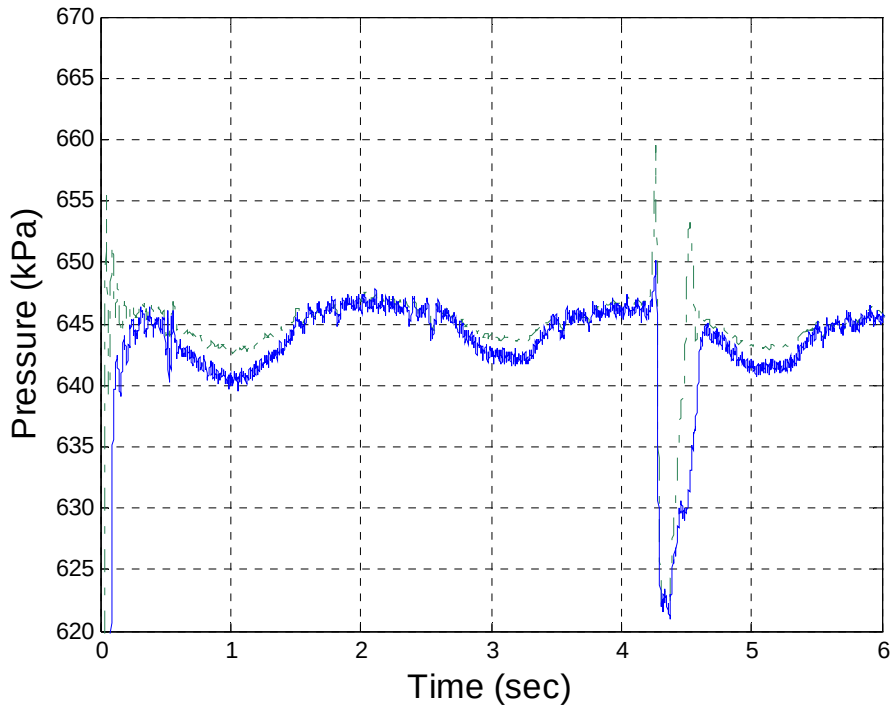

Fig. 3-3c. Actual (solid) and observed (dashed) pressure with energy-based observer at 0.5 Hz sinusoidal tracking– chamber 'B'

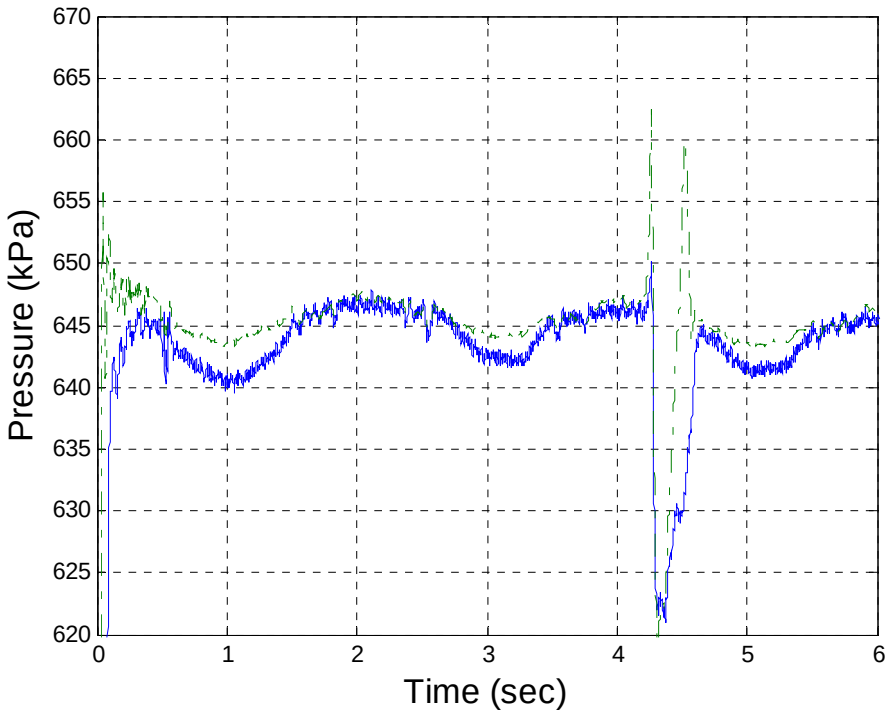

Fig. 3-3d. Actual (solid) and observed (dashed) pressure with force-error based observer at 0.5 Hz sinusoidal tracking – chamber 'B'

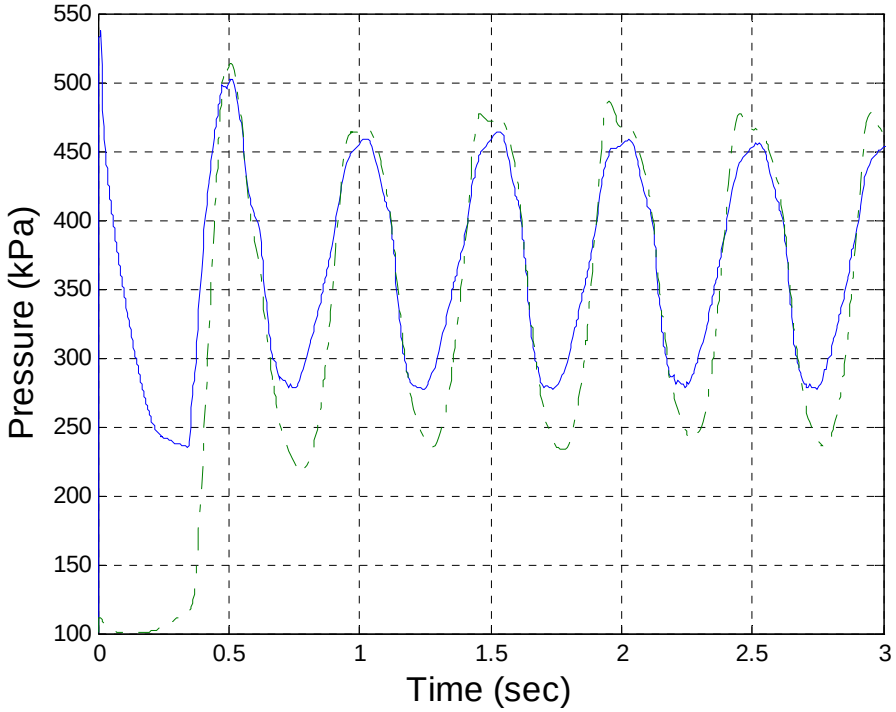

Fig. 3-4a. Actual (solid) and observed (dashed) pressure with energy-based observer at 2 Hz sinusoidal tracking– chamber 'A'

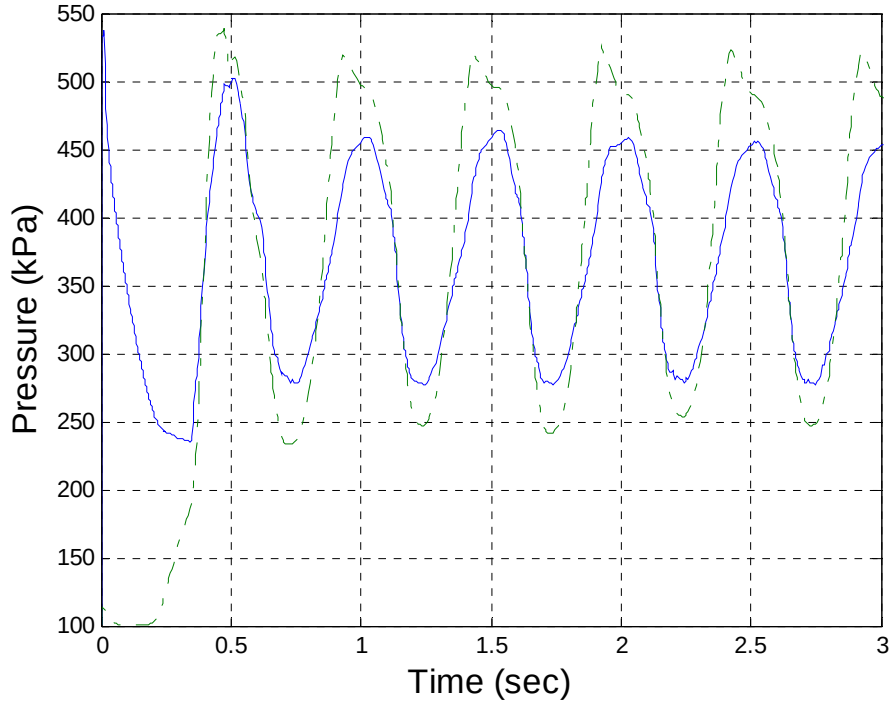

Fig. 3-4b. Actual (solid) and observed (dashed) pressure with force-error based observer at 2 Hz sinusoidal tracking – chamber 'A'

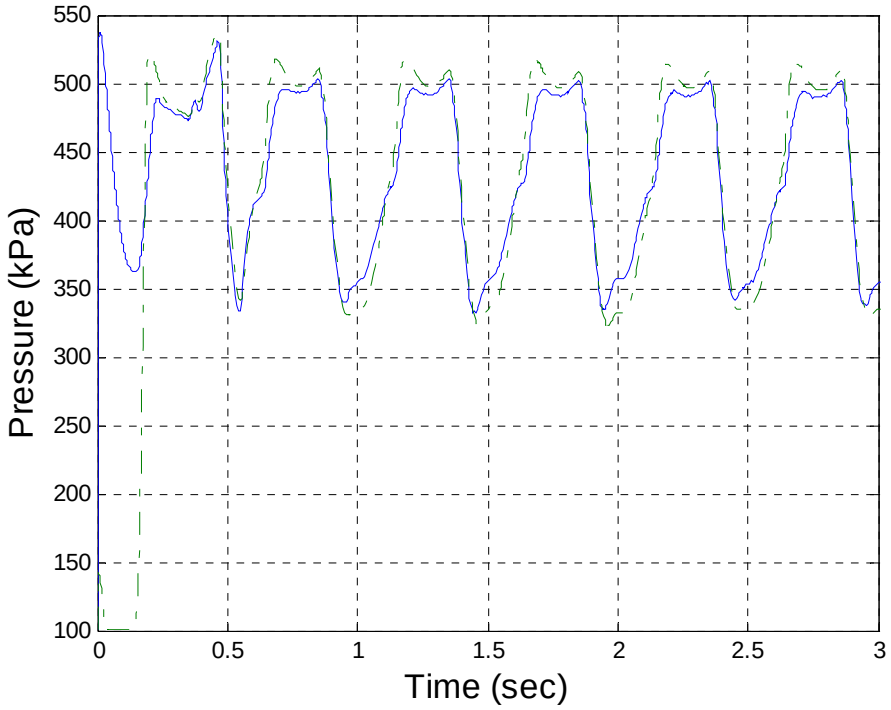

Fig. 3-4c. Actual (solid) and observed (dashed) pressure with energy-based observer at 2 Hz sinusoidal tracking– chamber 'B'

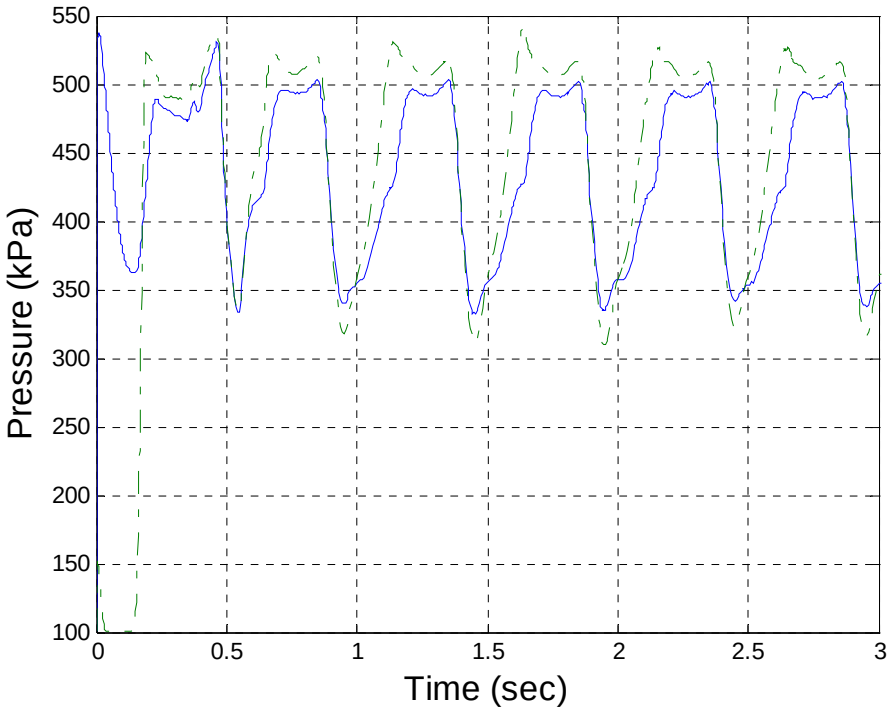

Fig. 3-4d. Actual (solid) and observed (dashed) pressure with force-error based observer at 2 Hz sinusoidal tracking – chamber 'B'

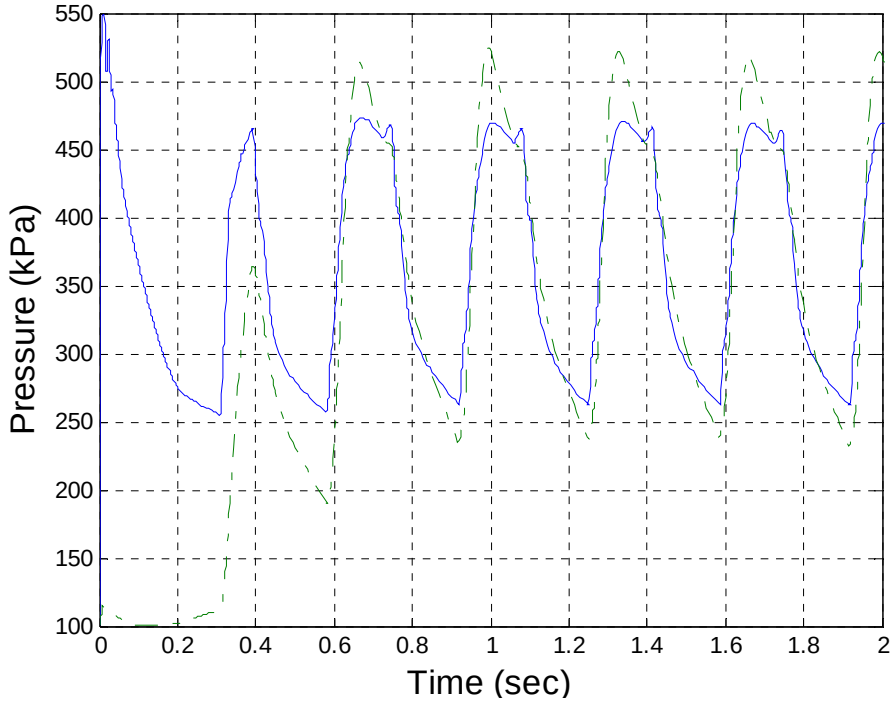

Fig. 3-5a. Actual (solid) and observed (dashed) pressure with energy-based observer at 3 Hz sinusoidal tracking– chamber 'A'

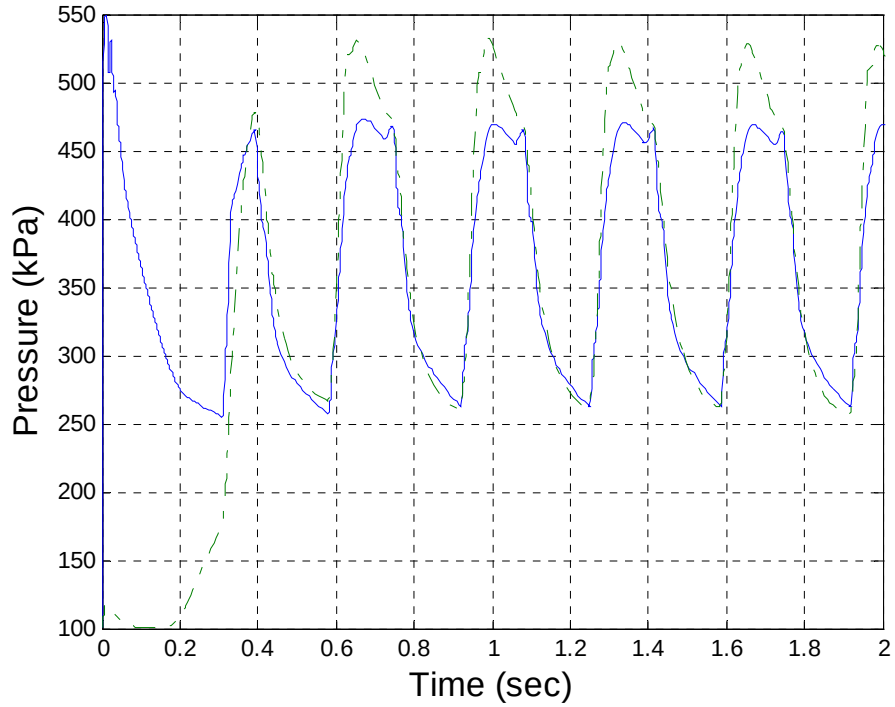

Fig. 3-5b. Actual (solid) and observed (dashed) pressure with force-error based observer at 3 Hz sinusoidal tracking – chamber 'A'

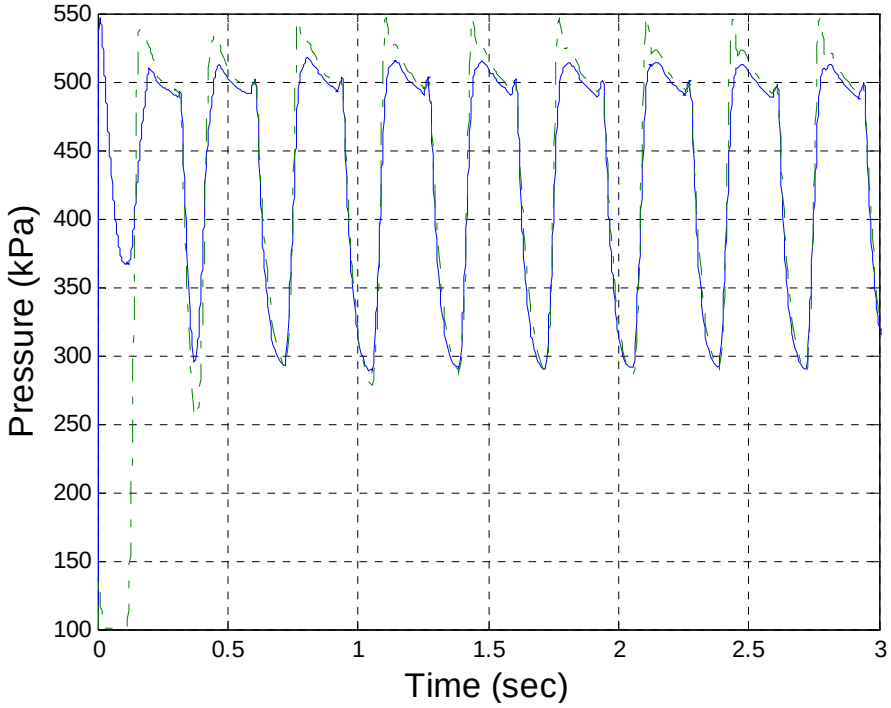

Fig. 3-5c. Actual (solid) and observed (dashed) pressure with energy-based observer at 3 Hz sinusoidal tracking– chamber 'B'

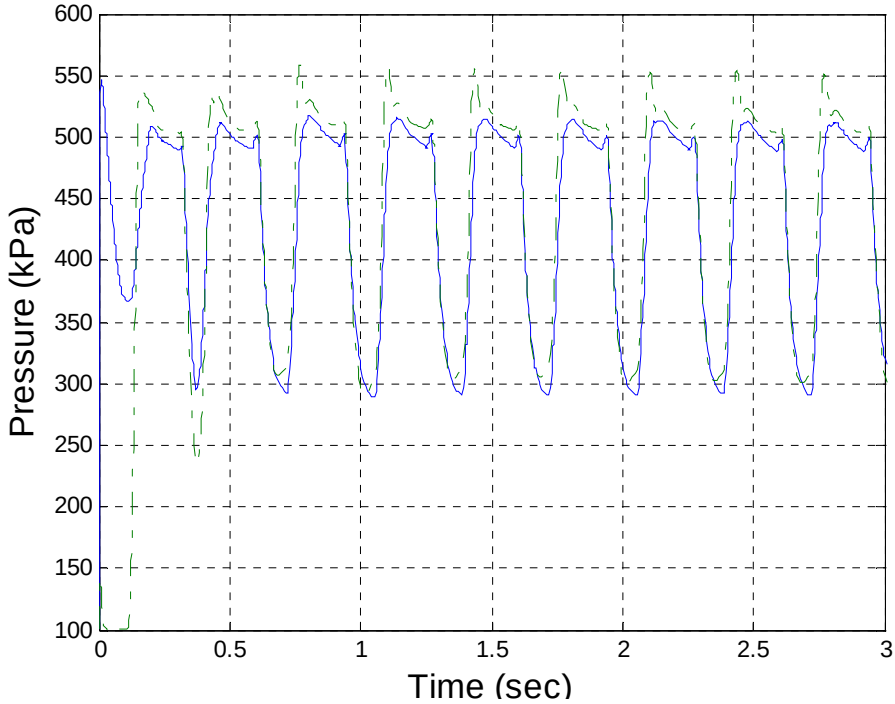

Fig. 3-5d. Actual (solid) and observed (dashed) pressure with force-error based observer at 3 Hz sinusoidal tracking – chamber 'B'

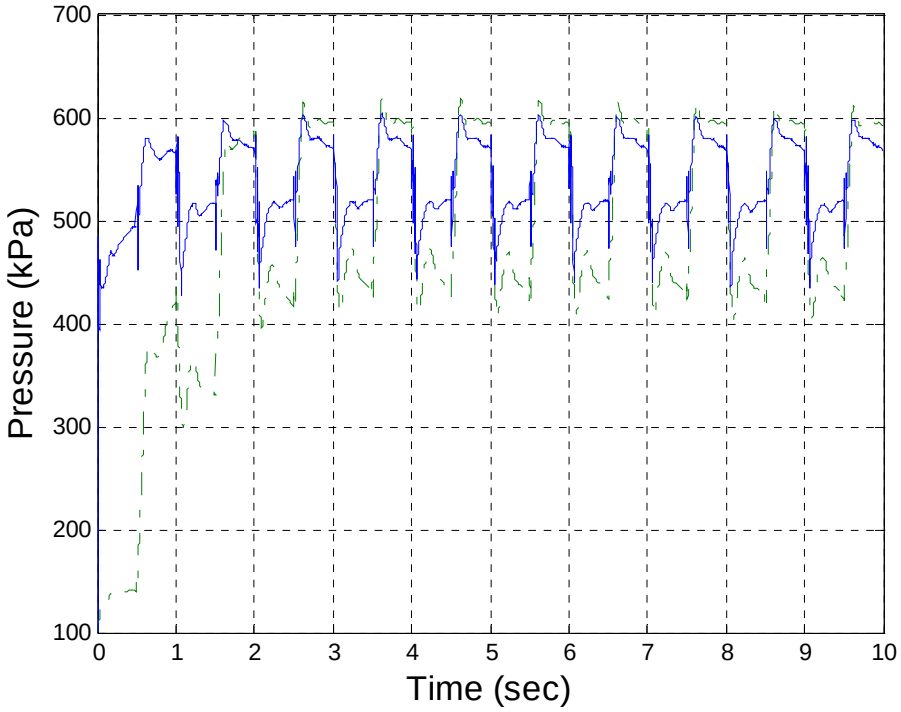

Fig. 3-6a. Actual (solid) and observed (dashed) pressure with energy-based observer at 1 Hz square wave tracking – chamber 'A'

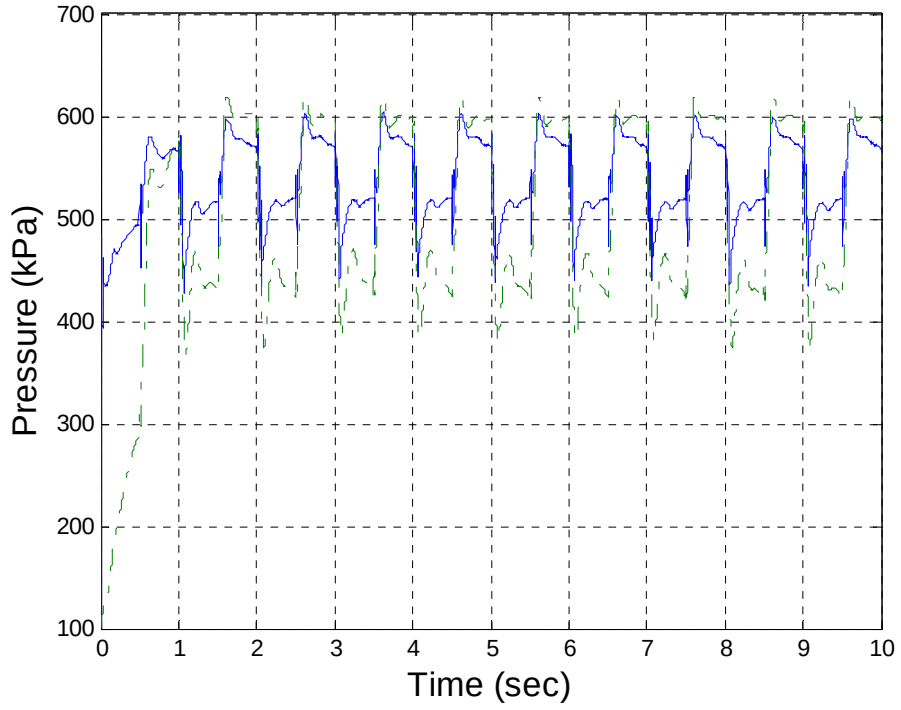

Fig. 3-6b. Actual (solid) and observed (dashed) pressure with force-error based observer at 1 Hz square wave tracking – chamber 'A'

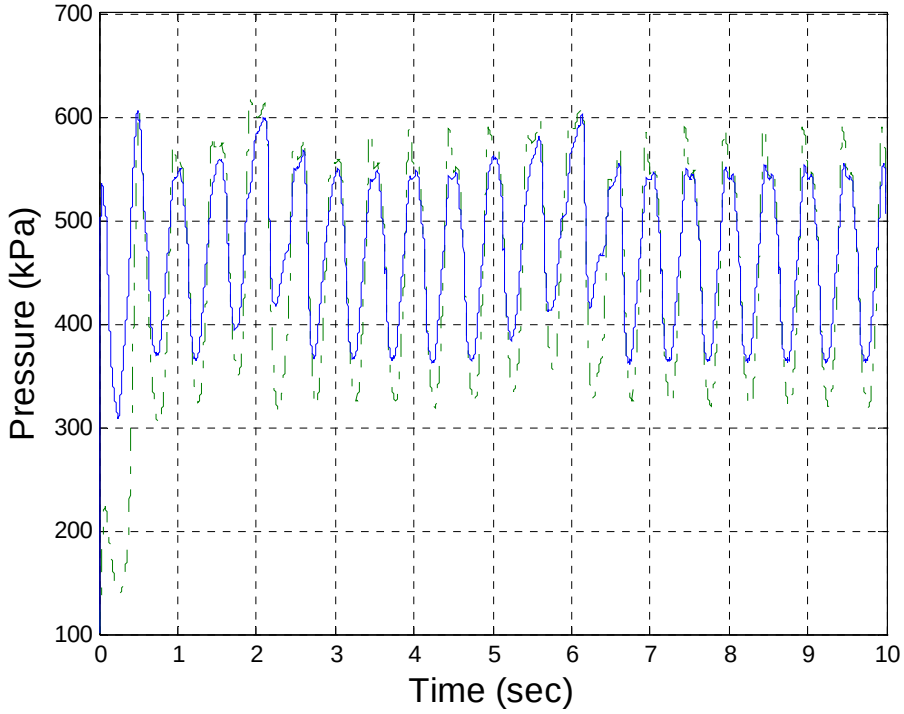

Fig. 3-7a. Actual (solid) and observed (dashed) pressure with energy-based observer at 2 Hz sinusoidal wave tracking with disturbance– chamber 'A'

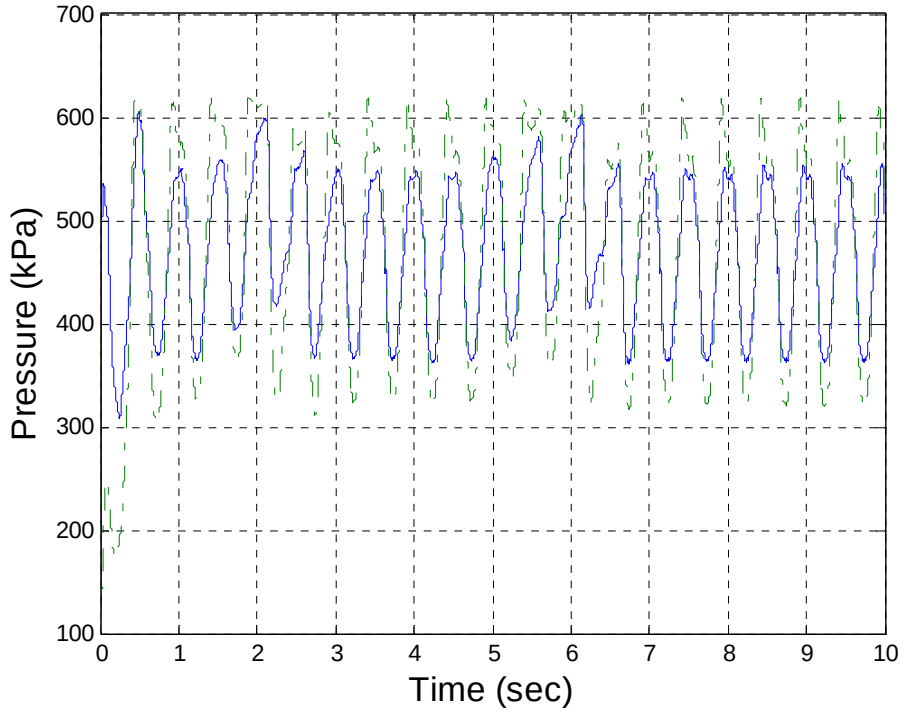

Fig. 3-7b. Actual (solid) and observed (dashed) pressure with force-error based observer at 2 Hz sinusoidal wave tracking with disturbance – chamber 'A'

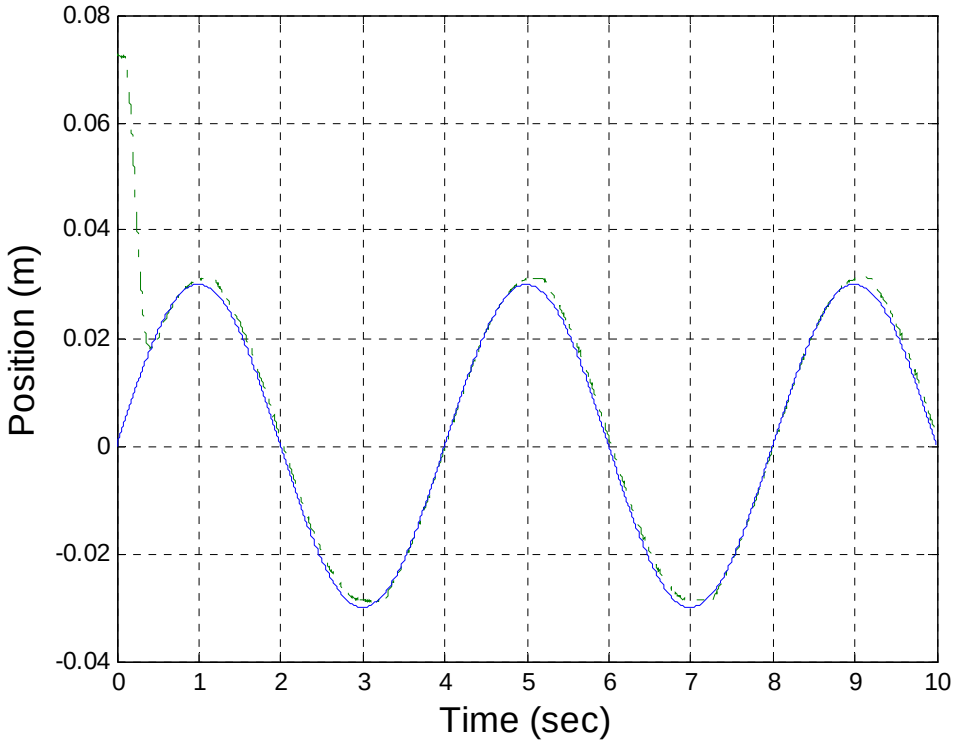

Fig. 3-8a. Desired (solid) and actual (dashed) position at 0.25 Hz sinusoidal frequency tracking using pressure sensors

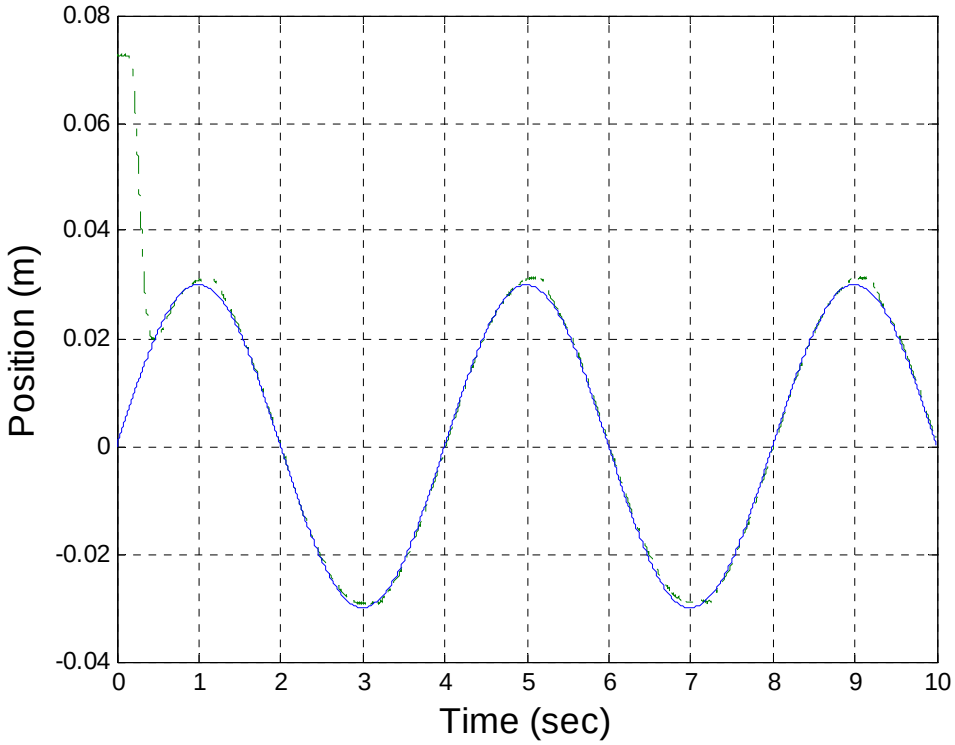

Fig. 3-8b. Desired (solid) and actual (dashed) position at 0.25 Hz sinusoidal frequency tracking using pressure observers

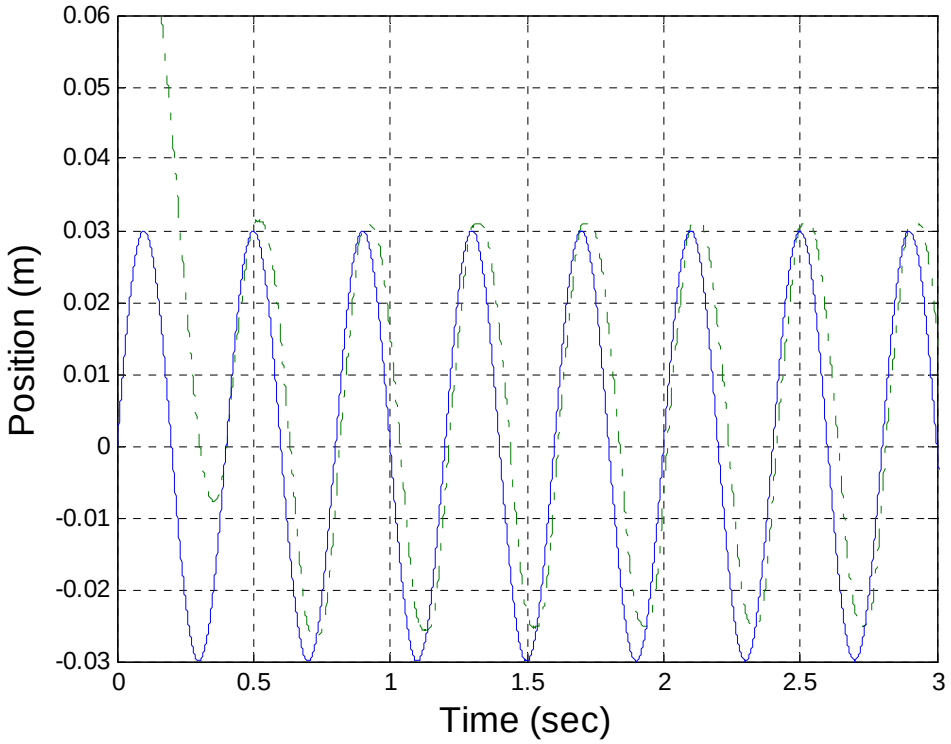

Fig. 3-9a. Desired (solid) and actual (dashed) position at 2.5 Hz sinusoidal frequency tracking using pressure sensors

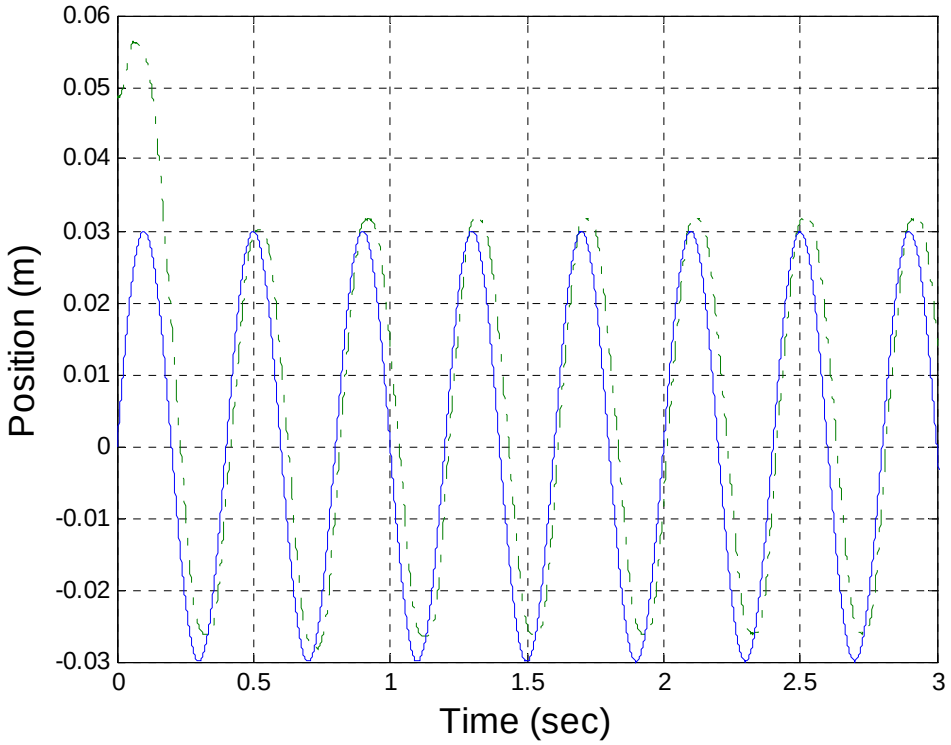

Fig. 3-9b. Desired (solid) and actual (dashed) position at 2.5 Hz sinusoidal frequency tracking using pressure observers

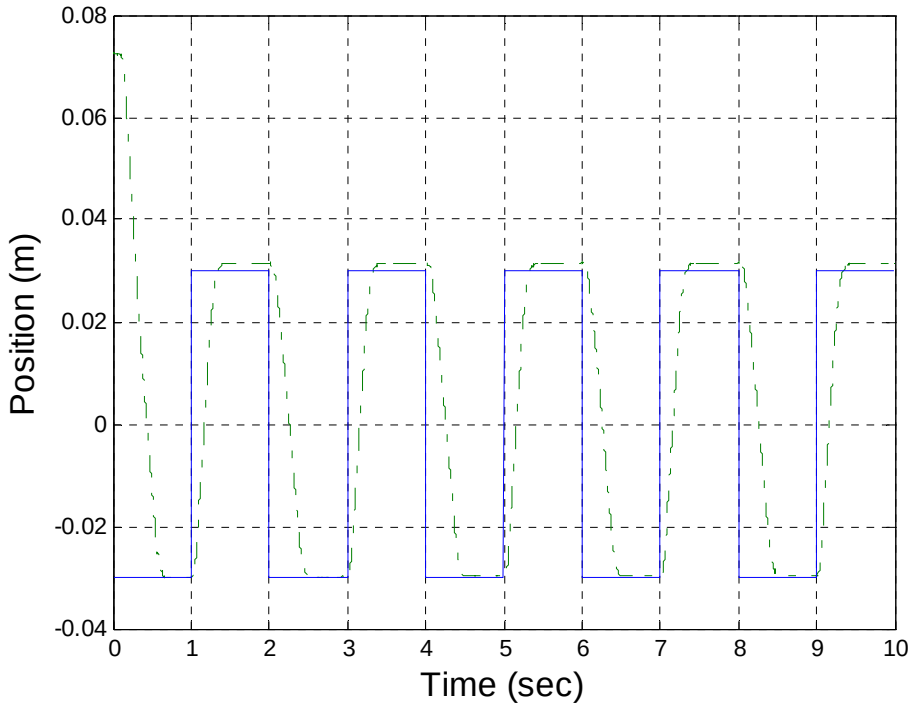

Fig. 3-10a. Desired (solid) and actual (dashed) position at 0.5 Hz square-wave frequency tracking using pressure sensors

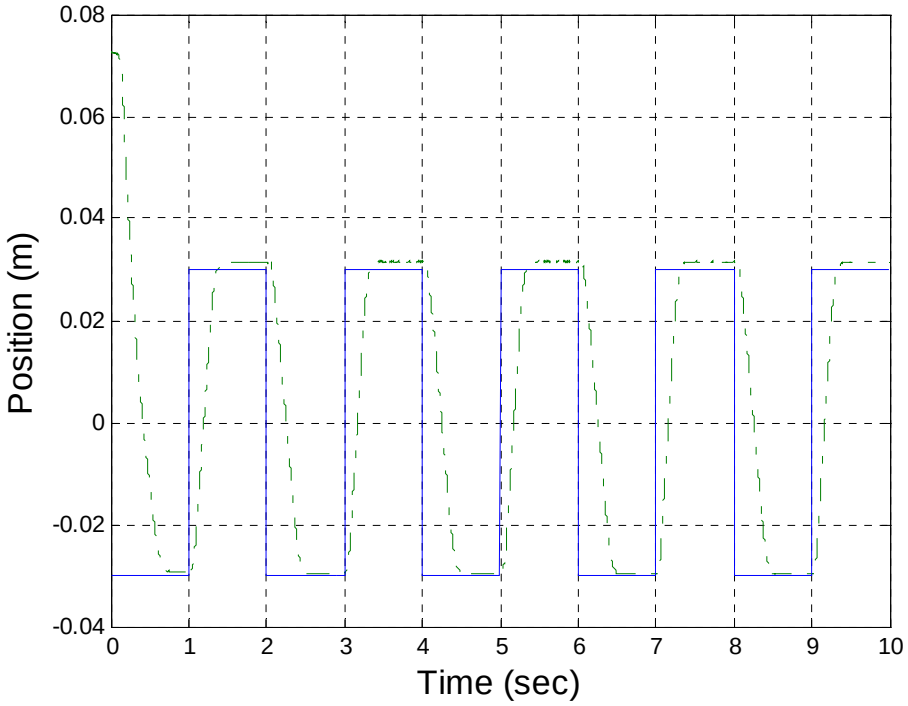

Fig. 3-10b. Desired (solid) and actual (dashed) position at 0.5 Hz square-wave frequency tracking using pressure observers

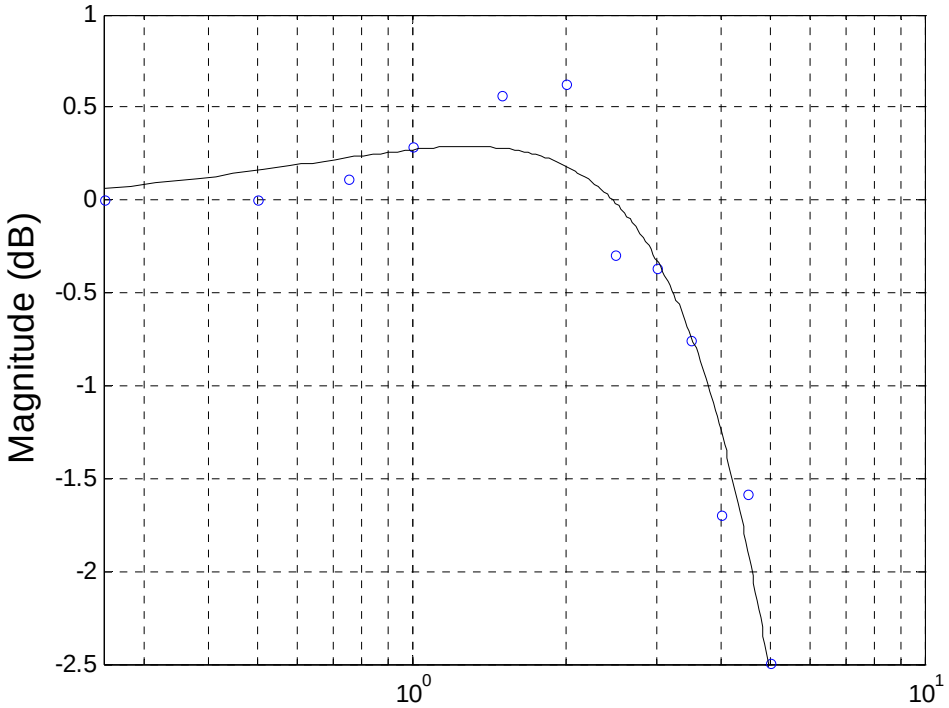

Fig. 3-11a. Closed-loop magnitude plot of the system with the controller using pressure observers

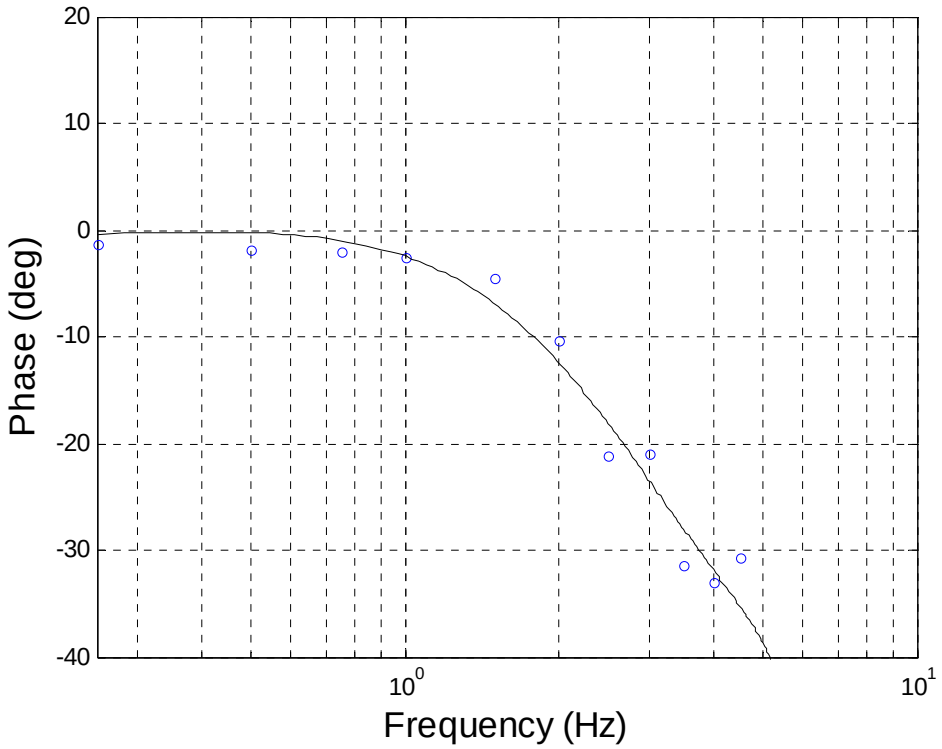

Fig. 3-11b. Closed-loop phase plot of the system with the controller using pressure observers

CHAPTER IV

MANUSCRIPT III

PRESSURE OBSERVER DESIGN AND SERVO CONTROL OF ENERGY AND POWER DENSE CHEMOFLUIDIC ACTUATORS

Navneet Gulati and Eric J. Barth

Department of Mechanical Engineering

Vanderbilt University

Nashville, TN 37235

Submitted as a Full Paper to the

ASME/ IEEE Transactions on Robotics

Abstract

This paper presents a model-based control design architecture for the position control of energy and power dense monopropellant powered chemofluidic actuators. This type of actuation system has been shown to have an actuation potential an order of magnitude better than a conventional battery powered DC motor based actuation system of similar mechanical power output. However, for the full state closed loop control of such chemofluidic actuators, the requirement of two high-temperature pressure sensors per actuated degree of freedom increases the cost of the system by a non-trivial amount. In order to reduce the initial cost, of which a large share is due to the pressure sensors, a non-linear pressure observer previously developed by the authors for pneumatic actuators is further developed for use with chemofluidic actuators. Simulation and experimental results are presented that show the effectiveness of the pressure observer and the suitability of the proposed observer/controller for stable tracking of the load at a band-width sufficiently high for many mobile robot applications.

1. Introduction

The increasing use of untethered mobile robots has necessitated the development of power supply and actuation systems that can deliver human-scale power for extended periods of time. Presently, mobile robots typically use a combination of electrochemical batteries and DC motors for their power supply and actuation system. It has been shown by the authors [1-3] that such actuation systems severely lack the fundamental energy and power density required for a useful human-scale service robot. As an example, the current state of the art humanoid robot (named P3) developed by Honda, while extremely

advanced in terms of its control and agility, is capable of 15 to 25 minutes of untethered autonomous operation, depending on its workload. Further, the nickel-zinc batteries are heavy and contribute about 30 kg in the total mass of 130 kg of the robot. This illustrates a major technological barrier to the development of power autonomous human-scale untethered mobile robots. To overcome this problem, some researchers have proposed proton exchange membrane fuel cells [4] or solid oxide fuel cells [5] as an alternative to batteries, but both have significant power density limitations relative to the average power requirements of a human-scale robot. Some other authors suggested the use of internal combustion engines to power fluid-powered systems, but such an approach is hampered by several issues, including the relative inefficiency of small engines, the loss of power necessitated by controlling power produced outside the control loop, noise problems, noxious exhaust fumes, and start-stop problems for a low duty cycle use. Additionally, such systems would be heavy and require oxidizers for combustion that make it burdensome for some applications (such as space exploration or other non-oxygen environments).

Another class of fuels, the monopropellants, are energy dense (relative to electrochemical batteries), and are capable of converting their stored chemical energy into pressurized gas within a small simple package – a catalyst pack. This energetic substance (fuel) and configuration has the potential to offer a higher system level energy density, and higher or comparable power density than current state of the art power supply and actuation systems and therefore hold promise in meeting the actuation requirements of autonomous untethered robots. Many monopropellants decompose when they come in contact with a catalyst material. The resulting heat energy can be transduced

to mechanical energy via the pneumatic domain within a pneumatic actuator. The development of this kind of chemofluidic actuator was first published by Goldfarb et al. [3] where they presented their preliminary results using hydrogen peroxide monopropellant. It was shown by the authors that chemofluidic actuators have five times better actuation potential than conventional battery / DC motor based actuators. Two configurations were shown by the authors capable of extracting controlled mechanical work from hot gaseous products. The first configuration known as the centralized system (Figure 4-1), which is pursued in this paper, is essentially based on the principle of standard pneumatic actuation systems. In this type of configuration, liquid hydrogen peroxide is stored in a pressurized blow-down tank. The controlled flow of hydrogen peroxide through the catalyst pack is governed by a discrete valve. When hydrogen peroxide comes in contact with the catalyst, it decomposes into steam and oxygen. These resultant hot gaseous products are collected in a reservoir. The hot reservoir then serves as a pressure source to one or more pneumatic actuators via pneumatic four-way proportional valves. A controlled amount of fluid is provided to either of the two chambers of the actuator depending on the force and the load requirements. In the second configuration, termed direct injection, the piston output is controlled by injecting the hot gaseous products directly into the chambers from the catalyst pack. Therefore, this configuration necessitates the use of two catalyst packs, one for each chamber of the cylinder. The output in this type of system is controlled with the help of valves that governs the flow of a monopropellant to the catalyst packs, as well as an exhaust valve that depressurizes each chamber by exhausting the gaseous products to the external environment.

The only work for the control of the centralized configuration was reported by Goldfarb et al. [3]. In their work, the authors used a non-model based PVA controller for the servo control of the inertial load. While this work did achieve position control without utilizing pressure sensors, the main motivation of their work was to determine an energetic figure of merit for the monopropellant-powered actuation system with an adequate precision of control. In the work presented in this paper, a model-based control methodology is presented for the position control of an inertial load. The motivation herein is thus to achieve precise robust and model-based control without adding further sensing requirements, namely pressure sensors, than the prior work by Goldfarb et al. [3].

While the chemofluidic actuator has the appeal of being simple and compact in design, it is fairly complex in terms of the physics of its operation. The complex interaction between several energy domains and the nonlinear nature of many of them necessitates a model-based control design to provide accurate, high-bandwidth, efficient, stable operation as generally required of a mobile robot platform. The model of the system was derived and discussed in references [6, 7] and is stated in summary in the next section for completeness. The proposed control architecture for the centralized configuration of the monopropellant powered actuators is divided in two parts. The first part of the control problem is the pressurization and regulation of the hot gas reservoir (dotted area of Figure 4-1a). The functional requirement of the reservoir is to maintain a uniform desired pressure with minimum pressure fluctuations. Since a transportation delay of 15 ms is present in the experimental system investigated here, a predictive control based design is best suited for this system. It should be noted that the inlet liquid fuel channel has a binary on/off valve and hence techniques such as the Smith filter,

which deals with time delay, cannot be implemented. The binary on/off valve is selected because no commercially available valve could be identified that could meter the low flow rate of monopropellant required for this application. The second part of the control problem is the stable servo control of the inertial load. The Lyapunov-based sliding mode control technique is selected for the motion because of its robustness in dealing with model uncertainties, as well as uncertainties resulting from the pressure observers that will be implemented here.

To prevent the addition of pressure sensors, which were not present in the initial control design by Goldfarb et al. [3] due to the non model-based nature of the controller, and to limit the initial cost of such chemofluidic actuators, a pressure observer is developed in this paper. By providing actuator pressures, a model-based control design can be pursued. The chemofluidic system is characterized by four states, viz. position, velocity, and pressures in both chambers of the actuator. Logical sensors to select for such a system would be a potentiometer for measuring the position and two pressure sensors per axis (one for each chamber of the compressible gas actuator). The velocity and acceleration signals can be obtained by differentiating the position and velocity signals respectively. The problem with the pressure measurement is that the high-bandwidth, high-temperature, and high-pressure sensors required for the control of the servo system are expensive and large (relative to the actuator – see Figure 4-1c) with a typical cost between $400 and $1200. Since pneumatic actuation requires two pressure sensors per axis, these sensors add $800 to $2400 per axis of monopropellant based servo system. In order to make the chemofluidic system more cost effective, a Lyapunov-based nonlinear pressure observer is developed in this paper to dispense of the pressure sensors.

This observer design is an extension of the work on observes by the authors [8] for pneumatic actuation systems. In their work, the authors presented two design methods for pressure observers. In this paper, one of the two designs, the energy-based pressure observer, is extended for chemofluidic actuators due to its structural simplicity, ease of implementation, and its independence on acceleration of the load which reduces noise problems. This observer utilizes the available knowledge of other states and inputs of the system to reconstruct the pressure states. The elimination of pressure sensors reduces the initial cost of the system by more than 50 percent.

The organization of the paper is as follows. In the next section, a model of the chemofluidic actuators is briefed. The subsequent section discusses the control architecture and the development of a feedback control law for the system. In section 4, the design of the pressure observer is presented. Section 5 and 6 discusses the experimental setup and experimental results of servo control and the pressure observer.

2. Model

Please refer to Figure 4-1a for component configuration of the system.

2.a. Liquid Propellant Valve

The liquid propellant valve is the control element of the actuation system's high pressure reservoir. Accurate control of the system requires the flow of precise amount of monopropellant via the valve. The mass flow rate ($\dot{m}_{in}$) through the valve is a derived using Euler's equation and Continuity equations and is stated as follows:

$$\dot{m}_{in} = C_1 A_0 \sqrt{(P_u - P_i)} \tag{1}$$

where, C_1 is a function of fluid density and the discharge coefficient of the valve, and is a constant for a given fluid; A_0 (m^2) is the flow orifice area of the valve; P_u and P_i are the upstream and downstream pressures (N/m^2 or Pa) of the valve respectively.

2.b. Catalyst Pack

The catalyst pack is the component where the catalytic decomposition of the monopropellant takes place resulting in the liberation of heat. The catalyst bed also offers resistance to the flow of both the reactant and the resultant gaseous products. The catalyst pack is modeled in two parts. In the first part, the flow resistance offered by the catalyst bed is modeled. The other part captures the reaction dynamics and the energy released by the decomposition of hydrogen peroxide.

The flow resistance of the hydraulic valve is modeled by the following equation:

$$\dot{m}_{in} = C_2 A_{cat} \sqrt{(P_i - P_d)} \tag{2}$$

where, C_2 is a constant for a given fluid; A_{cat} (m^2) is the effective flow orifice area of the catalyst pack; P_i and P_d are the upstream and downstream pressures (N/m^2 or Pa) of the catalyst pack respectively. Since the mass flow rate is same through the valve and the catalyst pack, eliminating P_i from the above equations:

$$\dot{m}_{in} = C^* \sqrt{(P_u - P_d)} \text{ . where } C^* = \frac{(C_1 A_0)(C_2 A_{cat})}{\sqrt{(C_1 A_0)^2 + (C_2 A_{cat})^2}} \tag{3}$$

The above equation describes the input-output dynamic behavior of the inlet valve as shown in Figure 4-1b. The control input of the block is the orifice area of the valve and the output is the mass flow rate of the propellant.

The heat released in the catalyst pack can be derived using the rate form of the first law of thermodynamics, and is given by the following relationship (with a slight abuse of notation where *s* represents the derivative operator in the usual Laplace domain sense):

$$\frac{(\dot{H}_{cat})_{out}}{\dot{m}} = [c_p T_{in} + \frac{\Delta H_r}{\tau s + 1} - k_{cat} \frac{\Delta H_r}{\tau s + 1}] \tag{4}$$

where, $(\dot{H}_{cat})_{out}$ is the rate of change of enthalpy leaving the catalyst pack; c_p ($J/kg \cdot K$) is the average specific heat of the liquid monopropellant at a constant pressure; T_{in} (K) is the temperature of the liquid entering the catalyst pack; ΔH_r (J) is the heat released per kilogram of hydrogen peroxide; and k_{cat} is the heat transfer coefficient representing heat loss through the catalyst pack walls.

The time "constant" in equation (4) is defined by the following:

$$\tau = \frac{1}{K_o e^{-E_a/RT}} \tag{5}$$

where E_a (J/mol) is the activation energy of hydrogen peroxide; T is the temperature inside the catalyst pack ; K_o is the pre-exponential factor; and $e^{-E_a/RT}$ is the Boltzmann factor.

The input-output relationship of the catalyst pack in Figure 4-1b is characterized by equation (4). The input to the catalyst pack is the mass flow rate of the monopropellant and the output is the enthalpy flow rate.

2.c. Hot Gas Reservoir and Actuator

The dynamic equations of the actuator and the hot gas reservoir are similar and were derived using an energy balance equation as per the first law of thermodynamics to obtain:

$$\dot{P}_{(a,b)} = \frac{\frac{R}{c_v}[(\dot{H}_{ch})_{in} - (\dot{H}_{ch})_{out} - \dot{Q}]_{(a,b)} - \gamma P_{(a,b)}\dot{V}_{(a,b)}}{V_{(a,b)}} \tag{6}$$

In the above equation subscripts 'a' and 'b' represent the properties of chambers 'a' and 'b' of the cylinder respectively, or in the case of the reservoir no subscript is needed. P (Pa) is the pressure in the chamber; V (m^3) is the volume of the chamber; $\dot{Q}(J/s)$ is the rate of heat lost to the environment; $(\dot{H}_{ch})_{in}$ and $(\dot{H}_{ch})_{out}$ are the rate of change of enthalpy entering and leaving the specified chamber respectively; γ is the ratio of the specific heat at constant pressure to the specific heat at constant volume, $\gamma = \frac{c_p}{c_v}$. The equation (6) above establishes the input-output dynamic behavior of the hot gas reservoir (where $\dot{V} = 0$) and each pneumatic actuator chamber (refer Figure 4-1b). The inputs are the enthalpy rates flowing in and out of the specified actuator or reservoir chamber. The output of the block is the rate of change of the pressure in the chamber.

2.d. Hot Gas 4-way Proportional Valve

The mass flow rate, and hence the rate of change of enthalpy entering and leaving the actuator chambers as governed by the hot gas 4-way proportional valve, depends on the upstream and downstream pressures. The mass flow rate increases with the increase in the ratio of upstream to downstream pressure. The flow rate becomes saturated for a

given orifice area when the velocity of flow at the orifice reaches the speed of the sound. The flow rate through a given side of the 4-way proportional valve under subsonic and sonic conditions is given as follows and is based on Euler's equation and the Continuity equation:

$$\dot{m} = \begin{cases} \dfrac{C_e A_v P_u}{\sqrt{T_e}} \sqrt{\dfrac{(2\gamma)}{(\gamma-1)R}\left((\dfrac{P_d}{P_u})^{2/\gamma} - (\dfrac{P_d}{P_u})^{(\gamma+1)/\gamma} \right)} & if \ \dfrac{P_d}{P_u} > \left(\dfrac{2}{\gamma+1}\right)^{\gamma/(\gamma-1)} \\ \dfrac{C_e A_v P_u}{\sqrt{T_e}} \sqrt{\dfrac{2\gamma}{\gamma+1}\left(\dfrac{2}{\gamma+1}\right)^{2/\gamma-1}} & otherwise \end{cases} \tag{7}$$

where C_e is the discharge coefficient of the valve; A_v (m^2) is the flow orifice area of the valve; P_u *(Pa)* and P_d (*Pa*) are the upstream and downstream pressure of the valve respectively; T_e *(K)* is the temperature of gaseous products; γ is the ratio of the specific heat at constant pressure (c_p) to the specific heat at constant volume (c_v), $\gamma = \dfrac{c_p}{c_v}$. The input-output relationship of the valve in Figure 4-1b is given by the equation (7). The input to this block is the valve's flow orifice area (where it is assumed that the proportional valve is furnished with an inner loop high-bandwidth closed-loop controller of the orifice area, i.e. closed-loop valve spool position), while the output is the enthalpy rate flowing into or out of each of the actuator's chambers.

2.e Inertial Load

The dynamic equation for the piston-rod-load assembly shown in Figure 4-1 is derived using a force balance (Newton's second law) and can be expressed as:

$$M\ddot{x} + B\dot{x} + F_c = P_a A_a - P_b A_b - P_{atm} A_r \tag{8}$$

where, M (kg) is the mass of the load; B is the viscous friction coefficient; F_c (N) is the Coulomb friction; P_a and P_b (N/m^2 or Pa) are the absolute pressure in each chamber of the cylinder, P_{atm} (N/m^2 or Pa) is the absolute environmental pressure; A_r (m^2) is the cross-sectional area of the rod, and A_a and A_b (m^2) are the effective piston areas in chambers 'a' and 'b', respectively.

3. Control Design

3.a Predictive Control Design for the Reservoir

As mentioned previously, a transportation delay of 15ms is present between the opening of the valve and the monopropellant reaching the catalyst pack. The liquid propellant valve is a binary valve, therefore, a pulse width modulation (PWM) controller (as developed in references [9, 10]) could be implemented. However, the limited switching speed of the valve would severely limit the bandwidth of the controller and hence it renders PWM approach not as effective for this case. A predictive control approach has been shown to be effective for systems with time delays. To take into account the delay of 15ms, a predictive controller is implemented for pressurization and pressure regulation of the hot gas reservoir. The predictive controller theory was developed in references [11, 12] for the direct injection configuration and is adopted here. In this prior work, a predictor is implemented (using dynamics derived in references [6, 7]) that at each time step convolves the effect of each next possible discrete control choices. It also takes in account the past control inputs that have occurred in the recent past but have not yet affected the system output due to the transportation delay present in

the system. The available control choice (open or close) that takes the system closest to the desired future state is the preferred choice of the controller.

For the pressurization of the fixed volume reservoir ($\dot{V}$ =0), the dynamic equation (6) reduces to the following:

$$\dot{P} = \frac{(R/c_v)}{V}[\dot{H}_{in} - \dot{H}_{out} - \dot{Q}] \tag{9}$$

In this case, $\dot{H}_{in}$ is the rate of enthalpy flowing in the hot gas reservoir. If the heat losses between the catalyst pack and the reservoir are neglected, then $\dot{H}_{in} = (\dot{H}_{cat})_{out}$. In order to get a closed form solution of the above equation, a requirement to implement the predictive control design, $\dot{H}_{out}$ and $\dot{Q}$ are treated as the disturbance present in the system. Therefore, the final equation for the rate of change of pressure without disturbances for control purposes reduces to

$$\frac{\dot{P}}{\dot{m}} = \frac{(R/c_v)}{V}[\frac{\Delta H_r}{\tau s + 1} - k_{cat}\frac{\Delta H_r}{\tau s + 1}]e^{-T_u s} \tag{10}$$

where $e^{-T_u s}$ in the above equation represents the time delay of T_u seconds present in the system.

The above equation can be represented in state-space form as follows:

$$\dot{x}(t) = Ax(t) + Bu(t - T_u) \tag{11}$$

where, $x = [P \quad \dot{P}]^T$; $A = \begin{bmatrix} 0 & 1 \\ 0 & -1/\tau \end{bmatrix}$ and $B = \begin{bmatrix} 0 \\ \frac{\Delta H_r (1 - k_{cat})(R/c_v)(1/V)}{\tau} \end{bmatrix}$

For each candidate control input $u_i \in [0, 1]$, the predicted future states $\hat{x}_{u_i}(t + T_u + T_d)$ can be described by (convolution integral):

$$\hat{x}_u(t+T_u+T_d) = e^{A(T_u+T_d)}x(t) + \int_{t}^{t+T_u} e^{A(t+T_u+T_d-\tau)}Bu(\tau-T_u)d\tau + \int_{t+T_u}^{t+T_u+T_s} e^{A(t+T_u+T_d-\tau)}Bu_i d\tau \quad (12)$$

The first term on the right hand side represents the unforced response, the second term accounts for all the inputs that have already occurred but have yet to affect the system due to the time delay (T_u), and the third term is the effect that the next input will have on the future state. T_d in the above equation is the prediction horizon, T_s is the switching period (refer to Figure 4-2) or sampling frequency of the controller.

Once the future states are predicted for each possible discrete-valued control input u_i, the next control input corresponding to the minimum weighted future state (defined by $V = \frac{1}{2}s^2(t+T_u+T_d)$, where $s = (\dot{P}-\dot{P}_d) + \lambda_p(P-P_d))$ is selected. This procedure effectively minimizes the magnitude of the Lyapunov function ($V = \frac{1}{2}s^2$) on the prediction horizon. It is shown in references [11, 12] that the predictive controller is bounded-input bounded-output stable where the error dynamics is bounded by, $|e| \le \frac{\psi}{\lambda_p^{n-1}}$, where Ψ is the upper bound on the sliding surface, s, such that $|s| \le \psi$ and λ_p is a positive constant.

3.b Sliding Mode Control Design

In this paper, a Lyapunov based sliding mode controller structure was chosen due to its suitability and effectiveness for higher order nonlinear systems in the presence of bounded uncertainties on the parameters of the system's dynamic model. In order to derive the control law, a time-varying sliding surface is defined in the typical fashion, which is the weighted sum of the error and its derivatives representing the desired error

dynamic. In this case, the error is the difference between the actual and desired position of the actuator. The general form of the time varying surface is as follows:

$$s = \left(\frac{d}{dt} + \lambda \right)^{n-1} e \tag{13}$$

where, λ is a strictly positive number, n is the number of times the output must be differentiated to get the input, and e is the error. Since the dynamics of the system are of 3rd order, the above equation reduces to the following:

$$s = (\ddot{x} - \ddot{x}_d) + 2\lambda\dot{e} + \lambda^2 e \tag{14}$$

Differentiating equation (14) and making the required substitutions and neglecting Coulomb friction results in:

$$\dot{s} = \frac{1}{M}(\dot{P}_a A_a - \dot{P}_b A_b - B\ddot{x}) - x_d^{(3)} + 2\lambda\ddot{e} + \lambda^2\dot{e} \tag{15}$$

In the control of the flow of hot gaseous products to chambers of the cylinder, a four-way proportional valve is used. Therefore, the kinematic configuration of the 4-way spool imposes the following constraint regarding the flow orifice areas during charging / discharging of the actuator chambers,

$$A_v = A_{v_a} = -A_{v_b} \tag{16}$$

where the signed area is used to represent a connection to the supply reservoir (positive) or to the atmosphere (negative). In order to get the expression of equivalent control law, $\dot{s}$ is forced to zero providing marginal stability, in the sense of Lyapunov, to the system. The control input A_v then appears in both $\dot{P}_a$ and $\dot{P}_b$. In equation (6), $\dot{H}_{ch}$ is calculated using the following relation:

$$(\dot{H}_{ch})_{in/out} = \dot{m}[x_{O_2}(c_p)_{O_2} T_{ex} + x_{H_2O}(h_f + xh_{fg})] \tag{17}$$

where $\dot{m}$ ($kg/\sec$) is the mass flow rate through the 4-way proportional valve and can be calculated using equation (7) with appropriately defined upstream and downstream pressures; $(c_p)_{O_2}$ ($J/kg \cdot K$) is the average specific heat of oxygen at a constant pressure; h_f (J/kg) is the specific enthalpy of saturated liquid; h_{fg} (J/kg) is the specific enthalpy of vaporization; x is the dryness fraction of steam. x_{O_2} and $x_{H_2O_2}$ are the fraction of oxygen and hydrogen peroxide per kilogram of the exhaust products; T_{ex} (K) is the temperature of the exhaust products.

Substituting the values of $\dot{P}$, imposing the constraint, and simplifying, results in the following equivalent control law:

$$A_{v_{eq}} = \frac{\gamma \dot{x}\left(\frac{P_a A_a^2}{V_a} + \frac{P_b A_b^2}{V_b}\right) + \left(\frac{(\gamma-1)}{V_a}\dot{Q}_a - \frac{(\gamma-1)}{V_b}\dot{Q}_b\right) B\ddot{x} + M(x_d^{(3)} - 2\lambda\ddot{e} - \lambda^2\dot{e})}{(\gamma-1)C_f\left(\frac{P_{u_a}\psi_a(P)\phi_a(T)A_a}{V_a\sqrt{T_a}} + \frac{P_{u_b}\psi_b(P)\phi_b(T)A_b}{V_b\sqrt{T_b}}\right)} \tag{18}$$

where,

$$\psi(P) = \begin{cases} P_u\sqrt{\frac{\gamma}{R}\left(\frac{2}{\gamma+1}\right)^{\frac{(\gamma+1)}{(\gamma-1)}}} & \textit{for choked flow} \\ P_u\left(\frac{P_d}{P_u}\right)^{\frac{1}{\gamma}}\left(\sqrt{1-\left(\frac{P_d}{P_u}\right)^{\frac{(\gamma-1)}{\gamma}}}\right)\left(\sqrt{\frac{2\gamma}{R(\gamma-1)}}\right) & \textit{otherwise} \end{cases} \tag{19}$$

and

$$\phi(T) = [x_{O_2}(c_p)_{O_2}T_{ex} + x_{H_2O}(h_f + xh_{fg})] \tag{20}$$

In order to ensure robustness of the controller and for uniform asymptotic stability, the typical robustness term is added to the equivalent control term that yields:

$$A_v = A_{v_{eq}} - k * sat(s/\phi) \tag{21}$$

where k is a strictly positive gain and captures uncertainties of the model and the pressure observer; Φ is the boundary layer thickness and selected such as to avoid excessive chattering across the sliding surface while maintaining the desired performance of the system.

4. Observer

Energy-Based Lyapunov Observer Design

In this method, a Lyapunov function is chosen based on the pneumatic energy stored in the actuator. The pressure is estimated based on the following observer equation:

$$\dot{\hat{P}}_{(a,b)} = \frac{(R/c_v)}{V_{(a,b)}}[(\dot{\hat{H}}_{ch})_{in} - (\dot{\hat{H}}_{ch})_{out} - \dot{Q}]_{(a,b)} - \frac{\gamma \dot{V}_{(a,b)}}{V_{(a,b)}}\hat{P}_{(a,b)} \tag{22}$$

where, $\hat{P}$ in the above equations represents the estimated pressure and $\dot{\hat{H}}$ represents the estimated enthalpy flow rate based on the estimated pressure and a known valve orifice area $A_{V_{(a,b)}}$.

In order to show the convergence between the actual pressures and the estimated pressures obtained from the above equations, the following positive definite candidate Lyapunov function is chosen for this method:

$$V = \frac{1}{2}(\tilde{P}_a V_a)^2 + \frac{1}{2}(\tilde{P}_b V_b)^2 \tag{23}$$

where, $\tilde{P}_a$ and $\tilde{P}_b$ represents the error between the actual pressure and the estimated pressure in chambers 'a' and 'b' respectively ($\tilde{P}_{(a,b)} = P_{(a,b)} - \hat{P}_{(a,b)}$). It should be noted

that the Lyapunov function chosen is based on the energy stored in the cylinders of a pneumatic actuator and represents the difference between the actual and observed stored energies.

Equation (23) can be rewritten as:

$$V = \frac{1}{2}(P_a V_a - \hat{P}_a V_a)^2 + \frac{1}{2}(P_b V_b - \hat{P}_b V_b)^2 \tag{24}$$

Differentiating equation (24) results in:

$$\dot{V} = (P_a V_a - \hat{P}_a V_a)(\dot{P}_a V_a + P_a \dot{V}_a - \dot{\hat{P}}_a V_a - \hat{P}_a \dot{V}_a) + (P_b V_b - \hat{P}_b V_b)(\dot{P}_b V_b + P_b \dot{V}_b - \dot{\hat{P}}_b V_b - \hat{P}_b \dot{V}_b) \tag{25}$$

If the process of charging and discharging of air in the cylinder is considered as isothermal (i.e., $\gamma = 1$), then using equation (6) following substitutions can be made in equation (25):

$$\dot{P}_{(a,b)} V_{(a,b)} + P_{(a,b)} \dot{V}_{(a,b)} = \frac{R}{c_v}(\dot{H}_{ch_{(a,b)}} - \dot{Q}_{(a,b)}) \qquad \text{and}$$

$$\dot{\hat{P}}_{(a,b)} V_{(a,b)} + \hat{P}_{(a,b)} \dot{V}_{(a,b)} = \frac{R}{c_v}(\dot{\hat{H}}_{ch_{(a,b)}} - \dot{Q}_{(a,b)}) \tag{26}$$

Substitution of equation (26) in equation (25) yields:

$$\dot{V} = \frac{R}{c_v} V_a (P_a - \hat{P}_a)[(\dot{H}_{in})_a - (\dot{\hat{H}}_{in})_a] - \frac{R}{c_v} V_a (P_a - \hat{P}_a)[(\dot{H}_{out})_a - (\dot{\hat{H}}_{out})_a] + \tag{27}$$

$$\frac{R}{c_v} V_b (P_b - \hat{P}_b)[(\dot{H}_{in})_b - (\dot{\hat{H}}_{in})_b] - \frac{R}{c_v} V_b (P_b - \hat{P}_b)[(\dot{H}_{out})_b - (\dot{\hat{H}}_{out})_b]$$

As noted earlier, a four-way proportional spool valve is used for charging and discharging of chambers of the actuator. Therefore, when it charges one chamber, it discharges the other chamber and vice versa. It should be noted that the same chamber cannot be charged or discharged simultaneously due to the constraint imposed by the

four-way proportional spool valve. With this constraint, the scalar function $\dot{V}$ can be shown as negative semi-definite with the following cases:

Case I: Charging chamber 'a' and discharging chamber 'b'

During the charging of chamber 'a' and discharging of chamber 'b', terms $(\dot{H}_{out})_a$, $(\dot{\hat{H}}_{out})_a$, $(\dot{H}_{in})_b$ and $(\dot{\hat{H}}_{in})_b$ are zero due to the constraint of the valve. The term $(P_a - \hat{P}_a)[(\dot{H}_{in})_a - (\dot{\hat{H}}_{in})_a]$ is always non-positive for the charging process of chamber 'a'. During the charging process for a known valve orifice area, if the actual pressure in the chamber 'a' is higher than the estimated pressure, then the actual flow rate will be less than the estimated flow rate. This is because a higher downstream pressure results in a lower mass flow rate, and consequently in a lower enthalpy flow rate, in the case of unchoked flow. For the case of choked flow, $\dot{H}$ and $\dot{\hat{H}}$ will be equal as the flow rate is only a function of known supply pressure. For the discharging of chamber 'b', the term $(P_b - \hat{P}_b)[(\dot{H}_{out})_b - (\dot{\hat{H}}_{out})_b]$ is always positive definite because a higher actual pressure will result in a higher mass flow rate than the estimated mass flow rate. Consequently, the enthalpy flow rate would be higher. Due to the pressure in 'b' being the driving pressure for the case of discharging, this will occur in the presence of either choked or unchoked flow. Therefore, it can be concluded that the scalar function is negative definite during the charging process of chamber 'a'.

Case II: Charging chamber 'b' and discharging chamber 'a'

During the charging of chamber 'b' and discharging of chamber 'a', terms $(\dot{H}_{out})_b$, $(\dot{\hat{H}}_{out})_b$, $(\dot{H}_{in})_a$ and $(\dot{\hat{H}}_{in})_a$ are zero because of the constraint of the valve. Using the similar arguments as used in Case I, it can be shown that terms $(P_a - \hat{P}_a)[(\dot{H}_{out})_a - (\dot{\hat{H}}_{out})_a]$ and $(P_b - \hat{P}_b)[(\dot{H}_{in})_b - (\dot{\hat{H}}_{in})_b]$ are positive definite and non-positive respectively. Hence, the scalar function $\dot{V}$ is negative definite.

Case III: No charging or discharging of the chambers

This case will result in a singularity point. At these singular points, i.e. when the velocity and control input is zero, the value of the scalar function $\dot{V}$ is zero. Consequently, it can be inferred that the error will not *diverge* away from the real values. Since $\dot{V}$ is negative semi-definite, the equilibrium point where $V = 0$ is stable.

5. Experimental Setup

Figure 4-1c shows the experimental setup developed for verification of the combined pressure observer and servo control of the inertial load. This prototype was fabricated in-house and is a representation of a single-degree-of-freedom translational motion of a robotic arm. A schematic of the system setup is illustrated in Figure 4-1a. The liquid monopropellant is stored in a pressurized blow-down stainless steel tank which in turn is connected to a catalyst pack via a solenoid actuated on/off valve (Parker/ General Valve model 009-581-050-2). The catalyst material used in this experiment is Shell 405 granules, which is iridium coated alumina, and is packed inside a 5 cm long and 1 cm diameter stainless steel tube trapped between screens at both ends. The output of the catalyst pack is directly connected to the hot gas reservoir of volume 75 cubic

centimeters. A high-temperature pressure transducer (Omega PX32B1-250GV) is connected to the reservoir for measuring the reservoir pressure. A four-way proportional spool valve is used to control the charging and discharging process of both chambers of the actuator cylinder. This proportional valve was customized for high-temperature applications. For this, the standard solenoid actuator of a commercially available solenoid-actuated 4-way valve (Numatics Microair model #M11SA441M) was replaced by a thermally isolated voice coil (BEI model #LA10-12-027A). A linear potentiometer (Midori model #LP10-FQ) is also incorporated in the valve for closed-loop control of the spool position.

The pneumatic cylinder (BIMBA) of stroke length of 4 inches is connected to the inertial mass of 2 kilograms. Two pressure transducers (Omega PX32B1-1KGV) are used to measure the chambers pressure of the cylinder. The position of the inertial load is measured with the help of a linear potentiometer (Midori LP-150F) of travel length of 100 mm, which enables closed-loop servo control. The velocity signals are obtained by an analog differentiator with a first order roll-off at 50 Hertz. Similarly, acceleration signals are obtained by analog differentiation of the velocity signals with a first order roll-off of 50 Hertz. The control and observer algorithms are implemented using Real Time Workshop (RTW) on a 256 MB RAM Pentium IV computer. An A/D card (National Instruments PCI-6031E) is used for the communication between the computer and the physical setup.

For the experimental verification of the control design, initially the pressure sensors were used for position servo control of the load at sinusoidal frequencies between 0.25 Hertz to 4 Hertz. Simultaneously, the pressure response in both chambers of the

actuator was compared to the response obtained with pressure observers. Similarly, the closed-loop position step response of the system was obtained. Thereafter, the pressure sensors were disconnected from the setup and the sinusoidal and step servo response of the system was obtained by utilizing the states constructed by the pressure observers. The tracking performance comparison of the system with and without pressure sensors are presented in the following section.

6. Results and Discussion

Figure 4-3a shows the position tracking results of the inertial mass using pressure sensors at a sinusoidal frequency of 0.5 Hertz and amplitude of 15 millimeters. The solid line in the figure shows the desired trajectory while the dotted line shows the actual trajectory followed by the mass. The result of the predictive controller for pressure regulation inside the hot-gas reservoir is shown in Figure 4-3e. The solid line in this figure shows the desired pressure and the dotted line represents the actual pressure in the hot gas reservoir. The pressure inside the hot gas reservoir quickly rises to the desired pressure and then it is regulated close to the desired pressure. The accurate tracking of the inertial mass and the adequate pressure regulation shows the overall effectiveness of the implemented model-based control structure.

Figure 4-3b shows the position tracking results at 0.5 Hertz frequency of 15 millimeters amplitude utilizing the pressure observers instead of the pressure sensors. In this experimental run generating Figure 4-3b, the pressure sensors in the chambers were physically disconnected from the system to completely ensure that no pressure sensor information was being used. As can be seen in comparing Figure 4-3b with Figure 4-3a,

the tracking performance is almost indistinguishable using pressure sensors or pressure observers. Figure 4-3c shows the results of monitoring the pressure observer in chamber 'a' during the experimental run that generated Figure 4-3a. The solid line in the figure shows the actual pressure and the dotted line represents the observed pressure in the chamber. Similarly, Figure 4-3d shows the actual and observed pressure in the chamber 'b' of the actuator. As seen from the figure, the observed pressure quickly converges to the actual pressure values. A phase lag between the observed and the actual pressure is noticeable in the figures (with the pressure observer information occurring slightly before the filtered pressure sensor information). This is presumably because of the implementation of a second order filter, with a roll-off frequency of 30 Hertz, for the conditioning of the noisy pressure transducer signals.

In all of the experiments, a PID controller is implemented for the closed-loop control of the four-way proportional spool valve. The spool position is commanded by the sliding mode controller output which is controlling the inertial load position. A frequency bandwidth of 25 Hertz was achieved for the closed-loop spool position control of the valve. In order to overcome static friction, a dither signal of 0.65 mm amplitude and 100 Hertz frequency is used.

Figure 4-6a shows the position step response of the system using pressure sensors. The corresponding response of the system using pressure observers is shown in the Figure 4-6b. In this case also, the closed-loop response of the system using pressure sensors or pressure observer is very similar and in essence identical in performance. The

pressure observer results of chambers ‘a’ and ‘b’ for this case are demonstrated in Figures 4-6c and 4-6d. Similar results for 1 Hertz and 2 Hertz sinusoidal tracking frequencies are shown in figures 4-4 and 4-5 respectively.

As observed from the figures, and other results not included in this paper, a maximum multiplicative error of ±0.6 atmospheric pressure exists between the actual and observed pressures. This error is conjectured to be mainly due to inaccuracies in the calculation of mass flow rates and thus the enthalpy flowing in or out of the chambers of the actuator. The mass flow rate is calculated based on the valve spool position which in turn is used to calculate the area of the valve. The resulting error due to these compounded calculations gets reflected in the results. The other contributing factor is the value of the discharge coefficient of the four-way proportional valve. The discharge coefficient is a function of the valve area among other factors. However, in this experiment a constant value of the discharge coefficient is used. This value was calculated based on the C_v value provided by the manufacturer. Frictional losses and time delay due to the connecting tubes are other contributing factors that add to the deviation. Despite the deviations seen between the actual and observed pressures, the phase response of the pressure observer is very good, and in fact arguably better than the filtered pressure sensor signals. In the context of control of the actuator, and as evidenced by the position tracking performance of the combined observer/controller system, the pressure observers appear to provide more than adequately quick and accurate estimated pressure states.

7. Conclusions

A model-based control design for the centralized configuration of an energy and power dense chemofluidic actuation system is presented in this paper. Additionally, an energy-based pressure observer is developed in the paper. The implementation of pressure observers instead of expensive pressure sensors reduces the initial cost of the system by more than 50 percent, in addition to contributing to a more compact actuation system in the interest of utilizing the system in an untethered mobile robot application domain. These savings and advantages are achieved without any compromise on the quality of servo tracking of the system. Although the developed observer is used for the servo control of chemofluidic actuators, it could also be used for other purposes such as condition monitoring and fault detection without the need to add more sensors. The resultant actuators are energy dense, power dense, light weight, economical, and compact. Coupled with the advantages of the chemofluidic actuators along with the accurate, precise and stable control, it will be feasible to develop energetically autonomous robots that provide energy and power density an order of magnitude greater than that provided by existing electrochemical and electromagnetic motor based actuation systems.

References

[1] Gogola, M., Barth, E. J., and Goldfarb, M., "Monopropellant-Powered Actuators for use in Autonomous Human-Scale Robotics," *IEEE International Conference on Robotics and Automation*, pp. 2357-2362, 2002.

[2] Goldfarb, M., Barth, E. J., Gogola, M. A., and Wehrmeyer, J. A., "The Design and Modeling of a Liquid-Propellant-Powered Actuator for Energetically Autonomous Robots," *ASME International Mechanical Engineering Congress and Exposition*, November 2002.

[3] Goldfarb, M., Barth, E. J., Gogola, M. A., and Wehrmeyer, J. A., "Design and Energetic Characterization of a Liquid-Propellant-Powered Actuator for Self-Powered Robots", *IEEE/ASME Transactions on Mechatronics*, Vol. 8, No.2, June 2003, pp.254-262.

[4] McCurdy, K., Vasquez, A., and Bradley, K., "Development of PEMFC systems for space power applications," First *International Conference on Fuel Cell Science, Engineering and Technology*, pp. 245-251, Rochester, NY, 2003.

[5] Tappero, F. and Kato, T., "Simulation Model of a Hybrid Power Generation System for Humanoid Robots," *Proceedings of the Fourth IASTED International Conference on Power and Energy Systems*, pp. 550-556, Rhodes, Greece, 2004.

[6] Barth, E. J., Gogola, M. A., Goldfarb, M., "Modeling and Control of a Monopropellant-Based Pneumatic Actuation System", *IEEE International Conference on Robotics and Automation*, Vol. 1, pp. 628-633, 2003.

[7] Gulati, N., "*Modeling and Observer-Based Robust Control Design for Energy-Dense Monopropellant Powered Actuators*", Ph.D. Thesis, Vanderbilt University, Nashville, TN, 2005.

[8] Gulati, N. and Barth, E., "Non-linear Pressure Observer Design for Pneumatic Actuators", *IEEE/ ASME International Conference on Intelligent Mechatronics*, Monterey, CA, 2005.

[9] Barth, E. J., Zhang, J., and Goldfarb, M., "Control Design for Relative Stability in a PWM-Controlled Pneumatic System," *ASME Journal of Dynamic Systems, Measurement, and Control*, vol. 125, no. 3, pp. 504-508, 2003.

[10] Ye, N., Scavarda, S., Betemps, M., and Jutard, A., "Models of a Pneumatic PWM Solenoid Valve for Engineering Applications," *ASME Journal of Dynamic Systems, Measurement, and Control*, vol. 114, no. 4, pp. 680-688, 1992.

[11] Shields, B. L., Barth, E. J., and Goldfarb, M., "Predictive Pressure Control of Monopropellant Powered Actuator," *Proceedings of the 2003 ASME International Mechanical Engineering Congress & Exposition*, Washington, D.C., 2003.

[12] Shields, B. L., "Development of a Solenoid Injected Liquid Monopropellant Actuator for Self-Powered Robots", Ph.D. Thesis, Vanderbilt University, Nashville, TN, 2005.

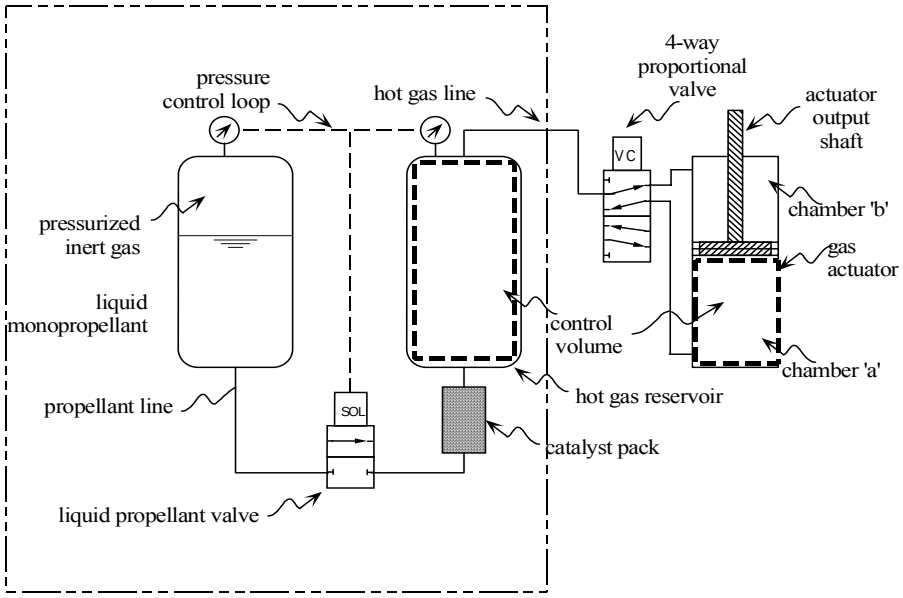

Fig 4-1a. Schematic of the centralized monopropellant actuation system

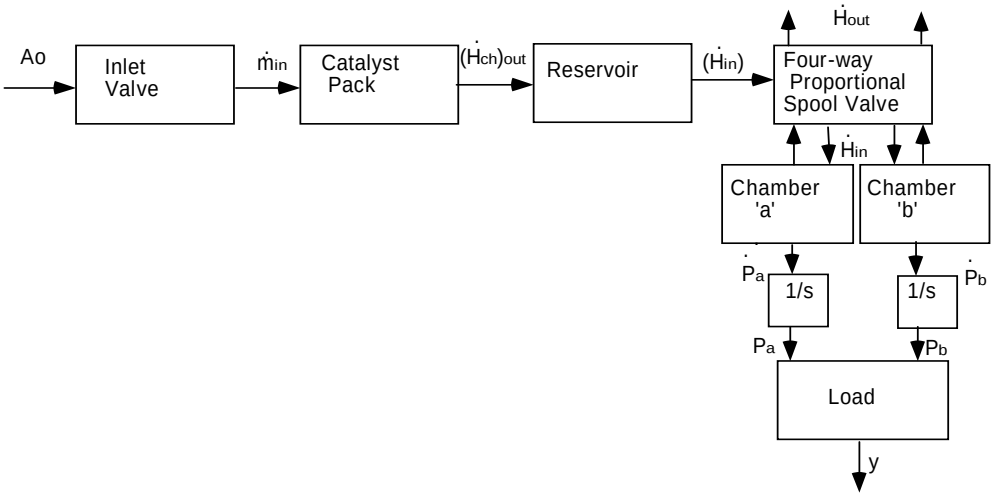

Fig 4-1b. Block diagram of the centralized configuration

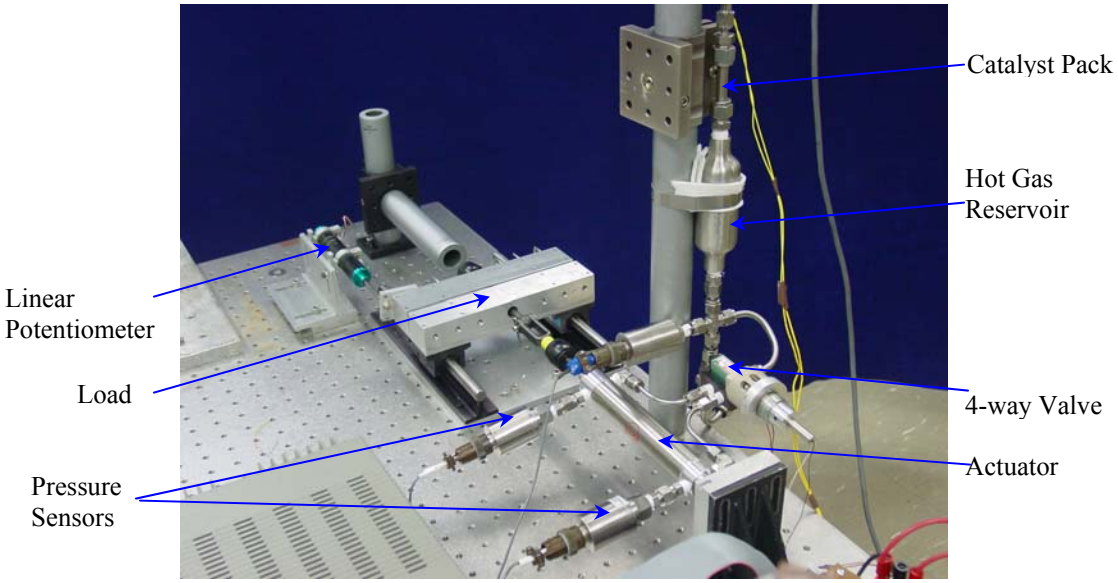

Fig 4-1c. Experimental setup of the centralized configuration

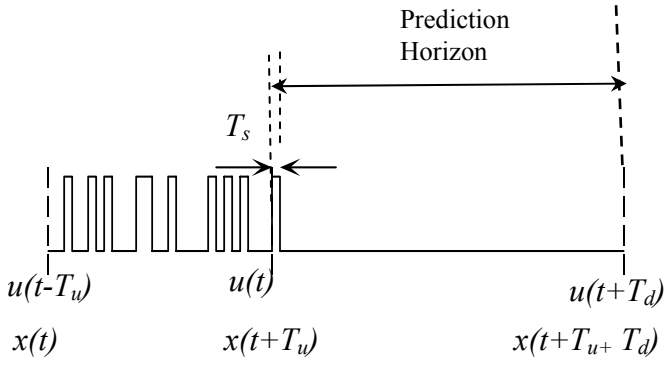

Fig 4-2. Effect of time-delay on the states of the system

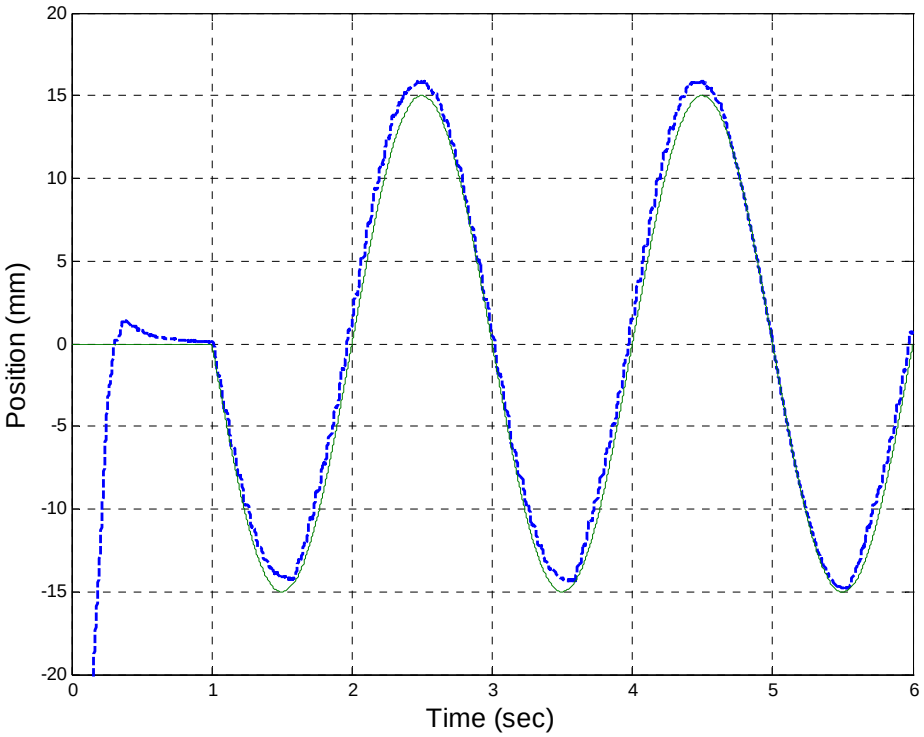

Fig 4-3a. Desired (solid) and actual (dashed) position at 0.5 Hz sinusoidal frequency tracking using pressure sensors

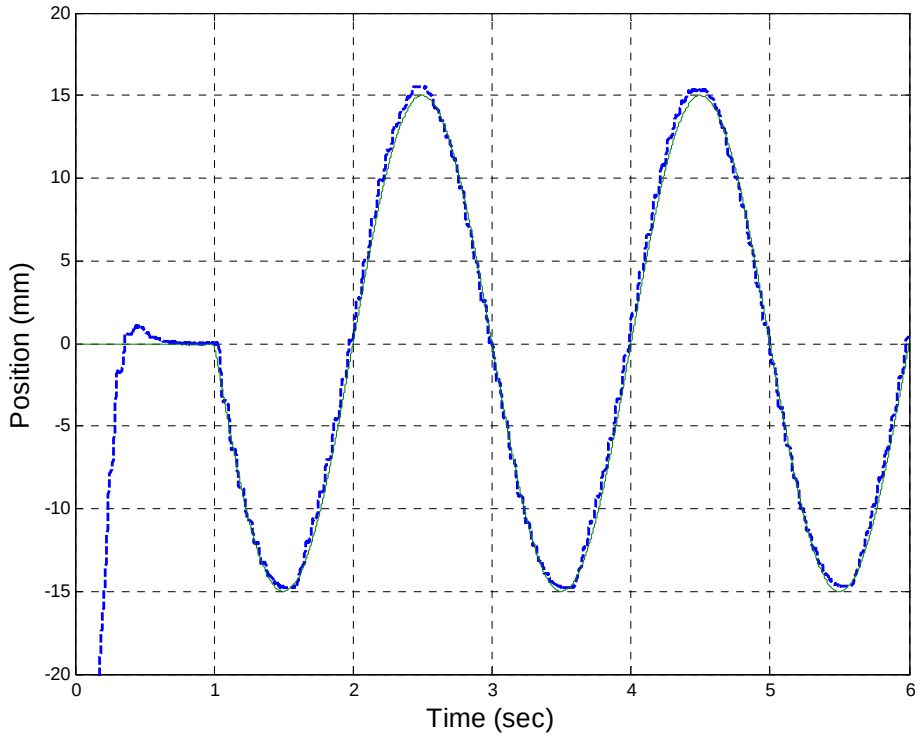

Fig 4-3b. Desired (solid) and actual (dashed) position at 0.5 Hz sinusoidal frequency tracking using pressure observers

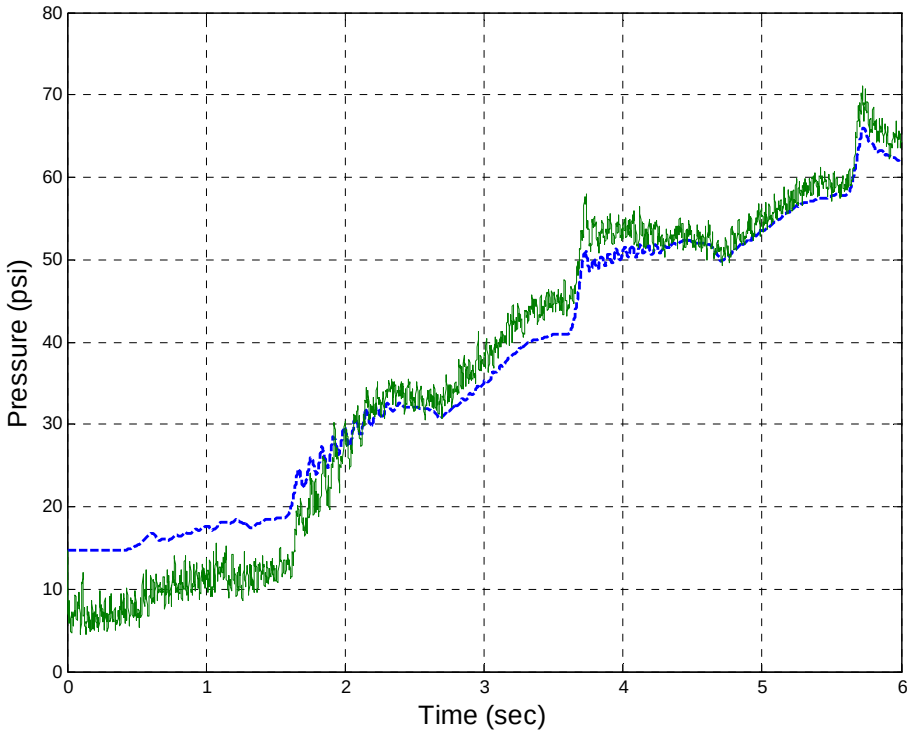

Fig 4-3c. Actual (solid) and observed (dashed) pressure at 0.5 Hz sinusoidal tracking – chamber ‘a’

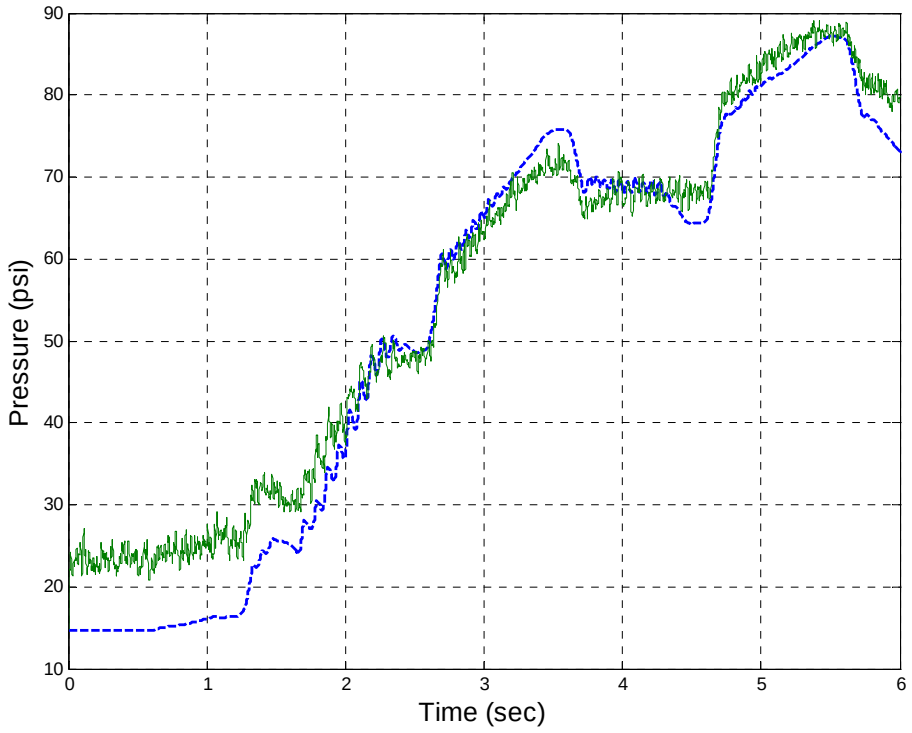

Fig 4-3d. Actual (solid) and observed (dashed) pressure at 0.5 Hz sinusoidal tracking – chamber ‘b’

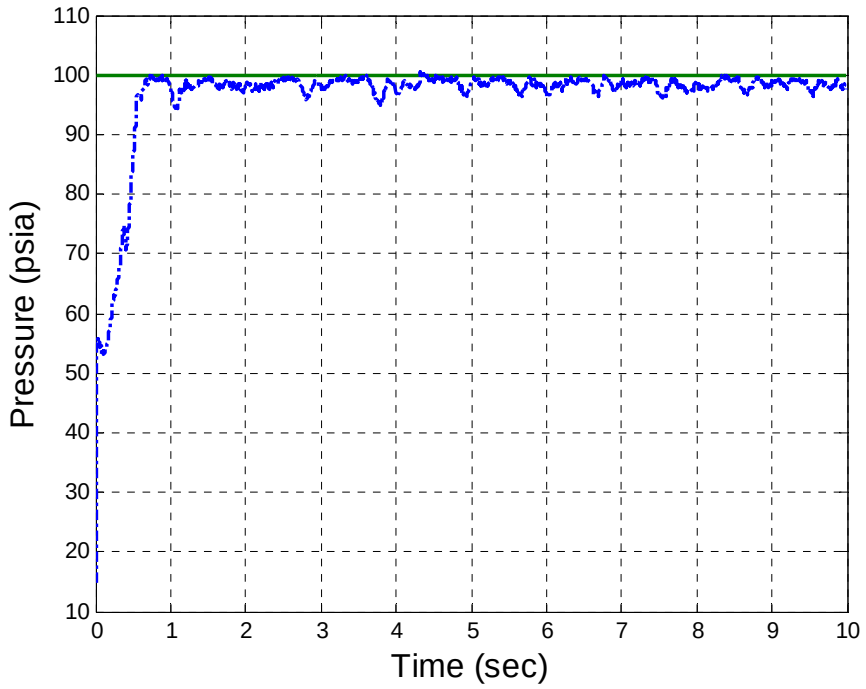

Fig 4-3e. Desired (solid) and actual (dotted) pressure in the hot gas reservoir at 0.5 Hz sinusoidal tracking

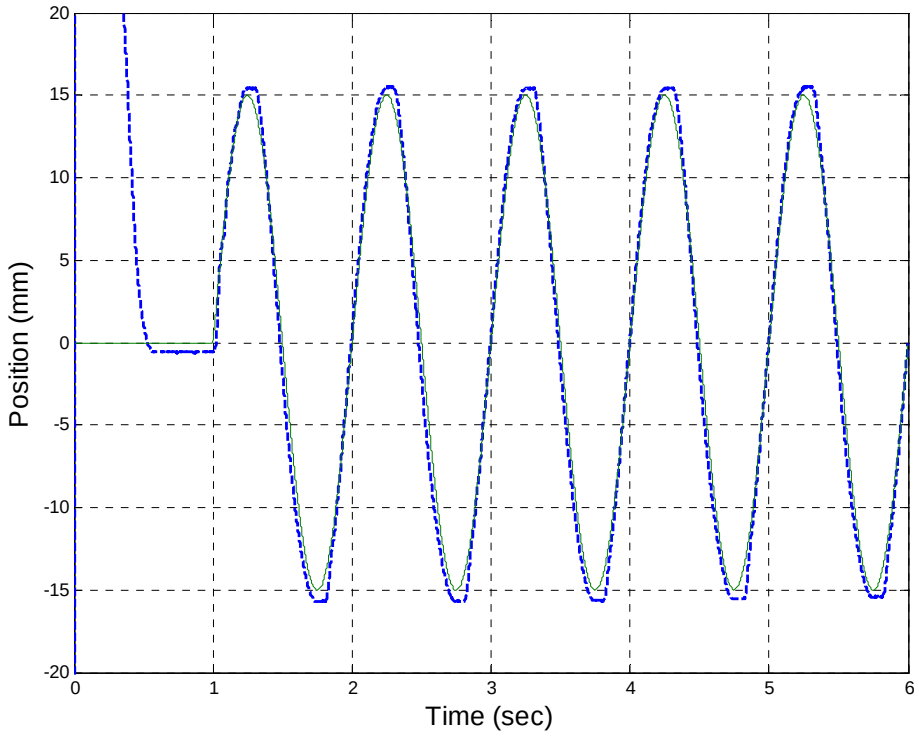

Fig 4-4a. Desired (solid) and actual (dashed) position at 1 Hz sinusoidal frequency tracking using pressure sensors

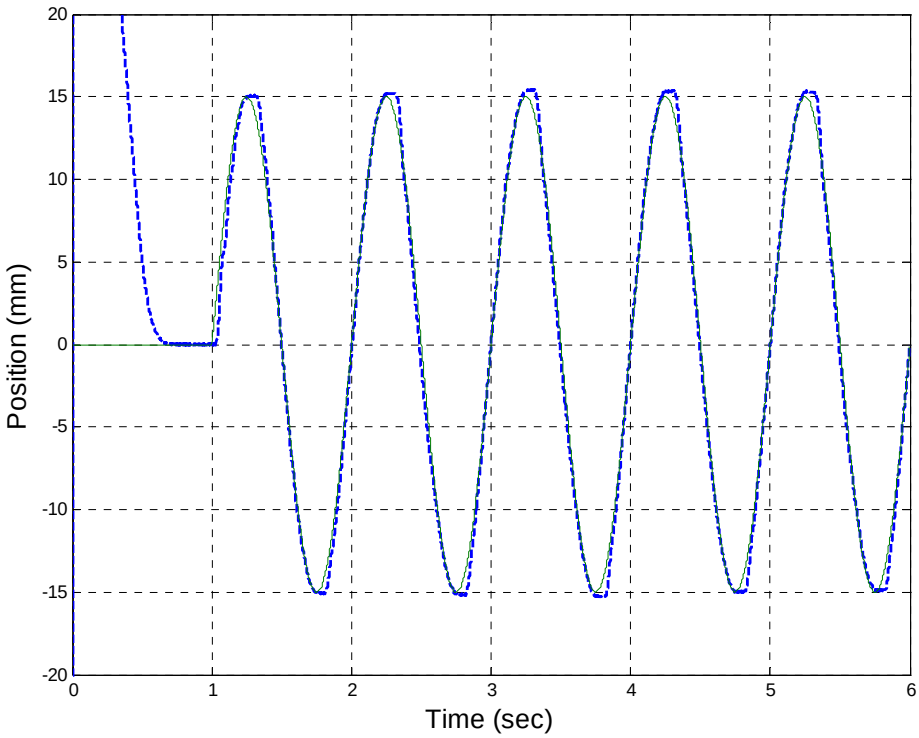

Fig 4-4b. Desired (solid) and actual (dashed) position at 1 Hz sinusoidal frequency tracking using pressure observers

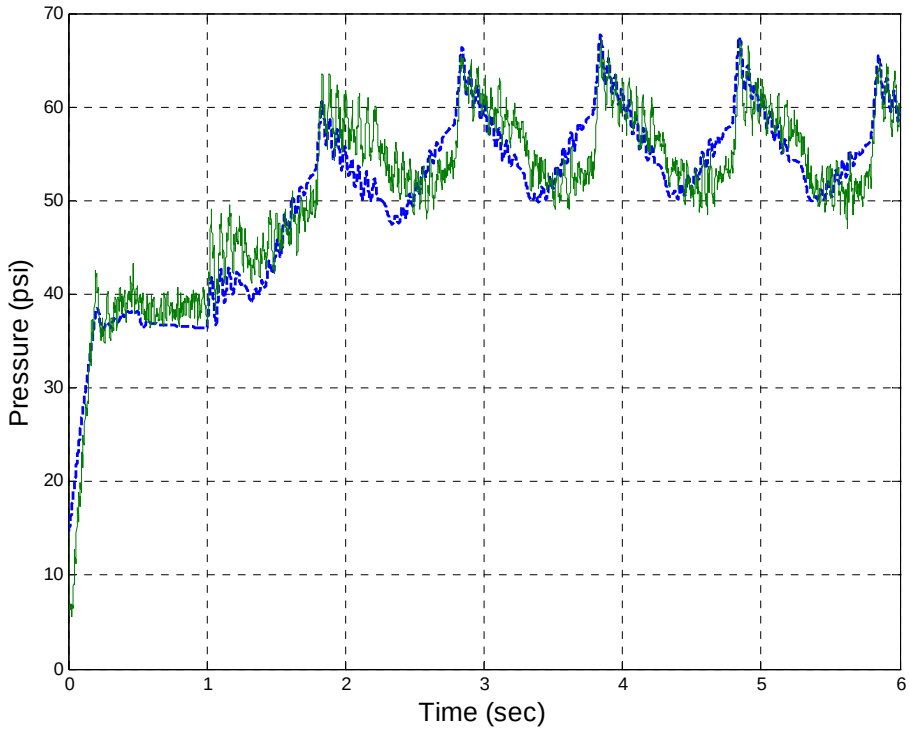

Fig 4-4c. Actual (solid) and observed (dashed) pressure at 1 Hz sinusoidal tracking – chamber ‘a’

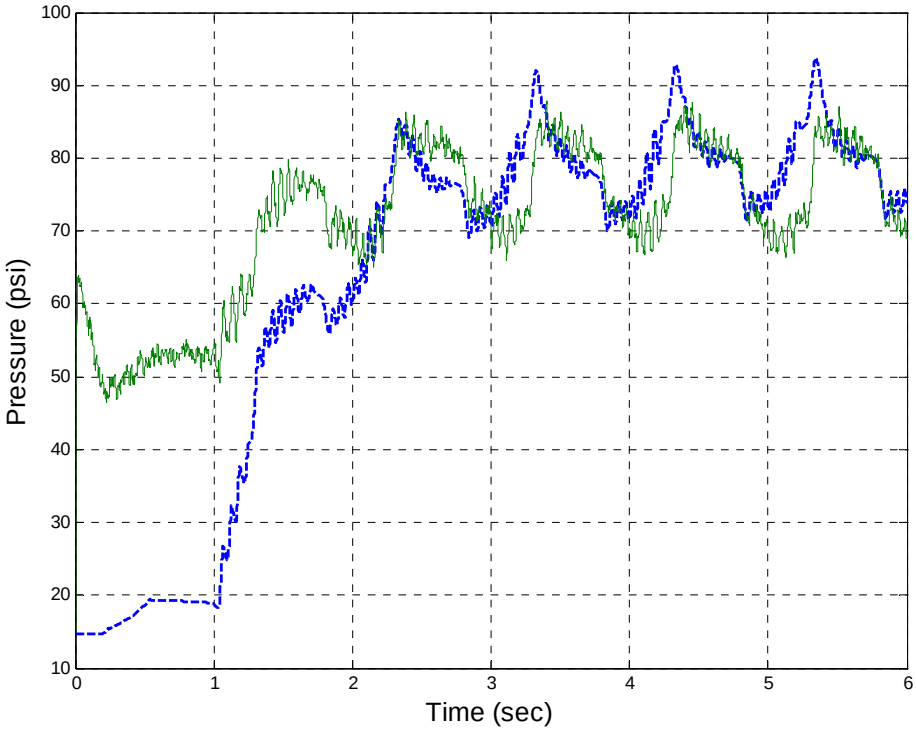

Fig 4-4d. Actual (solid) and observed (dashed) pressure at 1 Hz sinusoidal tracking – chamber ‘b’

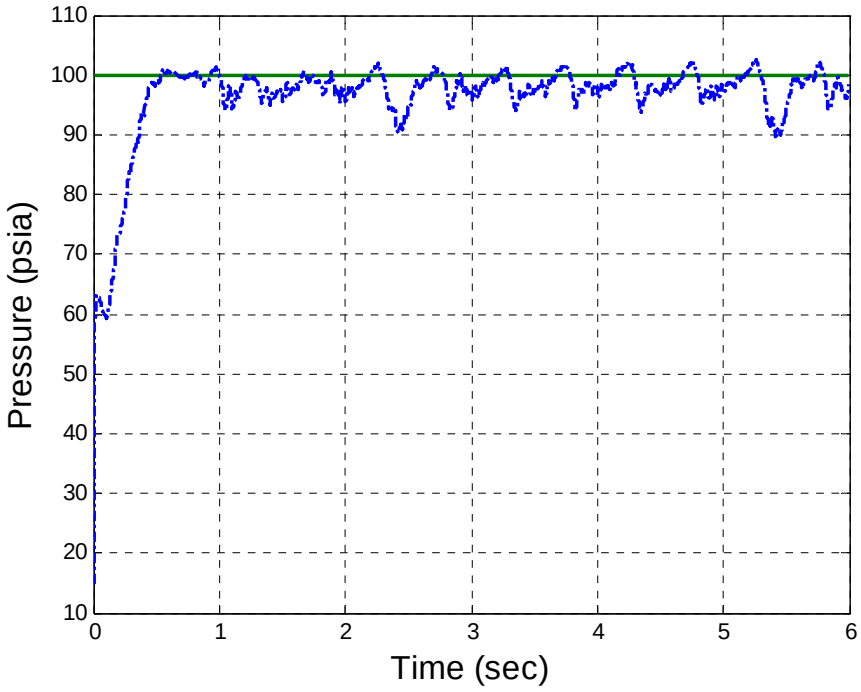

Fig 4-4e. Desired (solid) and actual (dotted) pressure in the hot gas reservoir at 1 Hz sinusoidal tracking

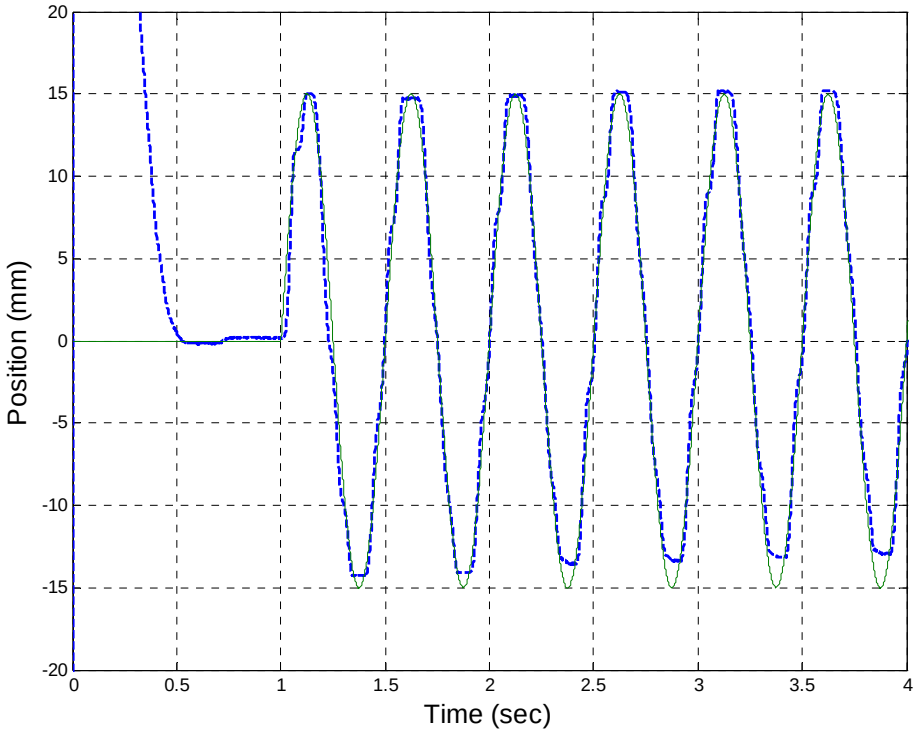

Fig 4-5a. Desired (solid) and actual (dashed) position at 2 Hz sinusoidal frequency tracking using pressure sensors

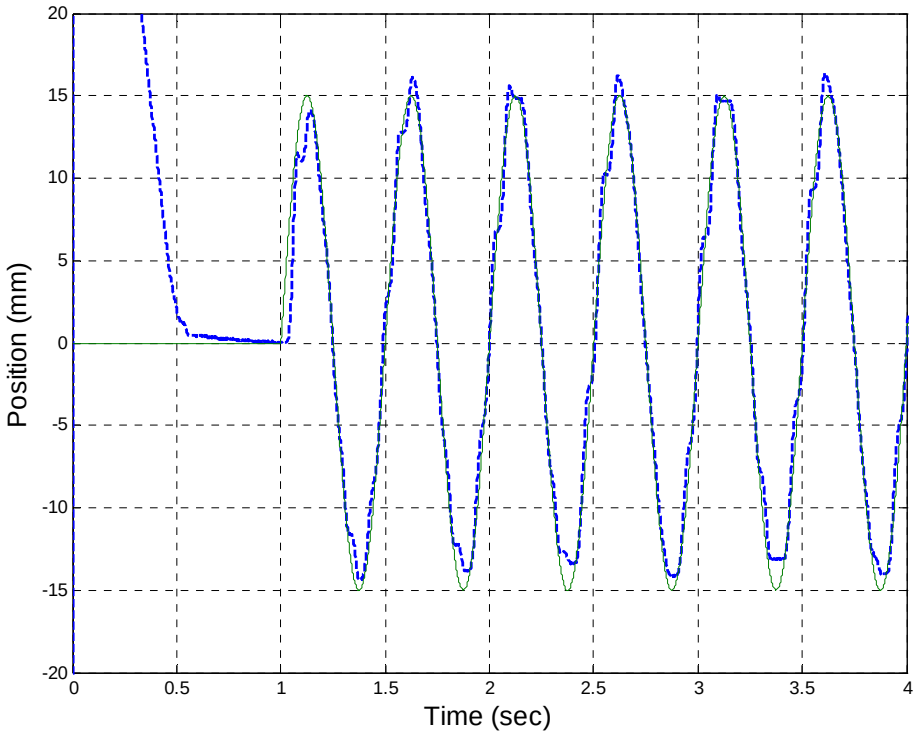

Fig 4-5b. Desired (solid) and actual (dashed) position at 2 Hz sinusoidal frequency tracking using pressure observers

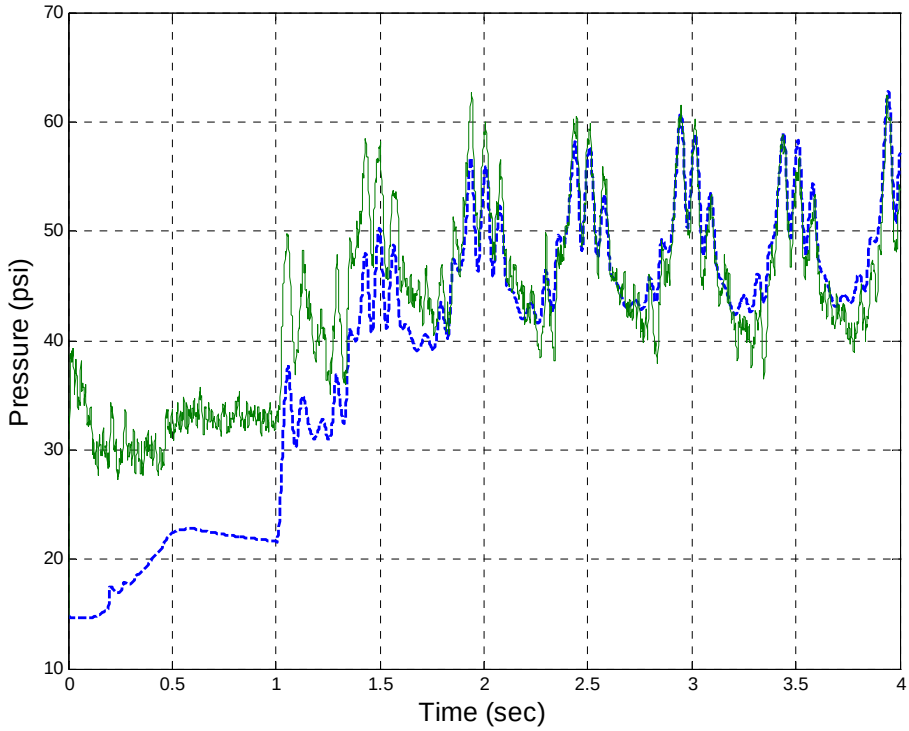

Fig 4-5c. Actual (solid) and observed (dashed) pressure at 2 Hz sinusoidal tracking – chamber ‘a’

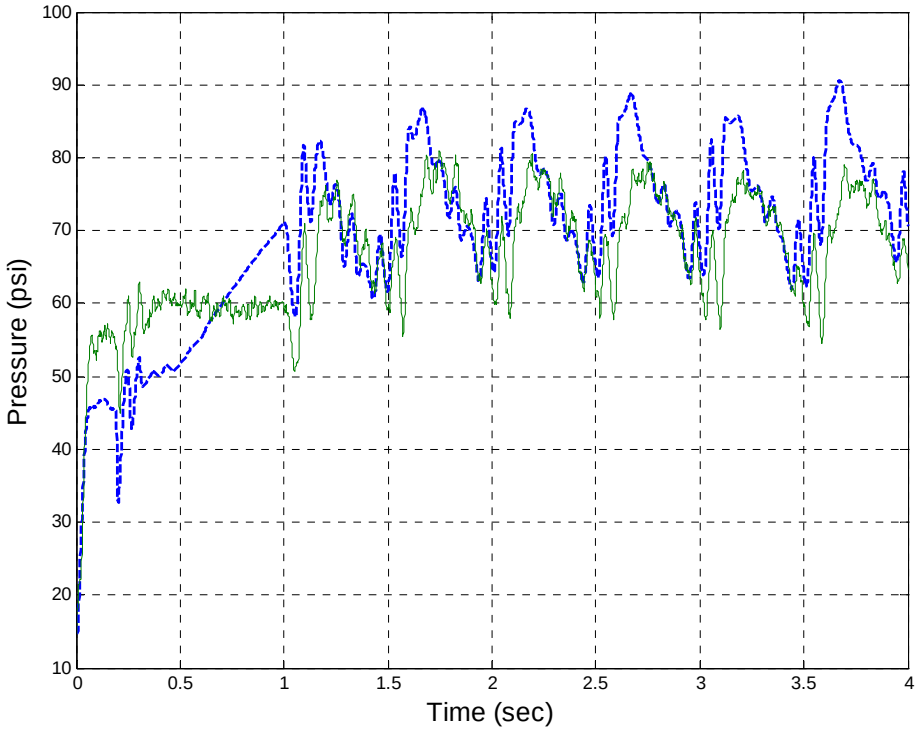

Fig 4-5d. Actual (solid) and observed (dashed) pressure at 2 Hz sinusoidal tracking – chamber ‘b’

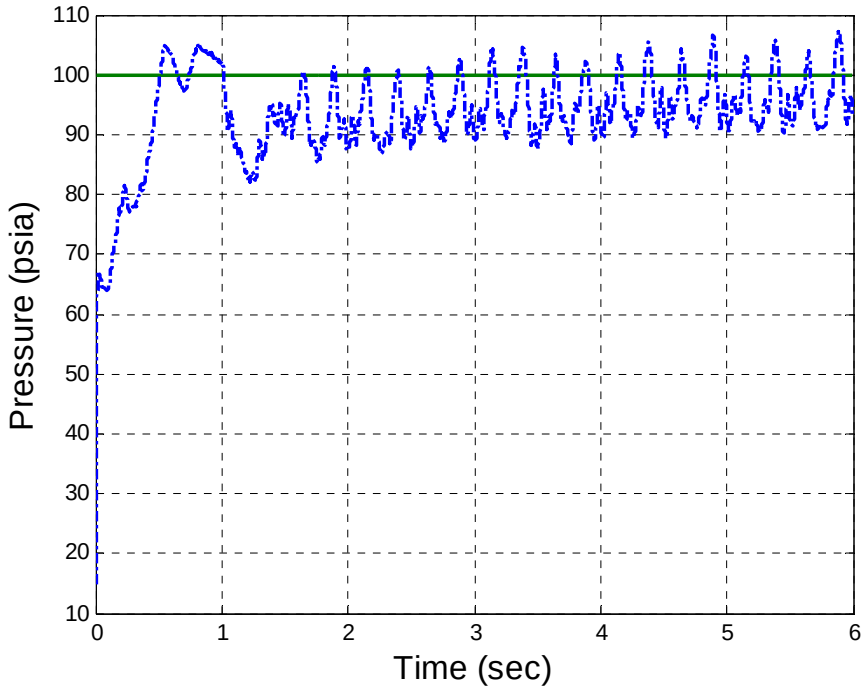

Fig 4-5e. Desired (solid) and actual (dotted) pressure in the hot gas reservoir at 2 Hz sinusoidal tracking

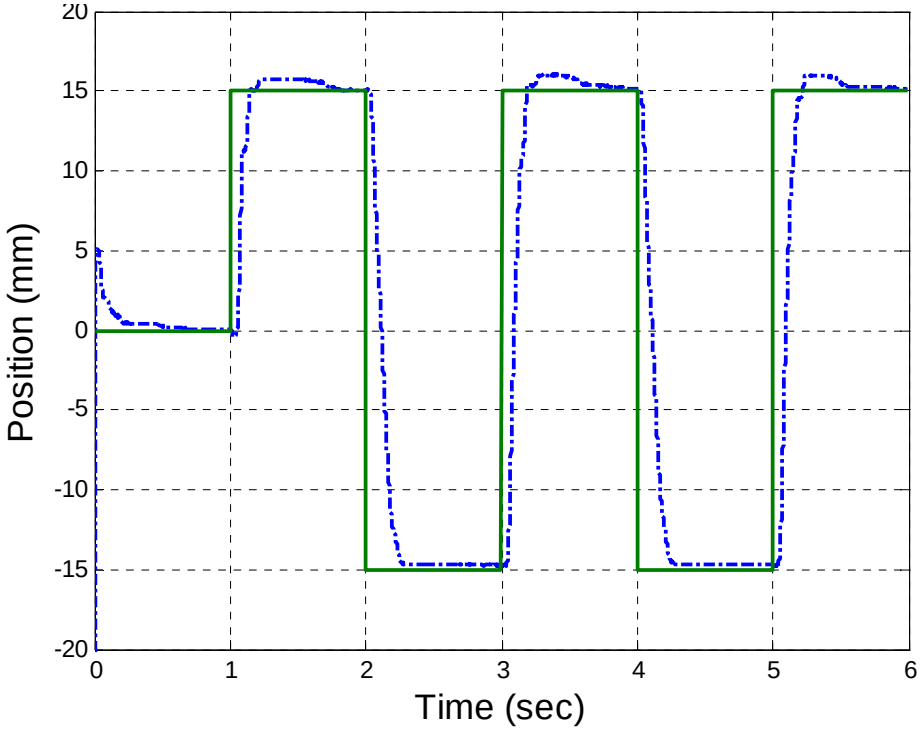

Fig 4-6a. Desired (solid) and actual (dashed) position at 0.5 Hz square-wave frequency tracking using pressure sensors

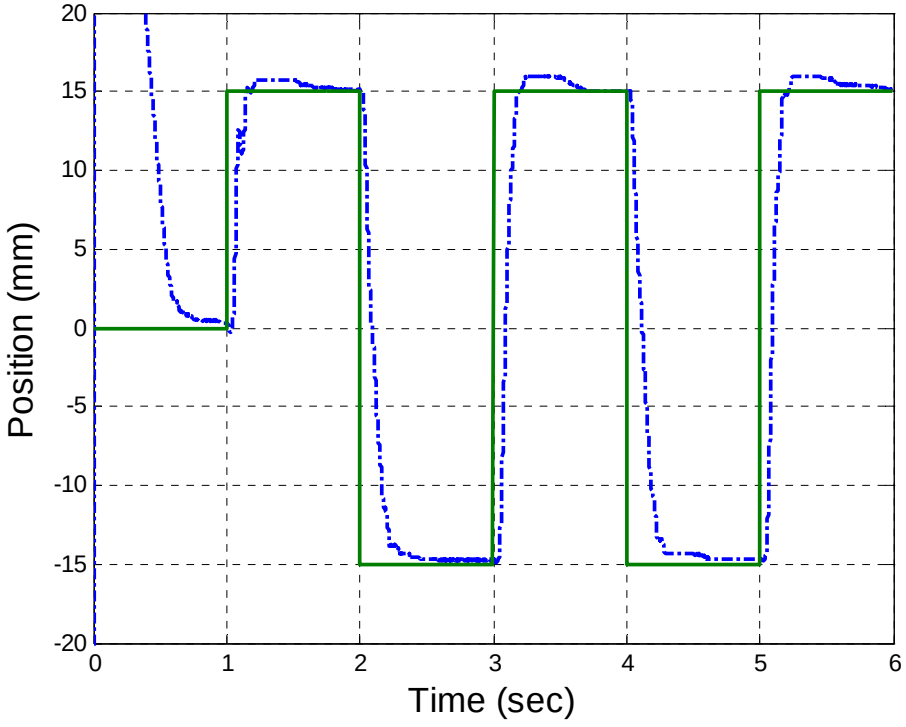

Fig 4-6b. Desired (solid) and actual (dashed) position at 0.5 Hz square-wave frequency tracking using pressure observers

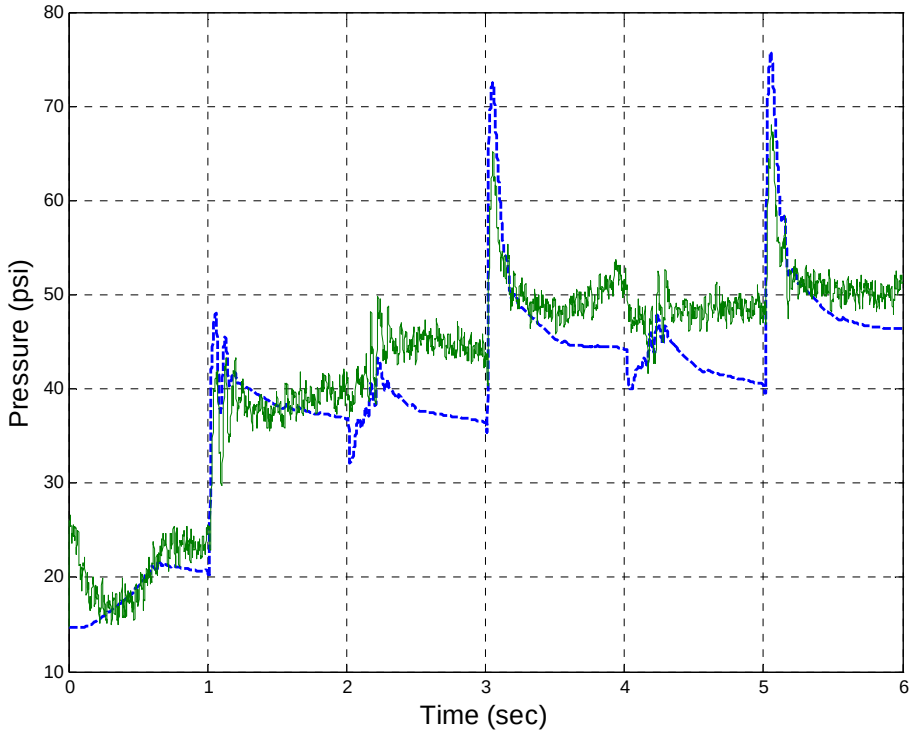

Fig 4-6c. Actual (solid) and observed (dashed) pressure at 0.5 Hz square-wave tracking – chamber 'a'

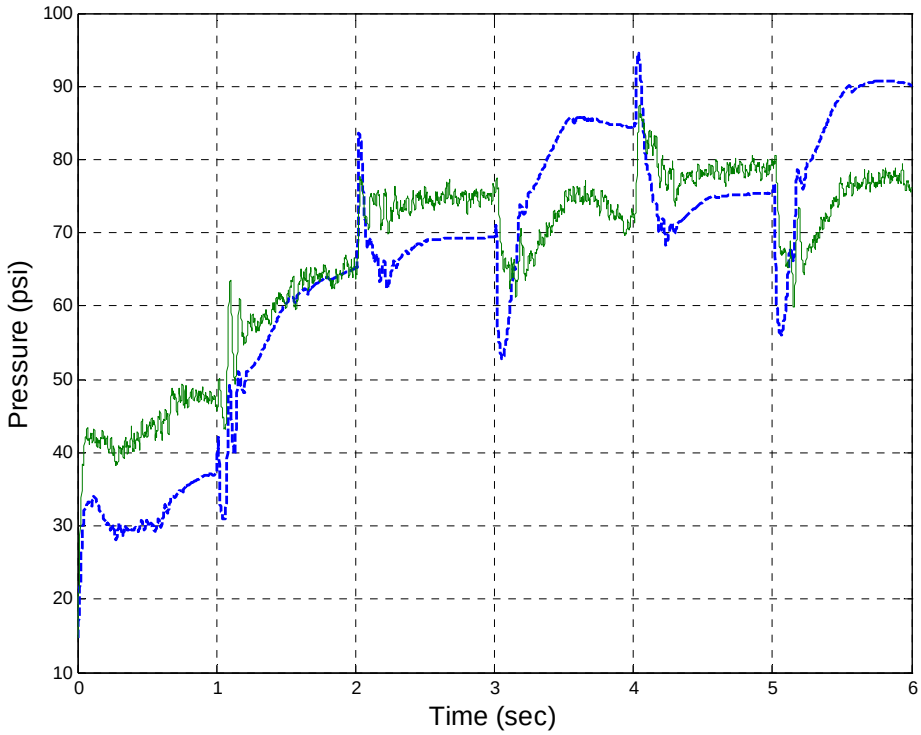

Fig 4-6d. Actual (solid) and observed (dashed) pressure at 0.5 Hz square-wave tracking – chamber 'b'

APPENDIX A

MATLAB SIMULINK BLOCKS FOR MANUSCRIPT I

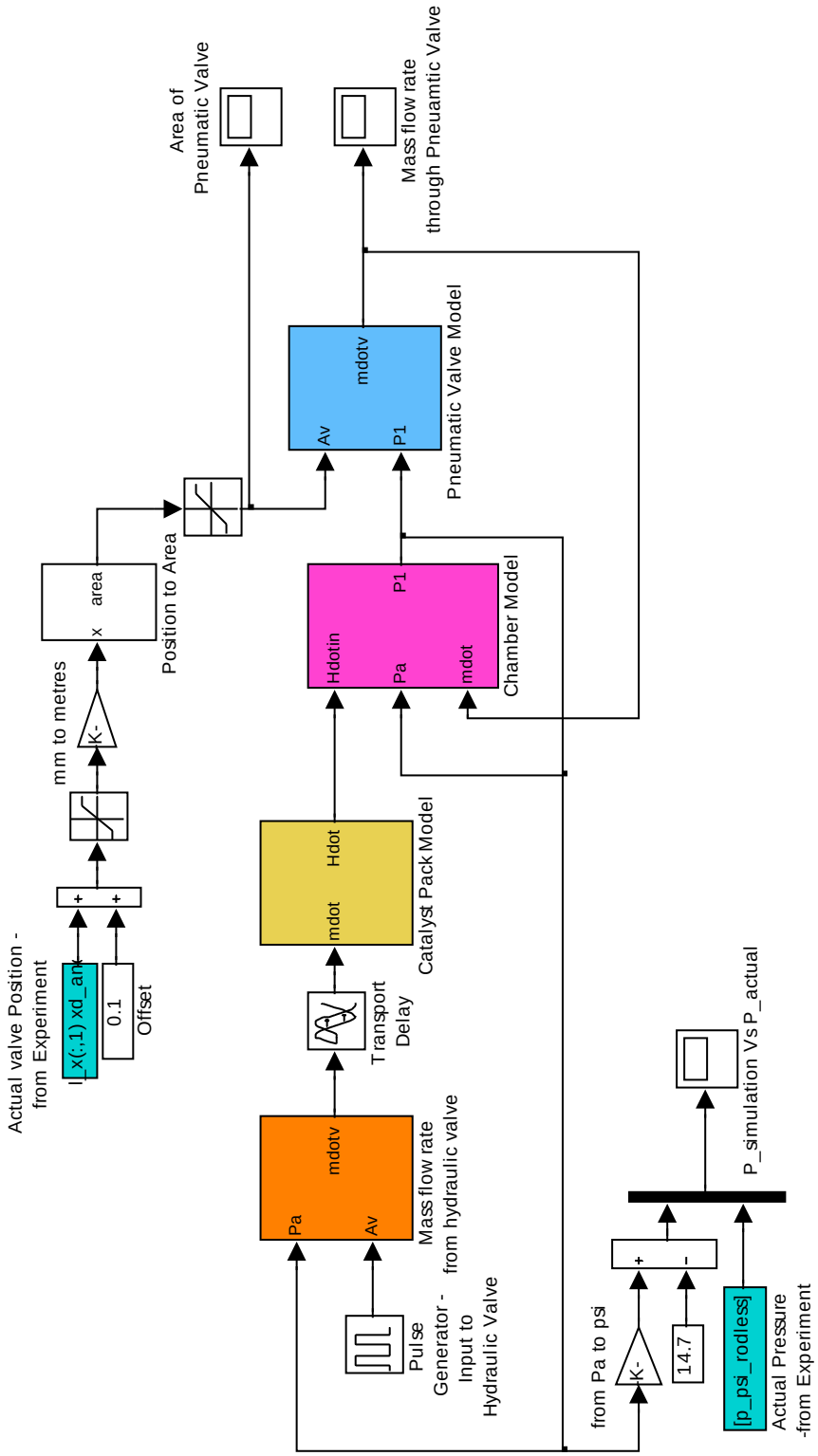

Figure A-1. Block diagram of the Chemofluidic Actuators Model

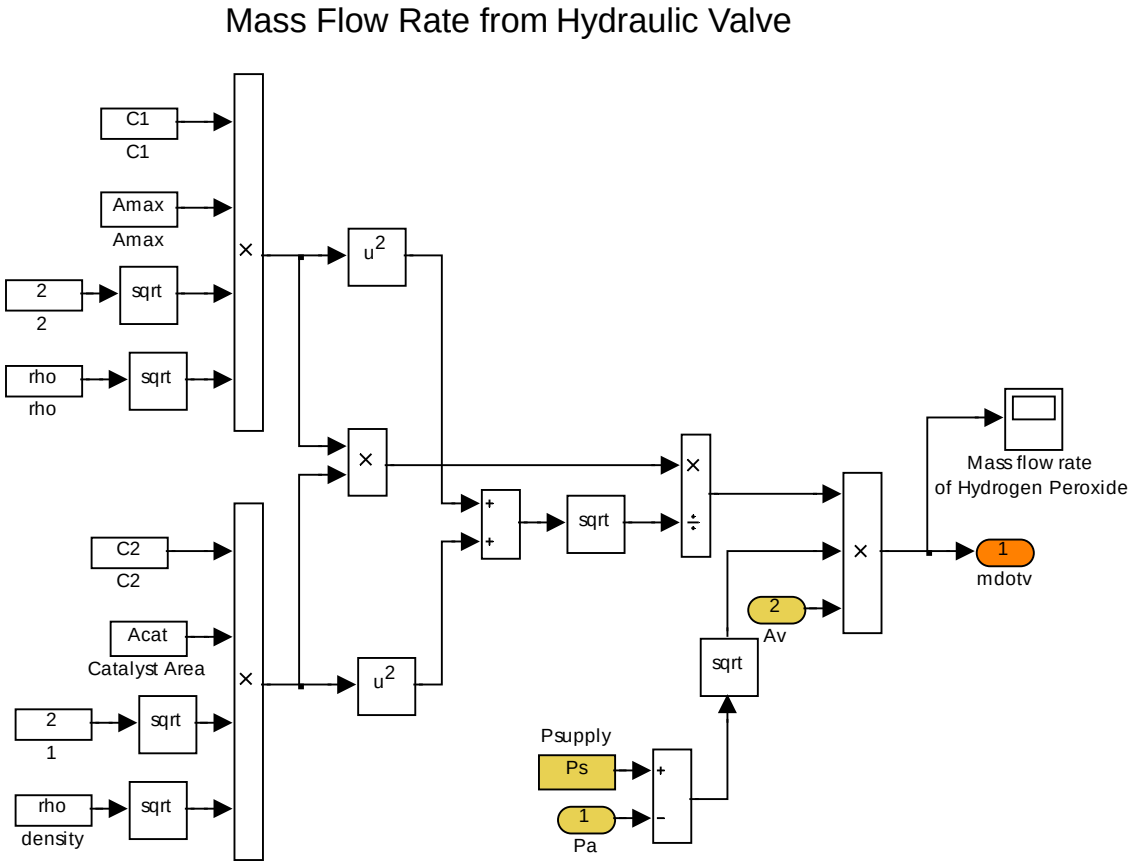

Figure A-2. Block diagram characterizing the dynamics of hydraulic valve and resistance of the catalyst pack

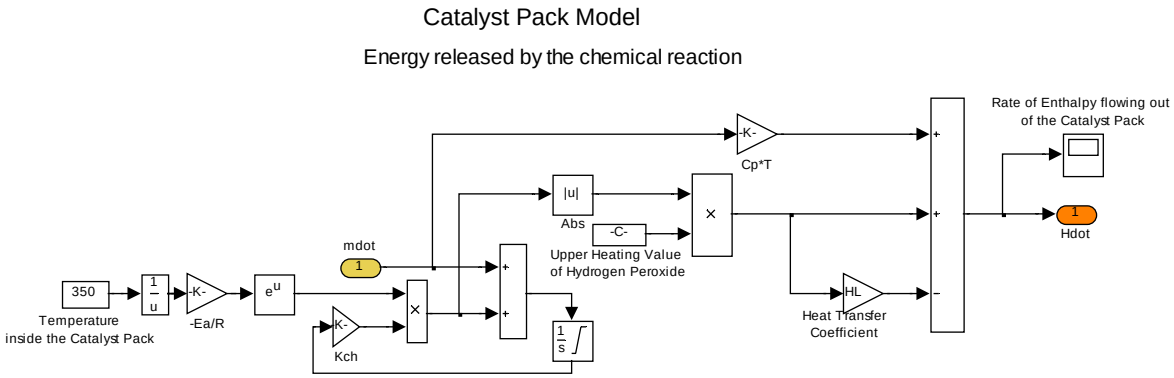

Figure A-3. Block diagram characterizing the decomposition of hydrogen peroxide in the catalyst pack

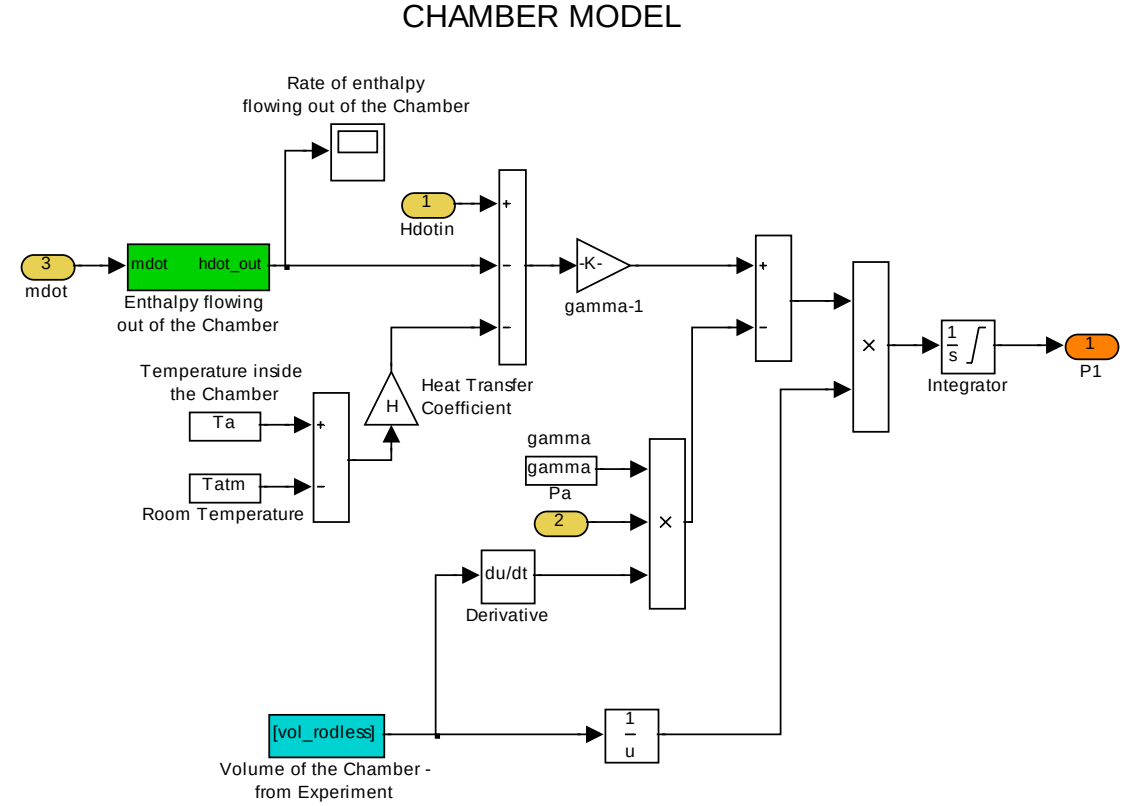

Figure A-4. Block diagram characterizing the dynamics of actuator

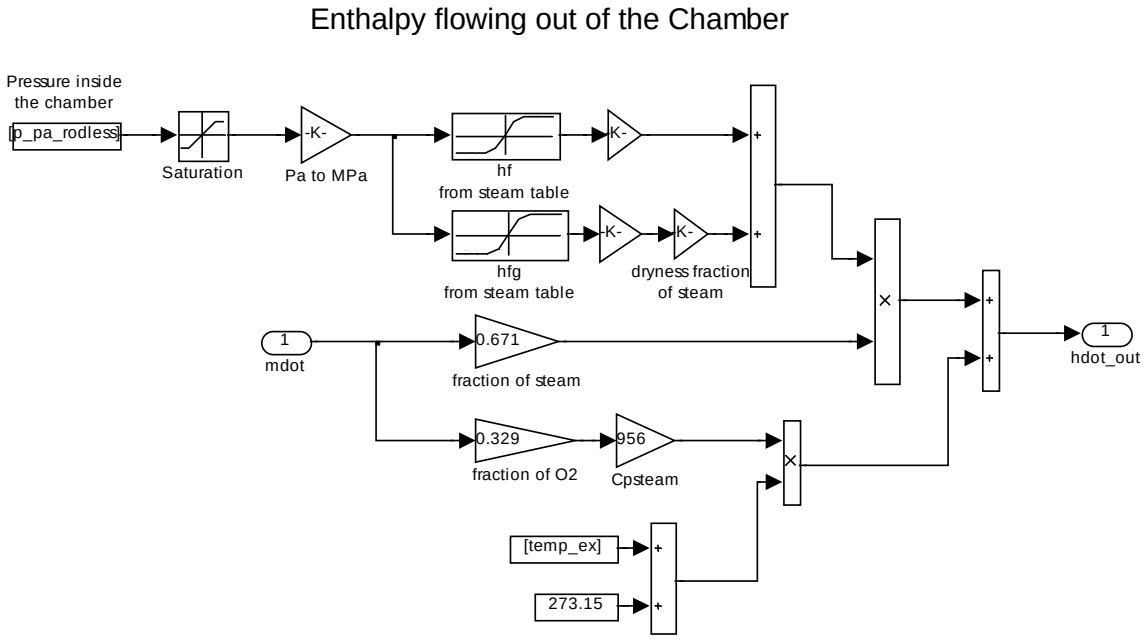

Figure A-5. Block diagram characterizing the rate of enthalpy leaving the chamber as a function of mass flow rate

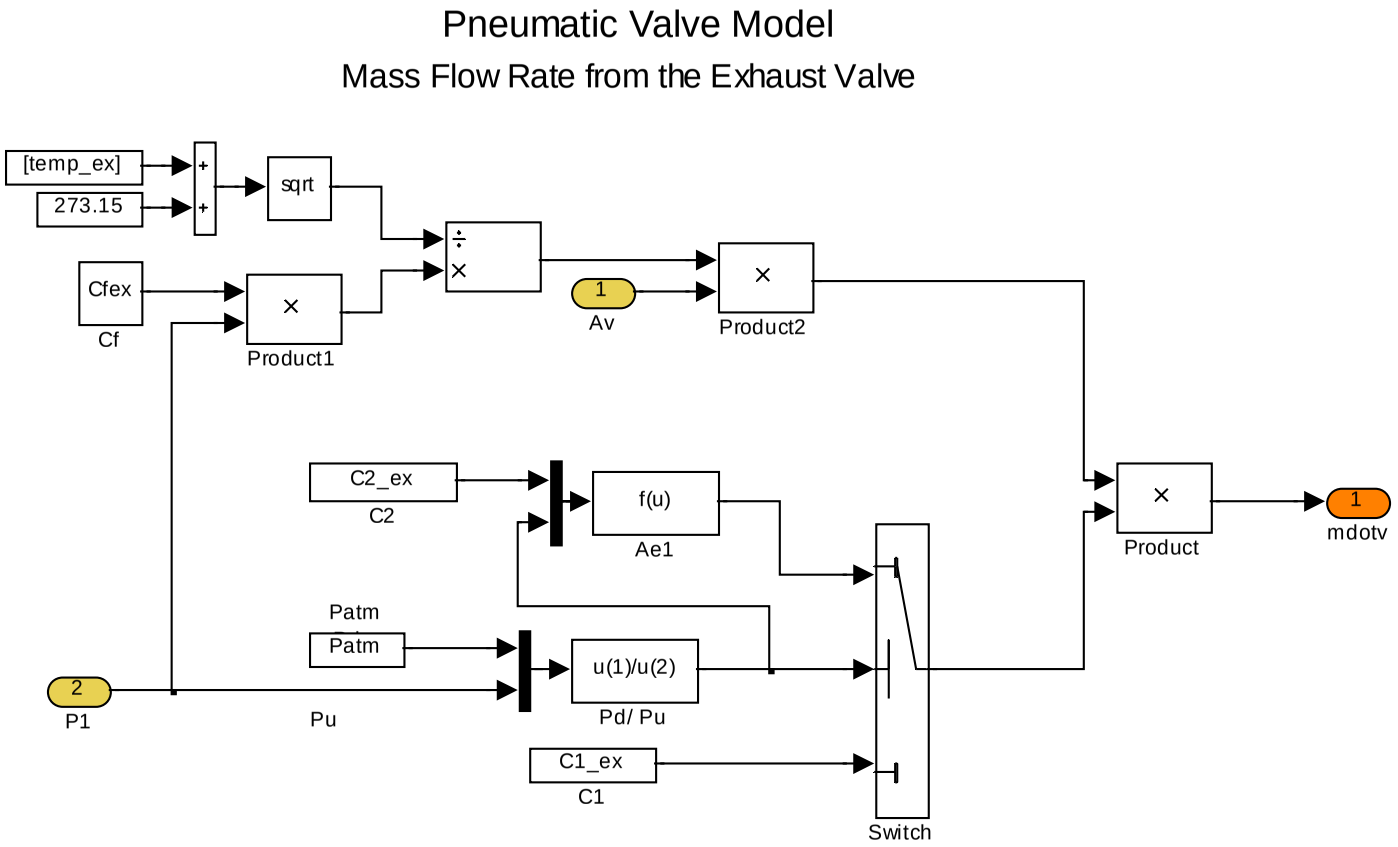

Figure A-6. Block diagram characterizing the dynamics of pneumatic valve

APPENDIX B

MATLAB SIMULINK BLOCKS FOR MANUSCRIPT II

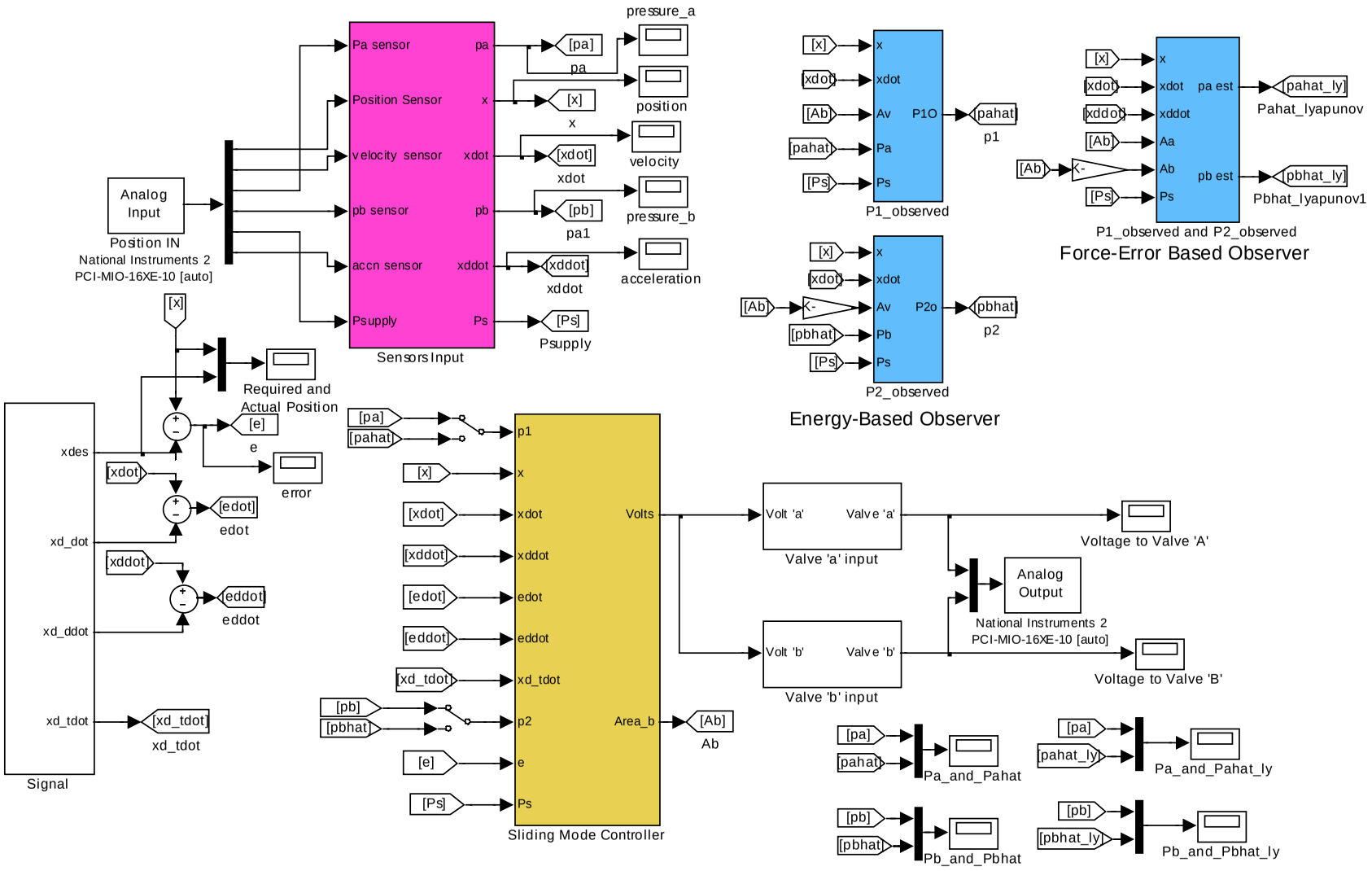

Figure B-1. Block diagram of pressure observers and the controller for pneumatic actuators

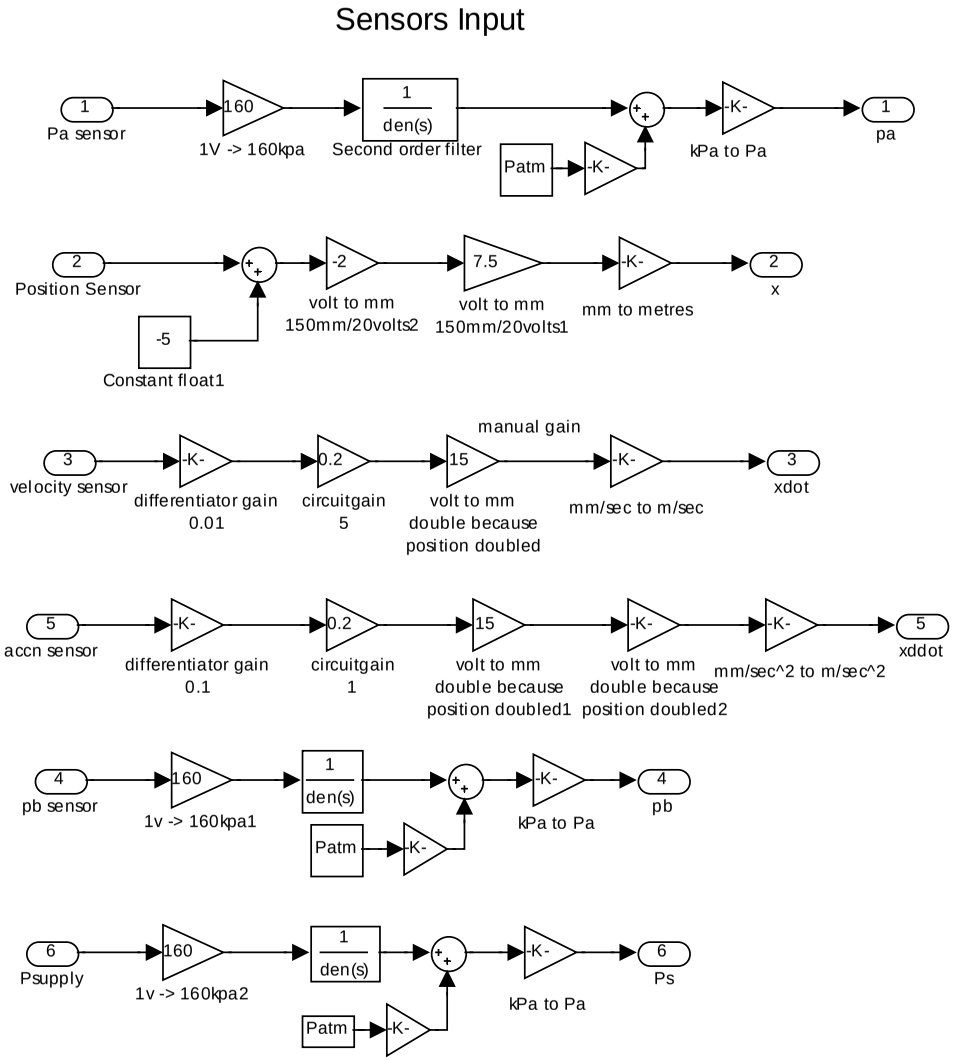

Figure B-2. Block diagram showing the calibration of sensors used in the experiment of manuscript 2

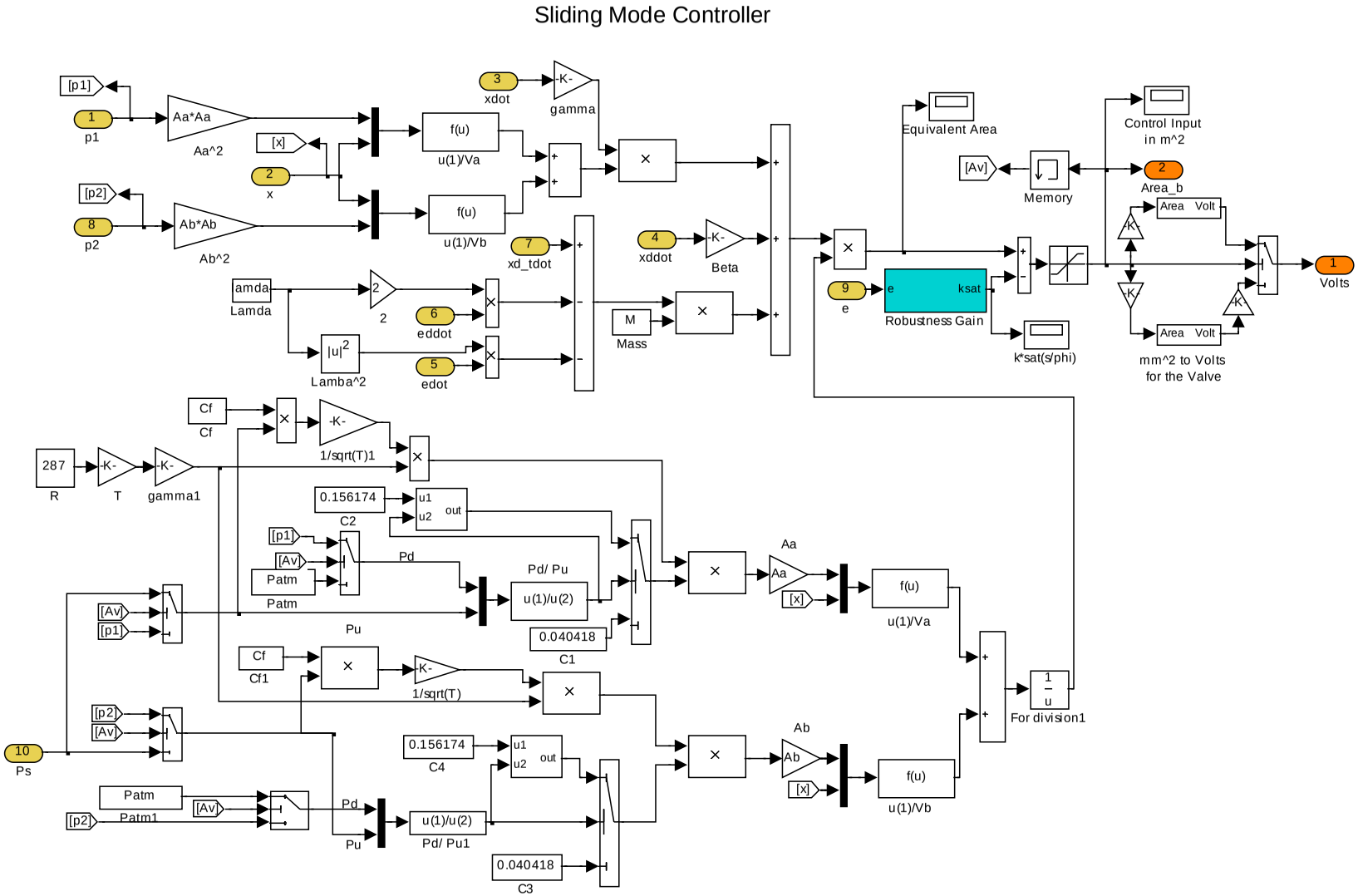

Figure B-3. Block diagram showing the implemented sliding mode controller for pneumatic actuators

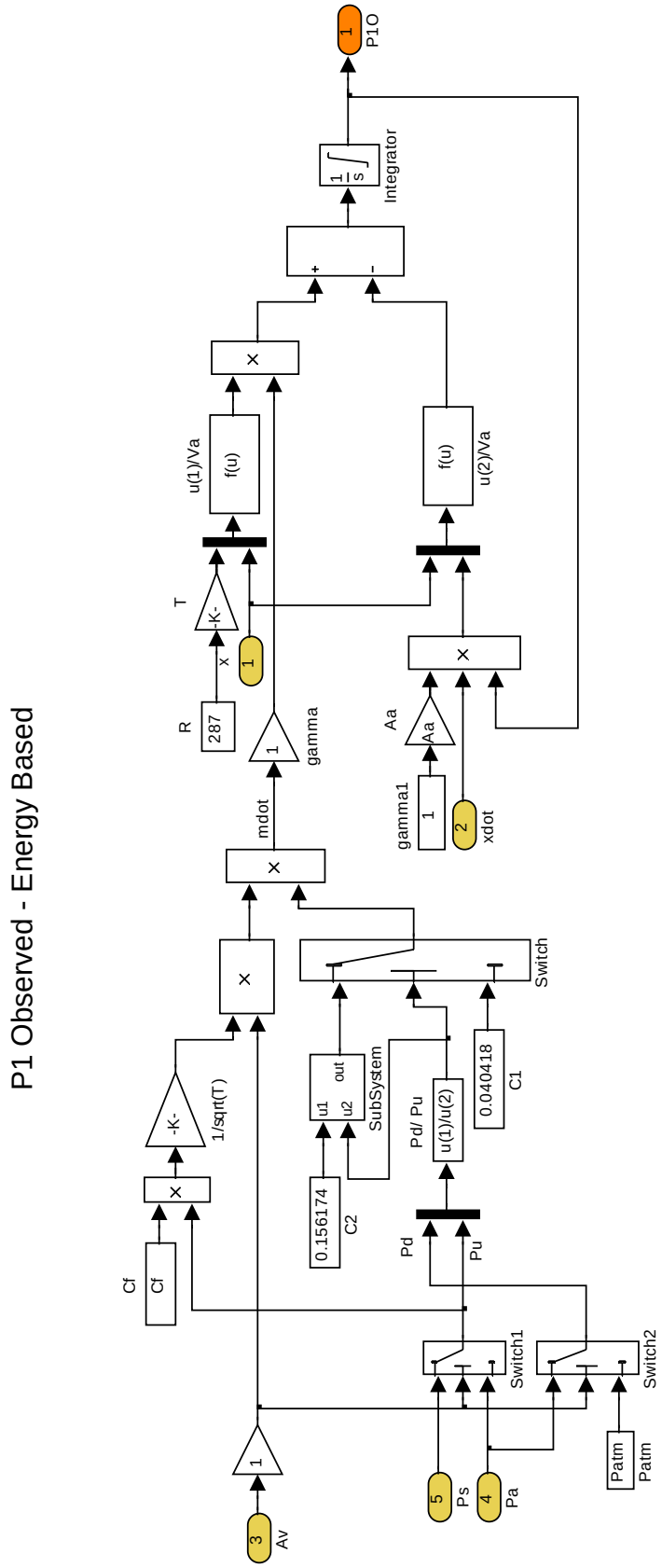

Figure B-4. Block diagram of the energy-based pressure observer for chamber ‘a’

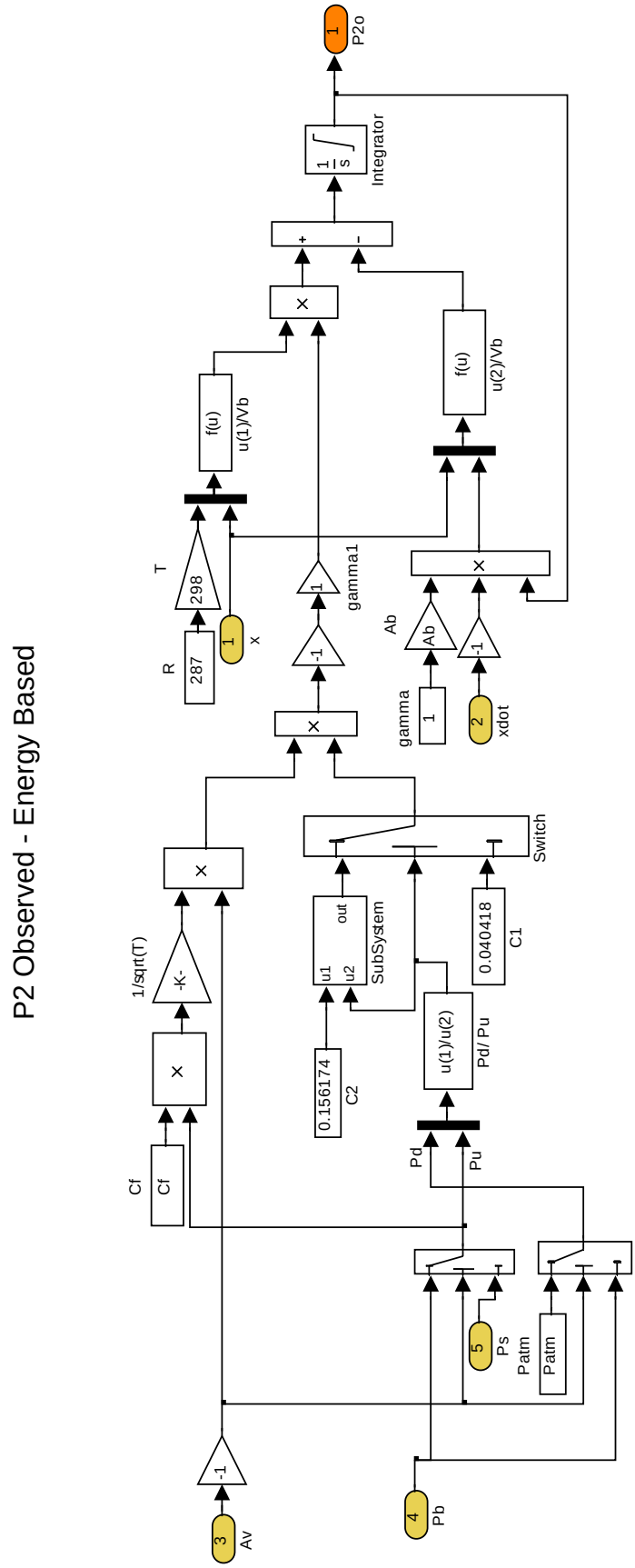

Figure B-5. Block diagram of the energy-based pressure observer for chamber ‘b’

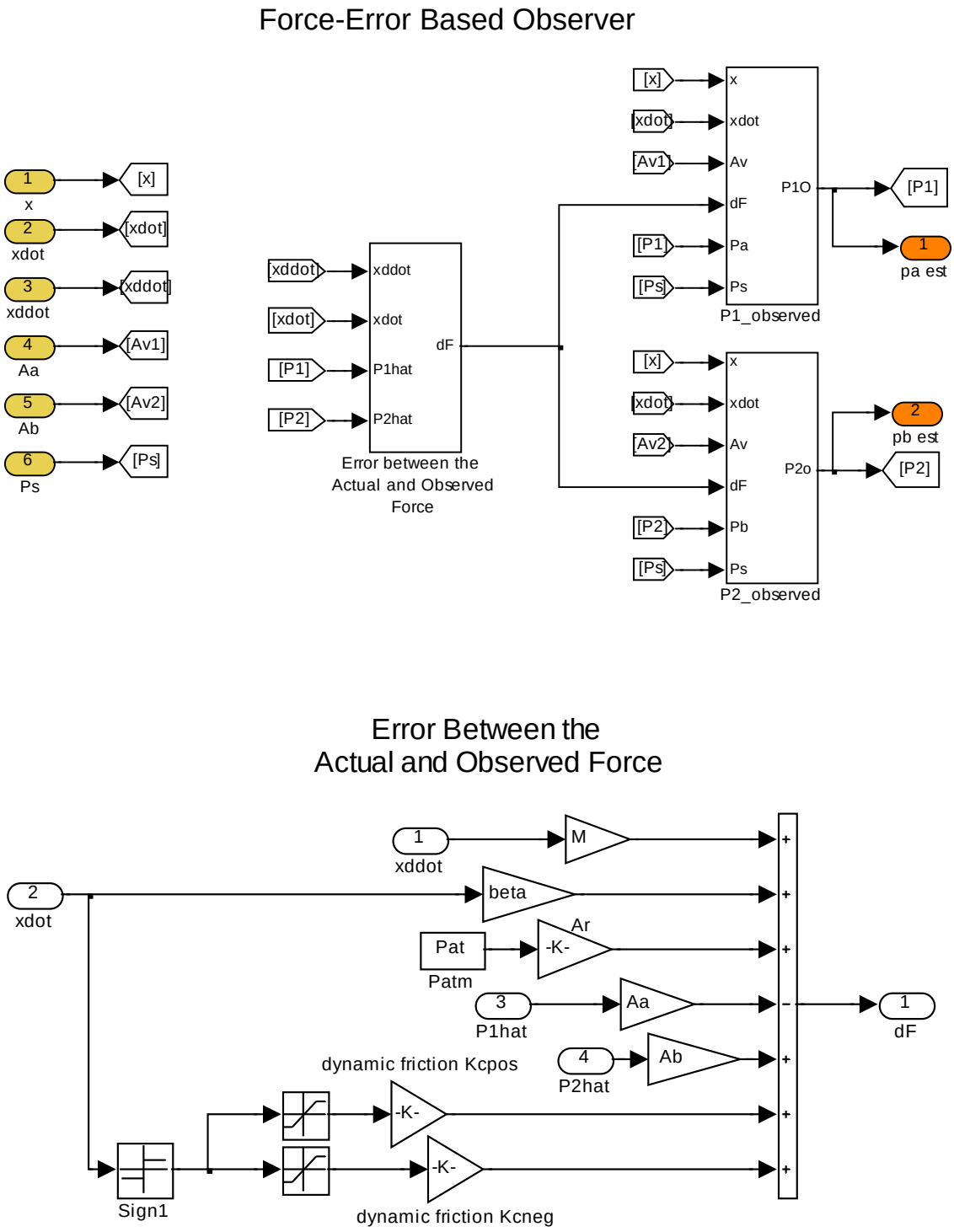

Figure B-6. Block diagram for calculating the error between the observed and actual force

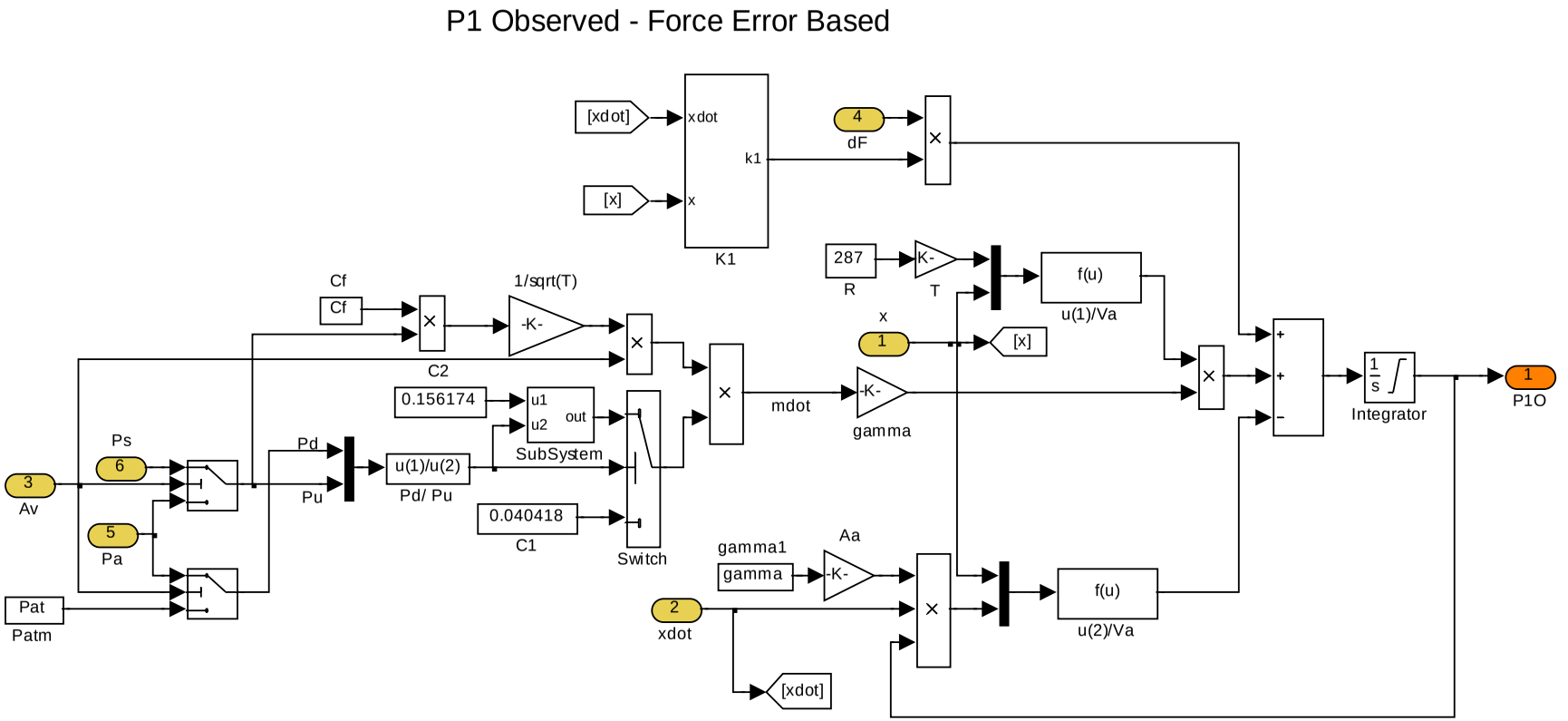

Figure B-7. Block diagram of the force-error based pressure observer for chamber ‘a’

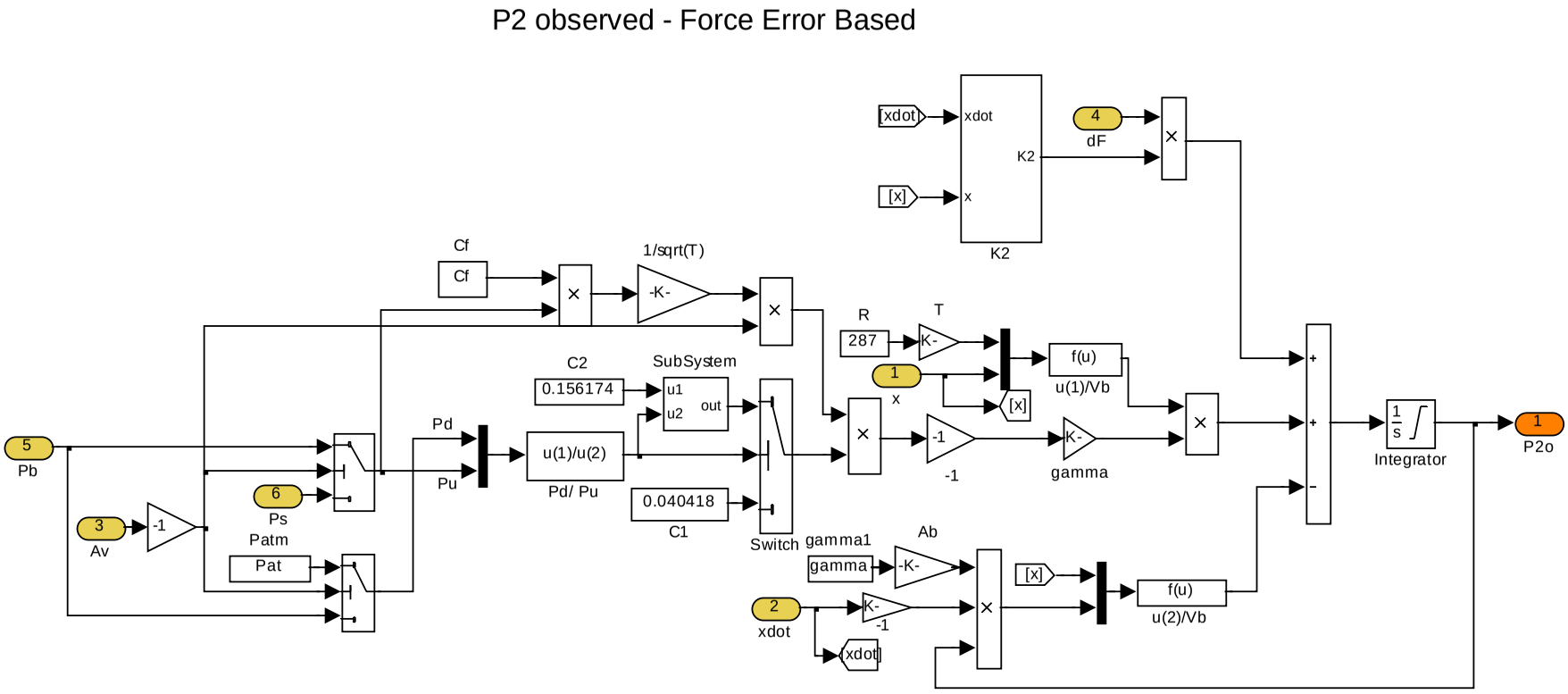

Figure B-8. Block diagram of the force-error based pressure observer for chamber ‘b’

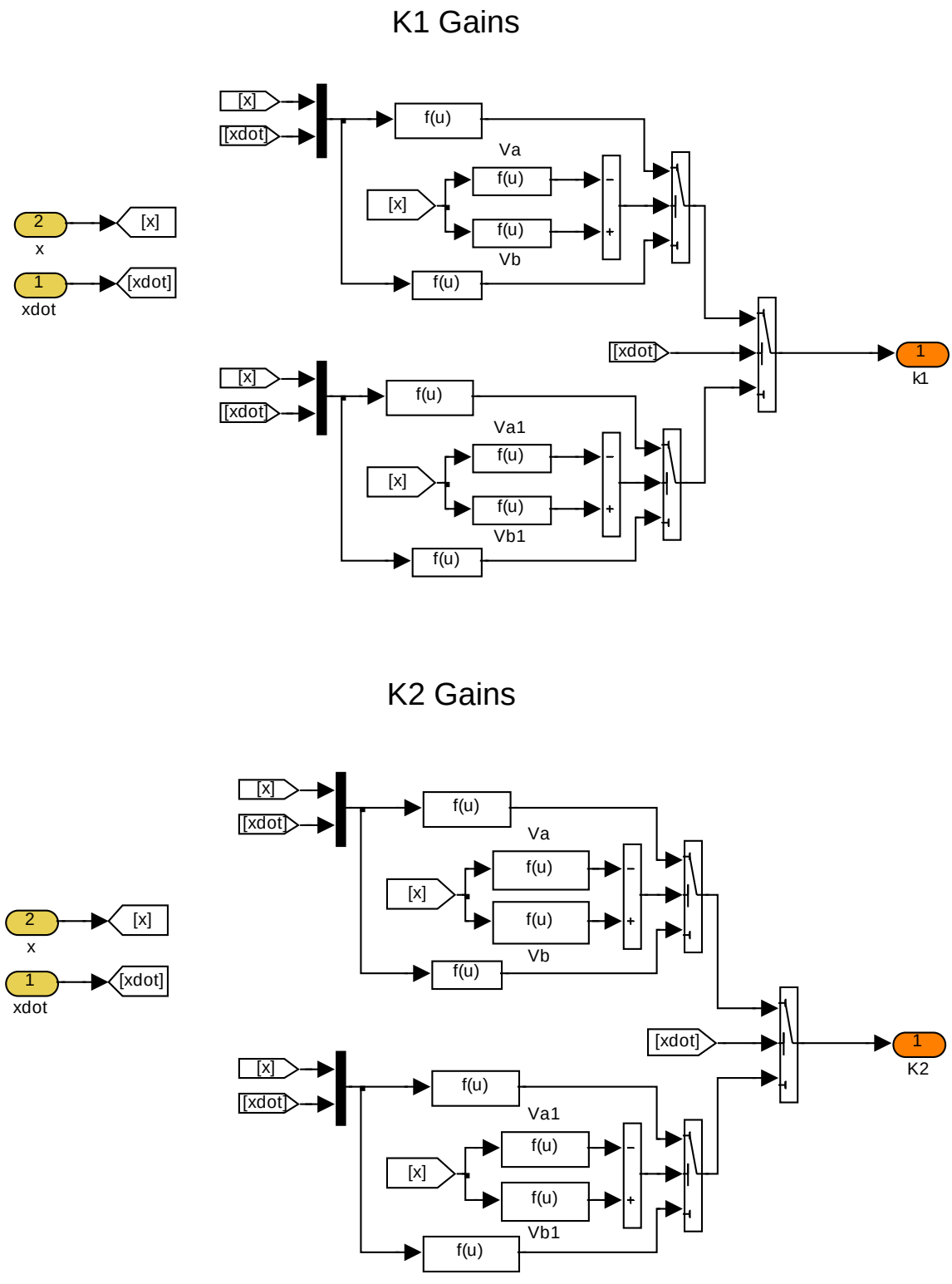

Figure B-9. Block diagram showing the calculation of dynamic gains for the force-error based observer

APPENDIX C

MATLAB SIMULINK BLOCKS FOR MANUSCRIPT III

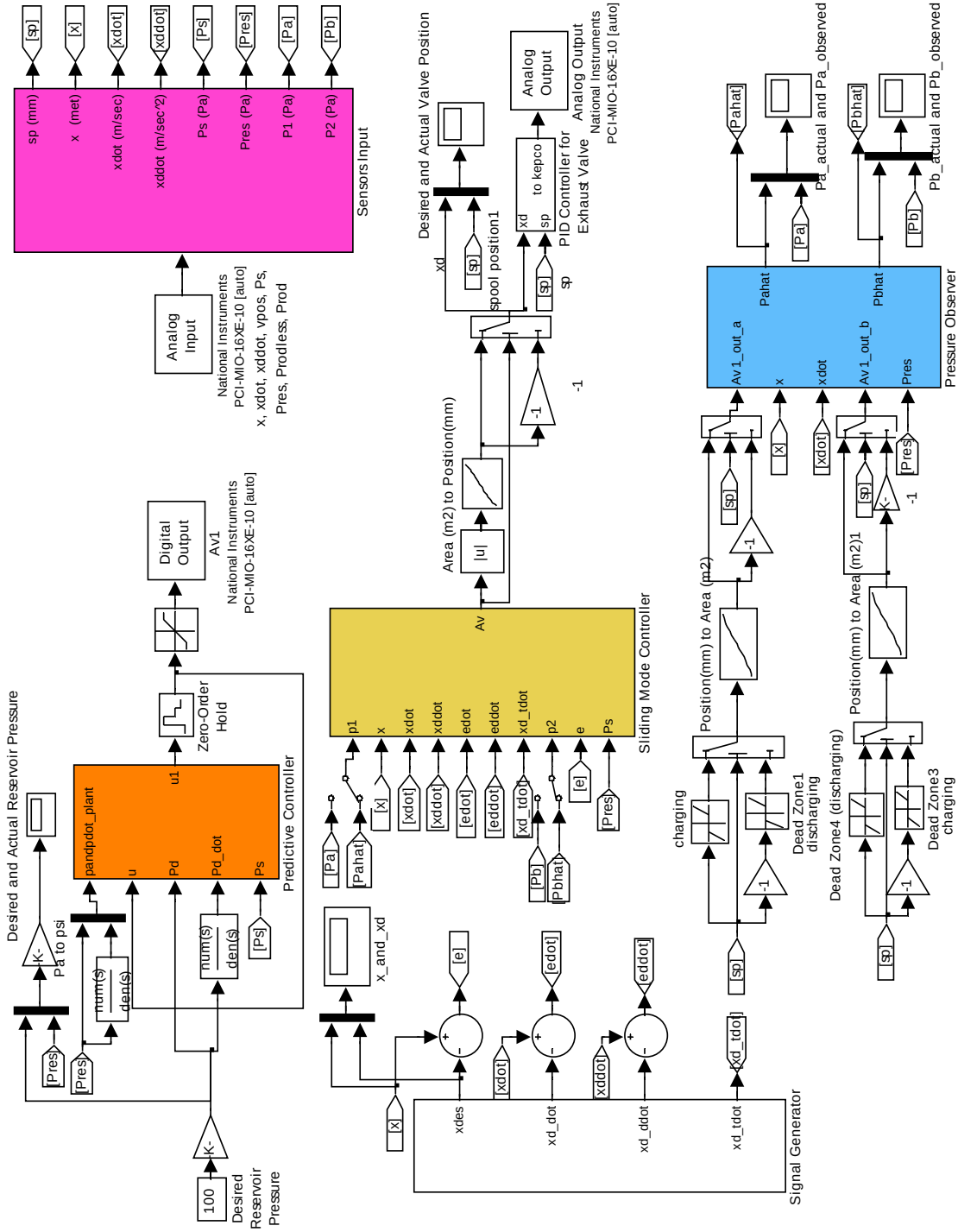

Figure C-1. Block diagram of the observer-based controller for chemofluidic actuators

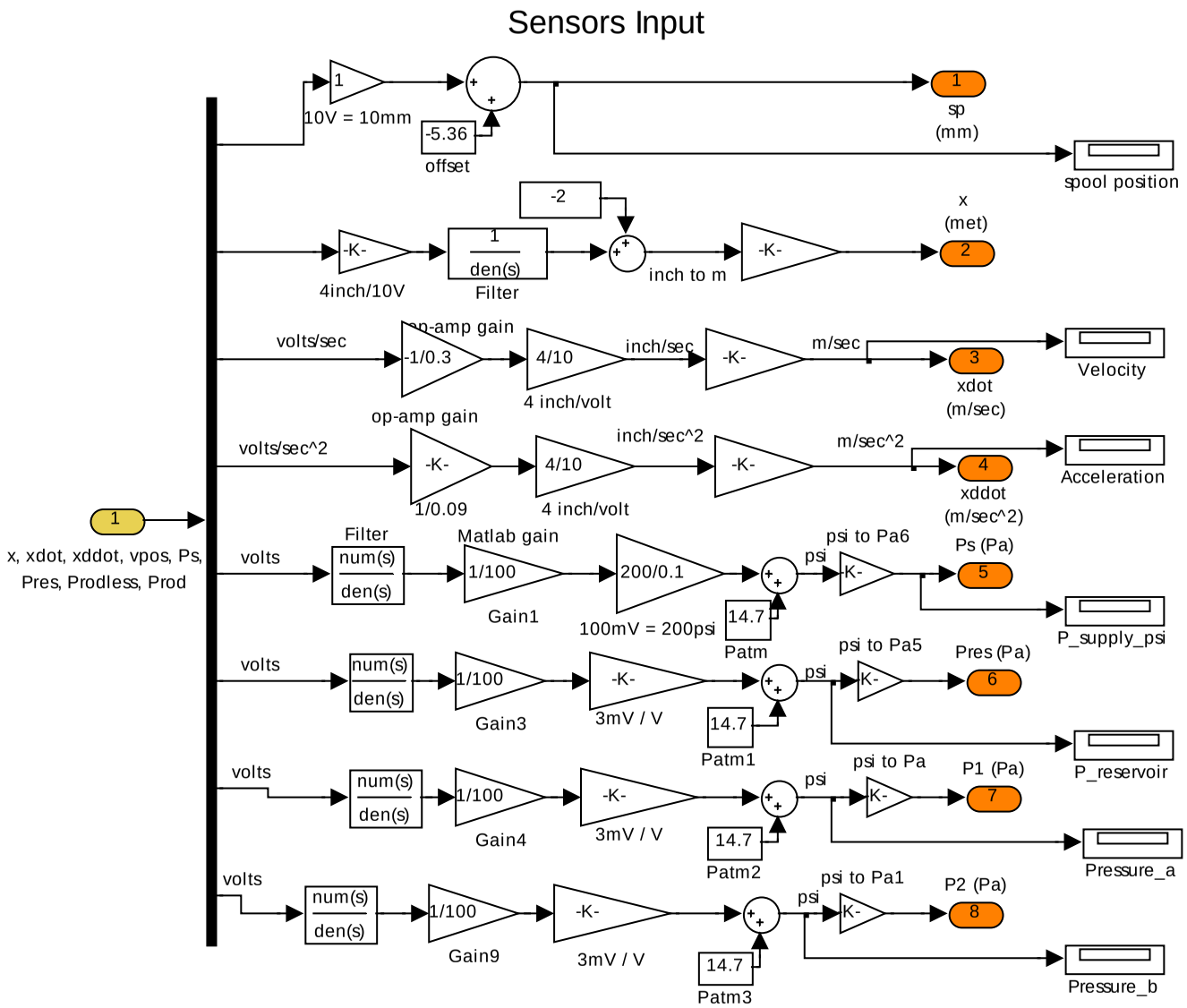

Figure C-2. Block diagram showing the calibration of sensors used in the observer-based controller of manuscript III

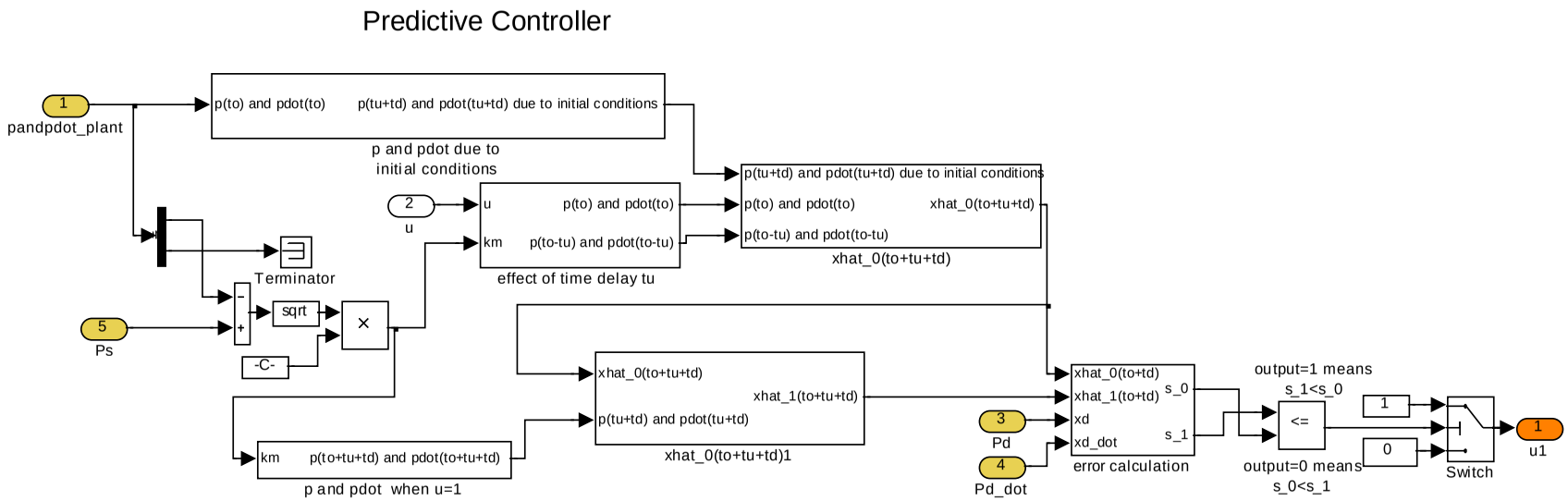

Figure C-3. Block diagram showing the implementation of the predictive control

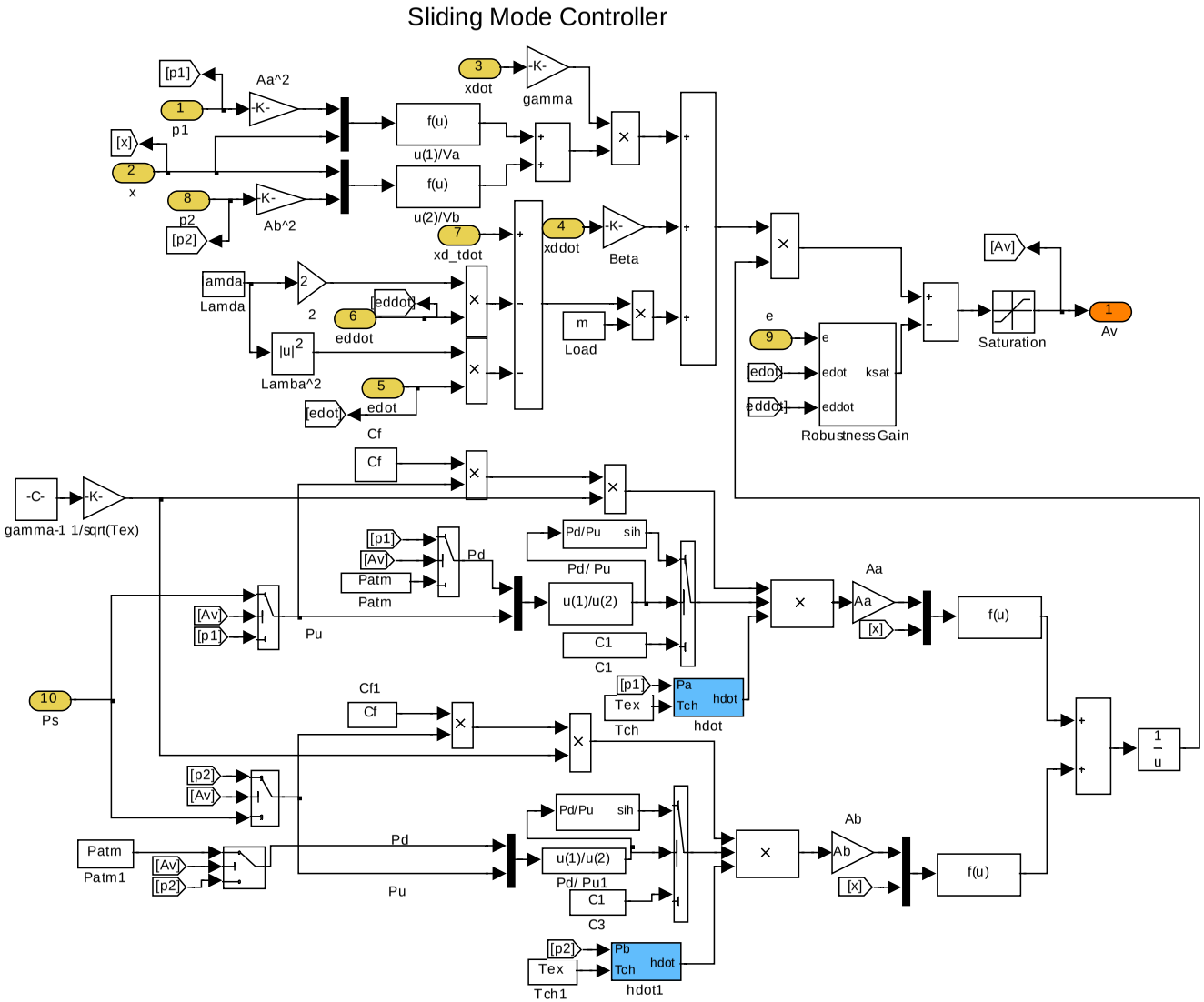

Figure C-4. Block diagram showing the implementation of the sliding mode controller for chemofluidic actuators

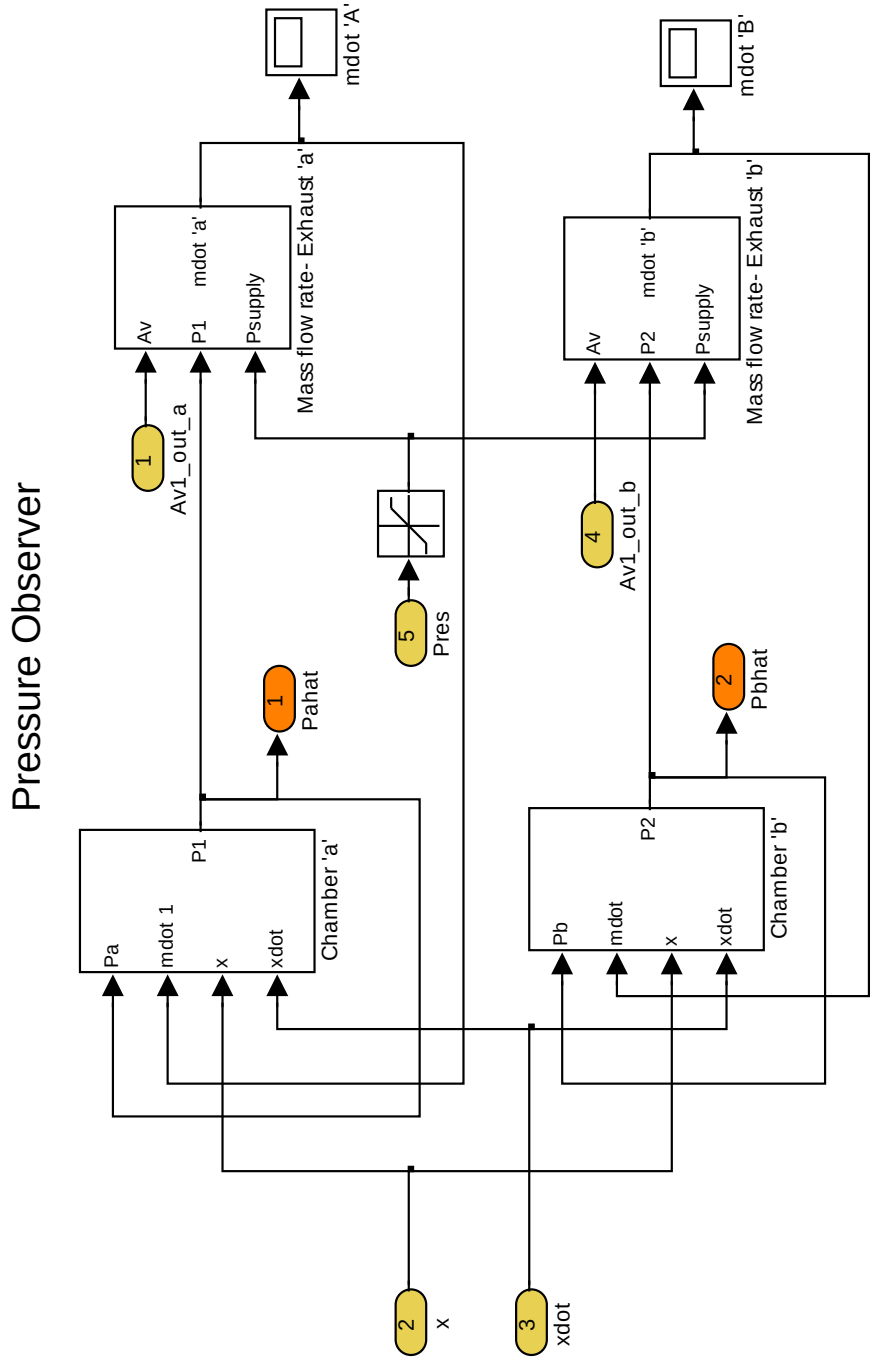

Figure C-5. Block diagram showing the implementation of the pressure observer in manuscript III

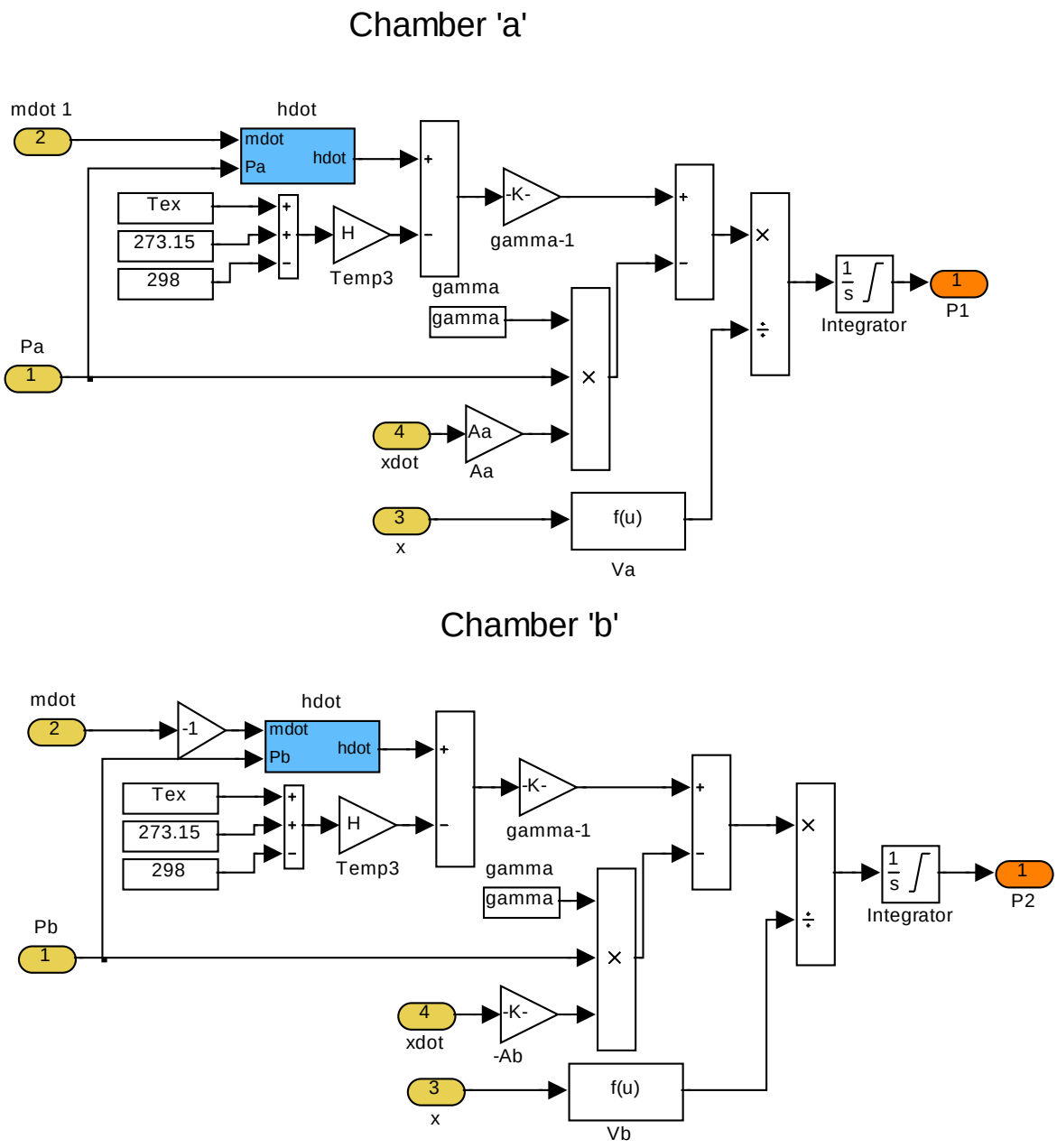

Figure C-6. Block diagram demonstrating the model of the chambers of the actuator

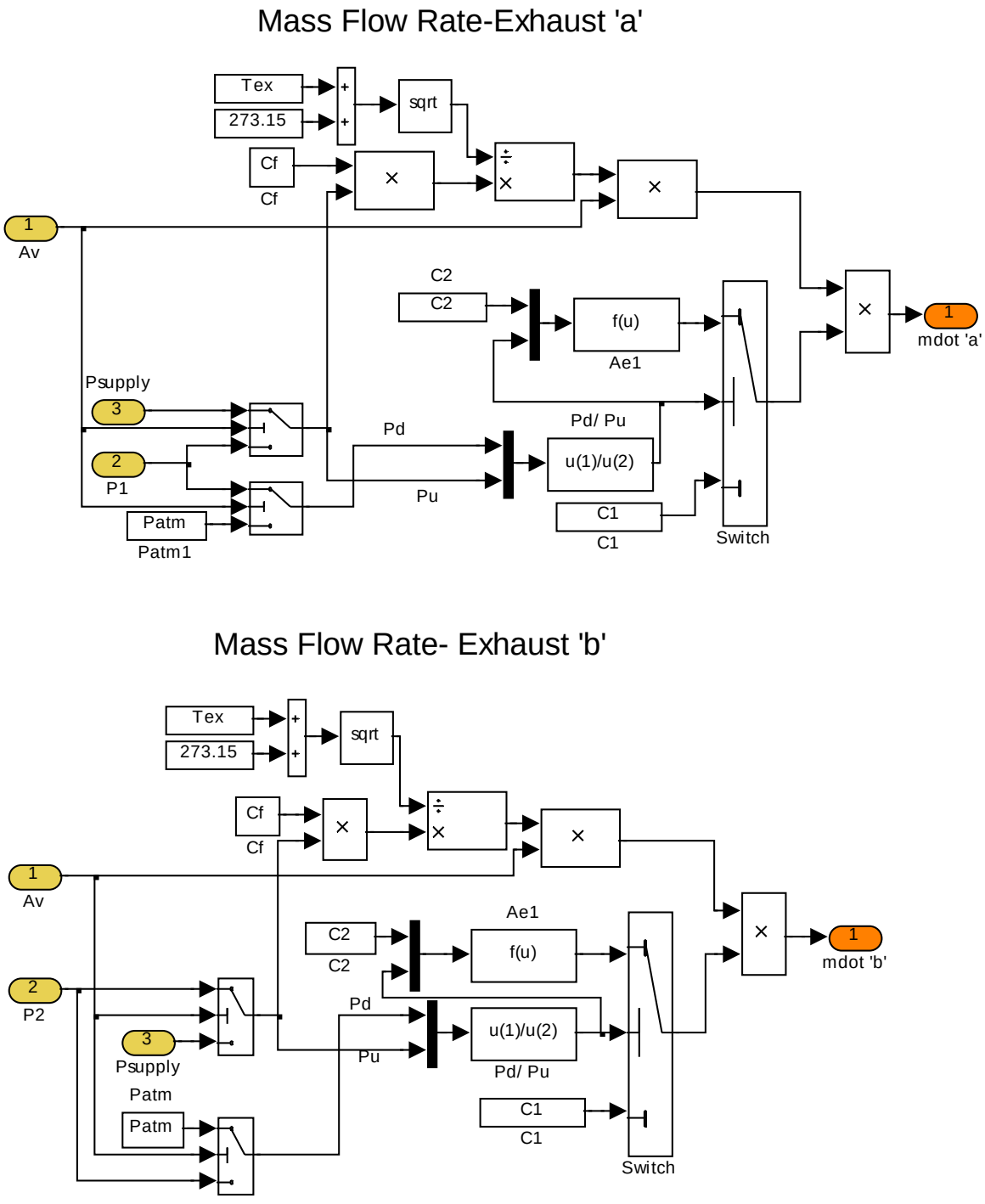

Figure C-7. Block diagram demonstrating the model of the 4-way proportional valve

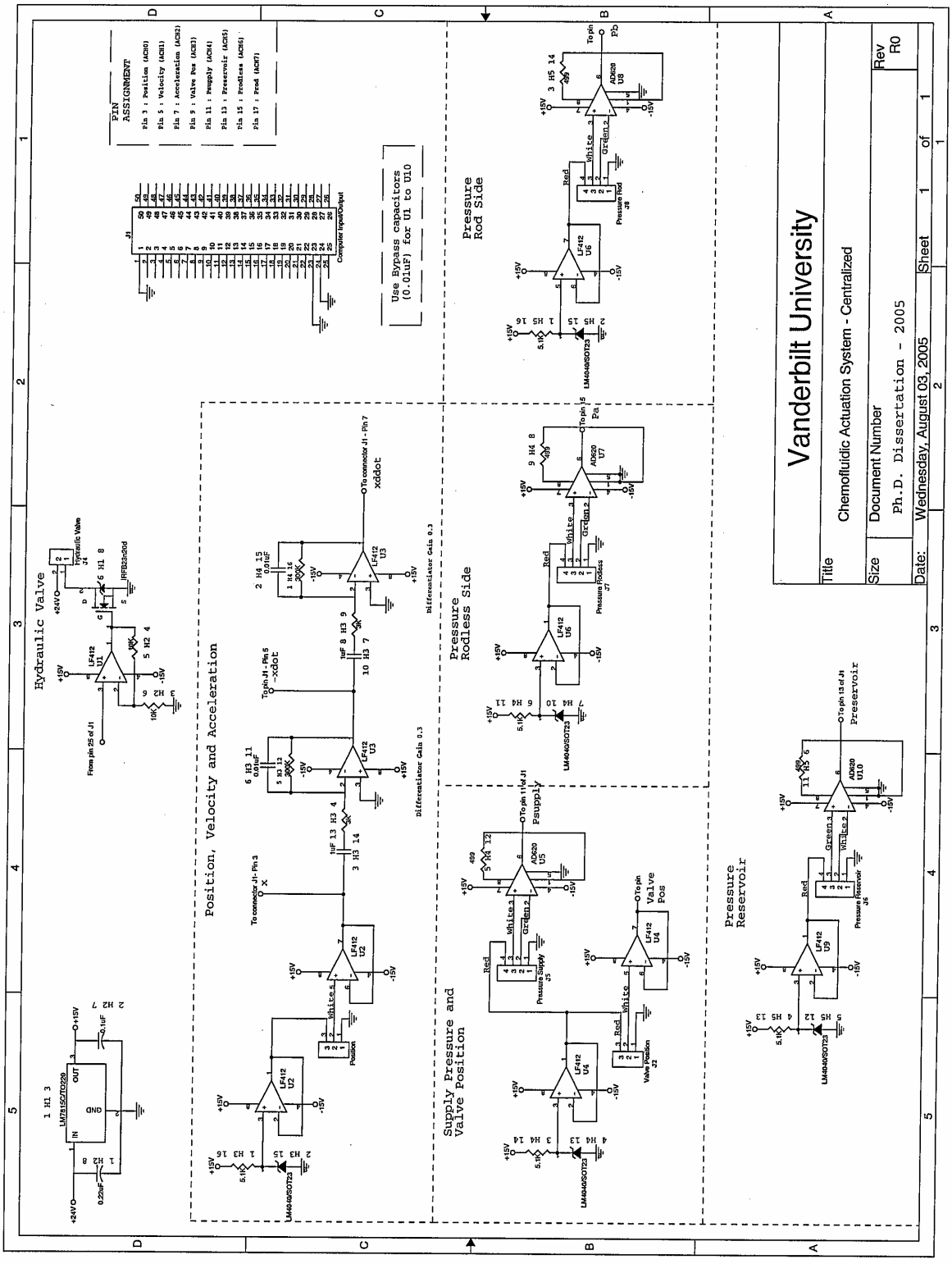

Figure C-8. Schematic of the circuit used for chemofluidic actuators

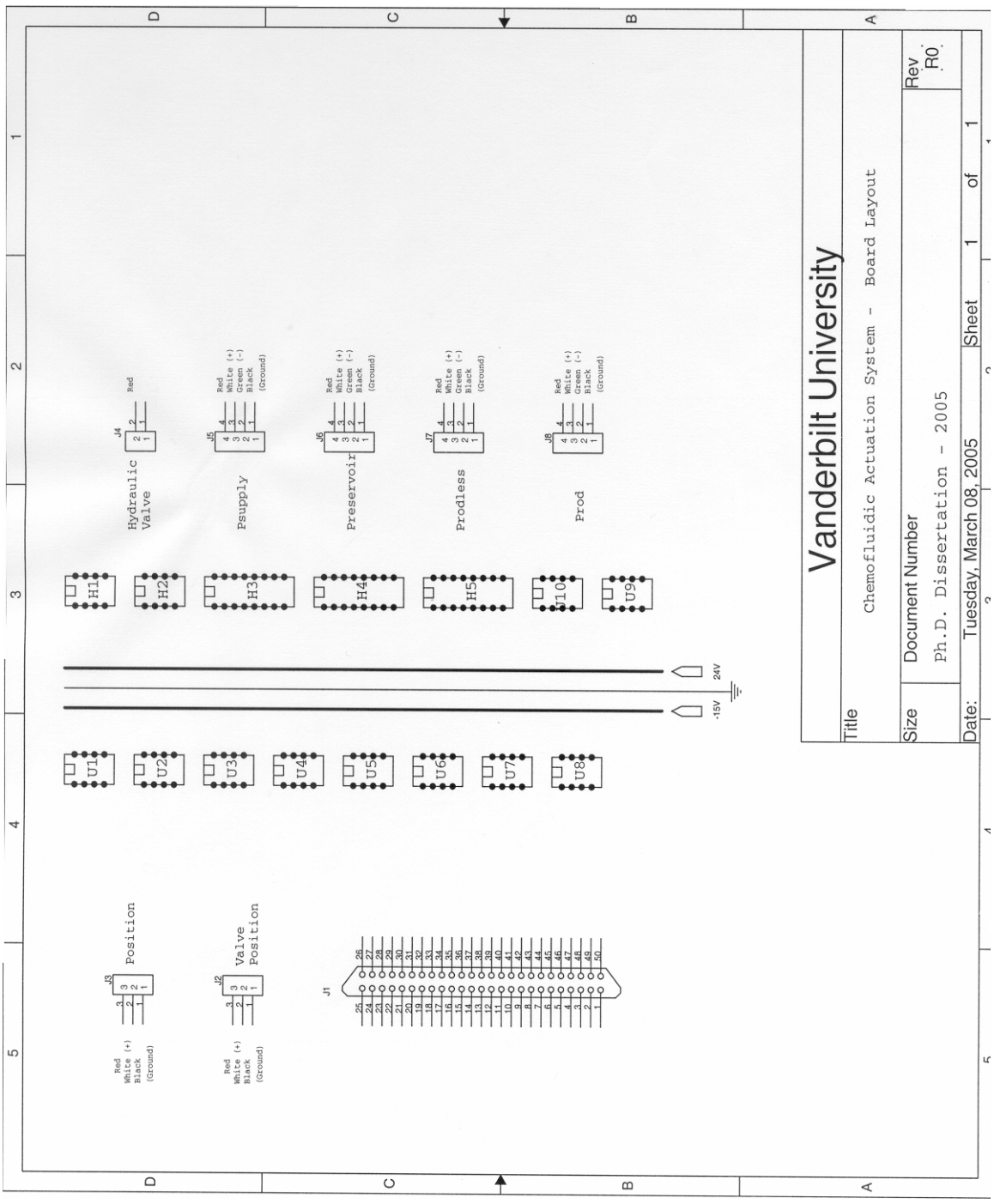

Figure C-9. Board layout of the circuit used for chemofluidic actuators